Virginia Commonwealth University
VCU Scholars Compass

Theses and Dissertations | Graduate School

2018

Integral Measurement of Atmospheric Particulate Matter (PM)

Di Liu
Virginia Commonwealth University

Follow this and additional works at: https://scholarscompass.vcu.edu/etd

 Part of the Engineering Commons

© The Author

Downloaded from
https://scholarscompass.vcu.edu/etd/5573

This Dissertation is brought to you for free and open access by the Graduate School at VCU Scholars Compass. It has been accepted for inclusion in Theses and Dissertations by an authorized administrator of VCU Scholars Compass. For more information, please contact libcompass@vcu.edu.

Integral Measurement of Atmospheric Particulate Matter (PM)

A dissertation submitted in partial fulfillment of the requirements for the degree of Doctor of Philosophy at Virginia Commonwealth University.

by

DI LIU

B.S., Environmental Science, Sun Yat-sen University, 2012

Major Director: DR. DA-REN CHEN

PROFESSOR AND FLOYD D. GOTTWALD, SR. CHAIR IN MECHANICAL AND NUCLEAR ENGINEERING

Virginia Commonwealth University
Richmond, Virginia
May 2018

© Di Liu, 2018

All Rights Reserved

Acknowledgement

I wish to express my appreciation to my advisor, Professor Da-Ren Chen, who has the attitude and the substance of a mentor: he continually and convincingly conveyed not only exploring spirit in research but also wisdom of life during my entire PhD study. His guidance and persistent help inspire me a lot, which also become treasure of my life. I also want to express my gratefulness to Dr.Chen's wife, Leelee Chen, for her understanding and motherly care in my daily life.

I would like to acknowledge members of my committee, Dr. Ta-Chih Hsiao, Dr. Weining Wang, Dr.Jianshun Zhang and Dr. Hong Zhao for taking interests in my work, examining my dissertation, and providing useful comments.

I would like to thank all members and alumni in the Particle Lab. In particular, I would like to thank Jingjie Zhang, Qiaoling Liu, Qiang Wang, Hsi-wei Yeh, Nan Zhou, Thamir Alsharifi, Peng Wang, Hao Tu, Xiaotong Chen, Zhen Li and many others, for their countless discussions and help. I also wish to thank the entire Mechanical and Nuclear Engineering Department. Many thanks go to department staff, Alison R. Bell, Lorita Peterson, Denise Ivey for their consistent assistance. I would like to thank Graduate Program Director, Dr. Karla M. Mossi, for her kindness and sincere advice.

Finally, my heartfelt gratitude goes to my parents, my parents-in-law and my husband, Zheng Zhang, for their support, patience, encouragement and sustained belief in my abilities. I am especially grateful to my husband. Without his companionship, support and encouragement, this work could not be completed.

Di Liu

April 2018

Dedicated to my parents, Jiawu Liu and Qiuhua Ai

My parents-in-law, Weizhong Zhang and Wenying Zhang

My husband, Zheng Zhang, and my lovely daughter, Duoduo

Table of Contents

List of Tables

List of Figures

Abstract

Integral Measurement of Atmospheric Particulate Matter (PM)

By Di Liu, B.S.

A dissertation submitted in partial fulfillment of the requirements for the degree of Doctor
of Philosophy at Virginia Commonwealth University.

Virginia Commonwealth University, 2018

Major Director: Dr. Da-Ren Chen
Professor and Floyd D. Gottwald, Sr. Chair in Mechanical and Nuclear Engineering

Atmospheric aerosol particles also known as atmospheric particulate matter or particulate matter (PM) are microscopic particles (solid or liquid) suspended in air, which is one of six air pollutants in US air quality standard. PM is classified as coarse particles with diameters between 2.5 to 10 μm, fine particles with a diameter less than 2.5 μm ($PM_{2.5}$), and ultrafine particles with the diameter less than 0.1 μm ($PM_{0.1}$). Epidemiological studies have already showed the adverse health effects (such as asthma, lung cancer and respiratory and cardiovascular disease) resulted from exposure to the fine and ultrafine particles. Monitoring the PM concentration (i.e., either mass or surface area concentration of PM) is critical for the protection of public health and environment and for the regulatory

control. Various PM sensors are now available in market. A majority of these PM sensors are optical sensors, whose readouts are highly depended on the physical property and composition of PM. Several PM monitors based on the measurement principle of electrical charging are also available. However, the empirical calibration of the readout of these electrical PM monitors via the use of standard dust particles makes it difficult to obtain the true mass concentration of PM when PM size distribution is different from that of standard dust.

The overall objective of this dissertation is to advance our scientific knowledge on the performance of cost-effective PM monitors for measuring either mass or surface area concentration of fine and ultrafine PM. This thesis includes two parts: (1) is on the evaluation of existing PM sensor for PM mass concentration measurement; (2) is on the development of new PM monitor for PM surface area concentration measurement. For the first part of this dissertation, four low-cost optical sensors, one Personal Dust Monitor (PDM) and Dustrak^{TM} were experimentally evaluated. Particles in the size distribution having different mean size, standard deviation value and material were used as test aerosol particles. The readouts of these low-cost and portable sensors are compared to that of a standard TEOM (Tapered Element Oscillation Microbalance). For the second part of this dissertation, a new electrical PM monitor, consisting of a corona-based aerosol charger, a precipitator and high sensitive current meter, has been proposed for measuring surface area concentration of fine and ultrafine PM. Particles are electrically charged upon entering an electrical PM monitor. Instead of using Faraday cage and current meter to measure the charges carried by particles in existed electrical PM sensors, the new PM monitor measures the current carried by particles deposited directly on the wall of the precipitator. A thorough

evaluation has been carried out to evaluate the fundamental performance of this new PM monitor. In addition, small cyclones (i.e., quadru-inlet and tapered-body cyclones) were also evaluated as the size-selective inlet of these PM sensors/monitors to minimize the potential interface from the presence of PM with large sizes in the air. The small quadru-inlet cyclone is to resolve the issue of directional sampling; and the tapered-body cyclones is to reduce the cyclone pressure drop while having small cyclone cutoff particle size. Each cyclone has been evaluated via the measurement of particle penetration curve and pressure drop. Semi-empirical models have been obtained for the prediction of cyclone performance.

CHAPTER 1 Introduction and Overview

1.1 Introduction to PM measurement

"Particulate Matter", usually abbreviated to "PM", is a mixture of solid particles and liquid droplets in the air. It is one of the six air pollutants considered harmful to public health and environment. The PM can vary as much as the variety of the size, surface area, concentration, chemical composition, physical properties and sources. Some particles are large and people can easily see them, while some are too small to be seen with naked eye. People usually categorizes the particles into different groups according to their aerodynamic diameter size. Particles with diameter smaller than 10 μm are defined as PM_{10}, also named as "inhalable particles". $PM_{2.5}$ is particles with diameters equal to and smaller than 2.5 μm, and generally described as "fine particles". Particles with diameter smaller than 0.1 μm are termed as the "ultrafine particles". What need to mention here, the PM_{10} contains the $PM_{2.5}$ and $PM_{0.1}$. Similarly, $PM_{2.5}$ also contains the ultrafine particles. (USEPA, http://www.epa.gov/pm/)

The sources of PM are often categorized as nature or human-made (Pérez et al., 2010; Pui, Chen, & Zuo, 2014; Sun et al., 2004). The nature sources of PM include forest fire, dust storm, volcano, sea salt and so on. These natural sources are uncontrollable. Human-made sources of PM are more important than natural sources. Industry source is one major human-made source. PM can be produced during both industrial processes, such as bulk material handling, combustion and minerals processing, and industrial emission. Transportation source, which can generate particles from the fuels burning or from wear of tires, is another important human-made PM source. Besides, the daily activities, such as

construction, unpaved roads, domestic heating and cooking, can also generate PM. Beside the direct-released PM sources, a substantial fraction of PM in the atmosphere is from the photo- and other chemical reaction of gaseous precursors, such as sulfur dioxide and nitrogen oxides.

The fine particles ($PM_{2.5}$), even the ultrafine particles ($PM_{0.1}$) are drawing more and more attention recently. The reason for this is that many health and environmental problems are related to particle pollution according to researches. The fine particles ($PM_{2.5}$) are the main cause of reduced visibility (Huang et al., 2009; Nam-Jun et al., 1996). Besides, because of the different chemical composition, PM might also cause environmental damages when they settle on ground or water, such damages include but not limit to acidize lakes and streams, change the nutrient balance in waters, deplete the nutrients in soil and cause acid rain. Early PM researchers reported that the number concentration of PM is lower at the exhale than inhale by a person, which mean a portion of PM was "trapped" in human body (Burke et al., 1955). According to the research studied the particle deposition in respiratory system, smaller particles are more likely to have retention in deeper position, like bronchial and alveolar region, while larger particle are usually trapped in extra-thoracic region (Hatch, 1961). Although the mechanisms of how PM interacts with human body and give rises to adverse health effects are not clearly understood, many studies have evidenced that fine particles and ultrafine particles are associated with the daily mortality. (Cao et al., 2012; Chen et al., 2011; Dockery et al., 1993; Evans et al., 2013; Franklin et al, 2008; Geng et al., 2013; Krewski 2009; Pope et al., 2002; Samoli et al., 2013; Yang et al., 2012). Respiratory and cardiovascular diseases are major problems resulted from the PM pollution. There is also evidence that longer-period

exposure to $PM_{2.5}$ will trigger respiratory problems, while the cardiovascular problems are occurring more promptly, within few hours or days. Many researches have indicated that exposure of fine particles will trigger asthma (Fan et al., 2015; Norris et al., 1999). Epidemiologic studies showed increased level of fine and ultrafine particles can be responsible for increased rates of lung cancer (Borm et al., 2004; Cohen and Pope, 1995; Knaapen et al., 2004; Nyberg et al., 2000; Tie et al. 2009). Besides, many studies also showed that people in certain group (i.e., children, elder and pregnant women) have increased risk for cardiovascular and respiratory mortality if they were exposed to $PM_{2.5}$ (Franklin et al., 2007; Ma et al., 2011; Ostro et al., 2006; Schwartz et al., 1996).

Due to the adverse effects mentioned above, accurate measurement of PM concentration is critical for environmental, human protection and regulatory control. Three metrics are usually used to quantify the PM pollution, i.e., mass concentration, surface area concentration and number concentration. Typically, mass concentration is the most popular metrics in particle measurement, which is useful to interpret certain mass-driven phenomena, eg. sedimentation and dose effect. However, when the particles get down to very small size, the mass concentration may not be the best metric to use, as the weight collected from many thousands of small particles might be equivalent to only one $PM_{2.5}$ particle. Therefore, the surface area concentration or the number concentration might be more favorable metrics in this case. The surface area concentration of particles is a key character in several environmental processes, such as sorption or dissolution ability of nanomaterial, toxicity of airborne particles, drug delivery and catalysts application (Handy et al., 2008; Baun et al., 2008; Redhead et al., 2001). Surface area per unit volume of particles increases as particle size decrease, thus smaller particles possess larger relative

surface area than larger particles. Therefore, smaller particles might be more harmful to human health because of more active surface area. Oberdorster pointed out the adverse health effects are highly related to the particle total geometric surface area (Oberdorster, 2000). It is desirable to use surface area concentration metric rather than the mass concentration metric to quantify the harm from PM pollution in submicron particle size range ($PM_{1.0}$). Besides the mass and surface area concentration, the number concentration is also another important PM concentration metrics. It is useful to present the aggregation and disaggregation behavior of particles (Chen and Elimelech, 2006; Baalousha et al., 2013). In terms of number-based view, ultrafine particles (UFPs) are dominant. Many researches had already evidenced the UFPs have strong impact on human health, which also emphasized the importance of number concentration.

All these three metrics (i.e., mass concentration metric, surface area concentration metric and number concentration metric) are useful in the PM pollution assessment. The National Ambient Air Quality Standard (NAAQS) was carried out by US Environmental Protection Agency(USEPA) in 1971, and had been revised several times since then, to control the aerosol problems more effectively. Table 1-1 list the National Ambient Air Quality Standards for Particulate Matter during 1971 to 2012. According to Table.1, it can be found that the NAAQS is based on PM mass concentration, and the PM indicator are changing from Total suspension particles (TSP) to PM_{10}, and to $PM_{2.5}$, which showed that smaller particles are attracting more attention recently. Even though $PM_{2.5}$ is the smallest particle size in the newest standard, some considerations have been raised that submicron particles ($PM_{1.0}$) or even the ultrafine particles ($PM_{0.1}$) should be an ambient standard (Lee et al., 2006; Jian et al., 2011).

Table 1- 1 History of the National Ambient Air Quality Standards for Particulate Matter During the Period 1971-2012

Issue Time	Type	Indicator	Averaging Time	Level
1971	Primary	TSP	24-hour	260 μg/m^3
			Annual	75 μg/m^3
	Secondary	TSP	24-hour	150 μg/m^3
			Annual	60 μg/m^3
1987	Primary and Secondary	PM_{10}	24-hour	150 μg/m^3
			Annual	50 μg/m^3
1997	Primary and Secondary	PM_{10}	24-hour	150 μg/m^3
			Annual	50 μg/m^3
		$PM_{2.5}$	24-hour	65 μg/m^3
			Annual	15 μg/m^3
2006	Primary and Secondary	PM_{10}	24-hour	150 μg/m^3
		$PM_{2.5}$	24-hour	65 μg/m^3
			Annual	15 μg/m^3
2012	Primary	$PM_{2.5}$	Annual	12 μg/m^3
	Secondary		Annual	15 μg/m^3
	Primary and Secondary		24-hour	35 μg/m^3
		PM_{10}	24-hour	150 μg/m^3

In order to meet the NAAQS, instruments and techniques for the PM monitoring have been developed for decades (Amaral et al., 2015). As the NAAQS is based on PM mass concentration, several methods for PM mass concentration measurement were well-developed and existed in the market. Gravimetric sampler is the most reliable method because it conducts a direct measurement on particle mass concentration. However, because gravimetric sampler is time-consuming and labor-needed, many other methods on particle mass measurement were developed (Ayers et al., 1999). Moreover, because of the tempo-spatial distribution of $PM_{2.5}$ in the ambient, the demand for cost-effective aerosol sensors in small packages and without sacrificing accuracy is increasing (Zhu et al., 2002). Tapered element oscillating microbalance and photometers are two popular techniques

used in many portable PM mass measurement devices. However, these two methods have their own pros and cons, which will be discussed in chapter 2.

Moreover, the performance of the portable particle sensors is often interfered by the presence of the large particles. Small particle size-selective inlets are thus needed to remove large particles from the sampling stream of these devices. Because of their high particle loading capacity and relatively low pressure drop, cyclones are often chosen as the particle separation device, which can be used before these portable particle sensors. Hsiao developed two miniature cyclones, which operated in low sampling flowrate (i.e., 0.3 lpm) and maintained good collection performance (i.e., 0.3 and 1.0 μm, respectively). However, the pressure drop of Hsiao's mini-cyclones are too high, which cannot be handle by the pump of many portable monitors.

1.2 Motivation and Objective

Electrical aerosol detector (EAD) is a simple technique capable of monitoring the integral parameters, such as total number, length and surface area concentration. A charger, of which the performance strongly influences the readout, is the key component in an EAD. An electrometer is used for measuring the current induced by the charged particles in an EAD. According to the particle charging patent, a well-designed EAD can thus meet the requirement to monitor the above-mentioned integral parameters by manipulating the operation condition (i.e., charger current, operation flowrate, etc.). Up till now, the EAD technique is mostly used in monitoring the total surface area concentrations of particles deposited in a human lung, while some researchers also developed the EAD-type monitor for mass measurement. However, all the existing EAD-type monitors are based on simple signal-to-concentration correlation. Because of the advantages on material dependent, fast

response, very good sensitivity and simple configuration, the existing EAD technique is expected to be advanced for more reliable PM measurement.

The main objective of this research is to develop a new PM monitor based on EAD technique, which signals are truly proportional to the integral parameters (i.e., total mass, surface area or number concentration) of the sampling particle. For the sake of reducing the large particle interference, the accompanied objective is to develop small cyclones as size-selective inlet, which can be handled by the miniature pump of the portable monitor.

1.3 Dissertation structure

The whole dissertation contains six chapters, which can be classified into two parts. The first part, including chapter 2 and 3, focuses on existing PM monitors review and evaluation. The second part, including chapter 4 and 5, focuses on the new PM monitor and its size-selective inlet development. Brief descriptions of each chapter are as following.

In chapter 1, a general introduction of the background, motivation and research objectives are presented.

In chapter 2, integral measurement methods of the PM mass concentration are reviewed and summarized. Besides, the working principle of EAD technique are elaborated, and the existing PM monitors based the EAD technique are also reviewed. The deficiencies of these existing PM monitors are also presented, which lead to opportunity for the new PM sensors.

In chapter 3, the performance of six low-cost and portable PM monitors are evaluated. These PM monitors are challenged by groups of polydisperse particles with different mean

particle size, geometrical standard deviation and material. These PM monitors are also tested under different working condition (i.e., steady and transient particle concentration). Difference among these experimental results are observed and discussed.

In chapter 4, the development of a new EAD-type PM sensor (eM sensor) is described. The design of the two main components (i.e., charger and precipitator) are presented. The operation condition (i.e., flowrate, charger current, etc.) of the eM sensor, as either total surface area monitor or mass monitor, are set according to the components evaluation results. By assembled the charger, precipitator and current monitor (i.e., electrometer) together, the overall performance evaluation of the eM sensor, as a total surface area monitor and mass monitor, are both carried out. The final experimental data are explained and discussed with simple theoretical calculation.

In chapter 5, two types of small cyclones are developed as size-selective inlet for the eM sensor: One is the quadru-inlet mini-cyclone, the other are the tapered body cyclones. The pressure drop and particle penetration efficiencies performance of these cyclones are presented. The performances of these cyclones are also compared to the existing small cyclones. Semi-empirical models are also proposed to predict both pressure drop and particle cutoff size of these cyclones, respectively.

In chapter 6, the accomplishments of this dissertation are summarized, and the issues and challenge that deserve future research efforts are also broached.

1.4 Reference

Amaral, S., de Carvalho, J., Costa, M., & Pinheiro, C. (2015). An Overview of Particulate Matter Measurement Instruments. Atmosphere, 6(9), 1327-1345.

Ayers, G. P., Keywood, M. D., & Gras, J. L. (1999). TEOM vs. manual gravimetric methods for determination of PM2.5 aerosol mass concentrations. Atmospheric Environment, 33(22), 3717-3721.

Baalousha, M., et al. (2013). "Effect of monovalent and divalent cations, anions and fulvic acid on aggregation of citrate-coated silver nanoparticles." Science of the Total Environment 454: 119-131.

Baun, A., et al. (2008). "Ecotoxicity of engineered nanoparticles to aquatic invertebrates: a brief review and recommendations for future toxicity testing." Ecotoxicology **17**(5): 387-395.

Borm, P. J., Schins, R. P., & Albrecht, C. (2004). Inhaled particles and lung cancer, part B: paradigms and risk assessment. International Journal of Cancer, 110(1), 3-14.

Burke, T., et al. (1955). "Nucleus content of air in occupied rooms." Geofisica pura e applicata 31(1): 191-196.

Cao, J.-J., Shen, Z.-X., Chow, J. C., Watson, J. G., Lee, S.-C., Tie, X.-X., Han, Y.-M. (2012). Winter and summer PM2. 5 chemical compositions in fourteen Chinese cities. Journal of the Air & Waste Management Association, 62(10), 1214-1226.

Chen, K. L. and M. Elimelech (2006). "Aggregation and deposition kinetics of fullerene (C60) nanoparticles." Langmuir **22**(26): 10994-11001.

Chen, B., Kan, H., Chen, R., Jiang, S., & Hong, C. (2011). Air pollution and health studies in China—policy implications. Journal of the Air & Waste Management Association, 61(11), 1292-1299.

Cohen, A. J., & Pope, C. A. (1995). Lung cancer and air pollution. Environmental Health Perspectives, 103(Suppl 8), 219-224.

Dockery, D. W., Pope, C. A., Xu, X., Spengler, J. D., Ware, J. H., Fay , M. E., Speizer , F. E. (1993). An Association between Air Pollution and Mortality in Six U.S. Cities. New England Journal of Medicine, 329(24), 1753-1759. doi: 10.1056/NEJM199312093292401

Evans, J., van Donkelaar, A., Martin, R. V., Burnett, R., Rainham, D. G., Birkett, N. J., & Krewski, D. (2013). Estimates of global mortality attributable to particulate air pollution using satellite imagery. Environmental Research, 120, 33-42.

Fan, J., Li, S., Fan, C., Bai, Z., & Yang, K. (2015). The impact of PM2.5 on asthma emergency department visits: a systematic review and meta-analysis. Environmental Science and Pollution Research, 23(1), 843-850.

Franklin, M., Koutrakis, P., & Schwartz, J. (2008). The role of particle composition on the association between PM2. 5 and mortality. Epidemiology (Cambridge, Mass.), 19(5), 680.

Franklin, M., Zeka, A., & Schwartz, J. (2007). Association between PM2.5 and all-cause and specific-cause mortality in 27 US communities. Journal of Exposure Science and Environmental Epidemiology, 17(3), 279-287.

Geng, F., Hua, J., Mu, Z., Peng, L., Xu, X., Chen, R., & Kan, H. (2013). Differentiating the associations of black carbon and fine particle with daily mortality in a Chinese city. Environmental Research, 120, 27-32.

Handy, R. D., et al. (2008). "The ecotoxicology and chemistry of manufactured nanoparticles." Ecotoxicology **17**(4): 287-314.

Hatch, T. F. (1961). "Distribution and deposition of inhaled particles in respiratory tract." Bacteriological reviews 25(3): 237.

Hsiao, T.-C., Chen, D.-R., & Son, S. Y. (2009). Development of mini-cyclones as the size-selective inlet of miniature particle detectors. Journal of Aerosol Science, 40(6), 481-491.

Huang, W., Tan, J., Kan, H., Zhao, N., Song, W., Song, G., Chen, R. (2009). Visibility, air quality and daily mortality in Shanghai, China. Science of the Total Environment, 407(10), 3295-3300.

Jian, L., Zhu, Y. P., & Zhao, Y. (2011). Monitoring fine and ultrafine particles in the atmosphere of a Southeast Chinese city. Journal of Environmental Monitoring, 13(9), 2623-2629.

Krewski, D. (2009). Evaluating the Effects of Ambient Air Pollution on Life Expectancy. New England Journal of Medicine, 360(4), 413-415.

Knaapen, A. M., Borm, P. J., Albrecht, C., & Schins, R. P. (2004). Inhaled particles and lung cancer. Part A: Mechanisms. International Journal of Cancer, 109(6), 799-809.

Lee, S. C., Cheng, Y., Ho, K. F., Cao, J. J., Louie, P. K., Chow, J. C., & Watson, J. G. (2006). PM1.0 and PM2.5 characteristics in the roadside environment of Hong Kong. Aerosol Science and Technology, 40(3), 157-165.

Ma, Y., Chen, R., Pan, G., Xu, X., Song, W., Chen, B., & Kan, H. (2011). Fine particulate air pollution and daily mortality in Shenyang, China. Science of the Total Environment, 409(13), 2473-2477.

Nam-Jun, B., Yong Pyo, K., & Kil Choo, M. (1996). Visibility study in Seoul, 1993. Atmospheric Environment, 30(13), 2319-2328.

Norris, G., et al. (1999). "An association between fine particles and asthma emergency department visits for children in Seattle." Environmental Health Perspectives 107(6): 489-493.

Nyberg, F., Gustavsson, P., Järup, L., Bellander, T., Berglind, N., Jakobsson, R., & Pershagen, G. (2000). Urban air pollution and lung cancer in Stockholm. Epidemiology, 11(5), 487-495.

Oberdörster, G. (2000). Pulmonary effects of inhaled ultrafine particles. International archives of occupational and environmental health, 74(1), 1-8.

Ostro, B., Broadwin, R., Green, S., Feng, W.-Y., & Lipsett, M. (2006). Fine particulate air pollution and mortality in nine California counties: results from CALFINE. Environmental Health Perspectives, 29-33.

Pérez, N., Pey, J., Cusack, M., Reche, C., Querol, X., Alastuey, A., & Viana, M. (2010). Variability of Particle Number, Black Carbon, and PM10, PM2.5, and PM1 Levels and Speciation: Influence of Road Traffic Emissions on Urban Air Quality. Aerosol Science and Technology, 44(7), 487-499. doi:10.1080/02786821003758286

Pope, I. C., Burnett, R. T., Thun, M. J., & et al. (2002). Lung cancer, cardiopulmonary mortality, and long-term exposure to fine particulate air pollution. JAMA, 287(9), 1132-1141.

Pui, D. Y. H., Chen, S.-C., & Zuo, Z. (2014). PM2.5 in China: Measurements, sources, visibility and health effects, and mitigation. Particuology, 13, 1-26.

Redhead, H., et al. (2001). "Drug delivery in poly (lactide-co-glycolide) nanoparticles surface modified with poloxamer 407 and poloxamine 908: in vitro characterisation and in vivo evaluation." Journal of Controlled Release 70(3): 353-363.

Samoli, E., Stafoggia, M., Rodopoulou, S., Ostro, B., Declercq, C., Alessandrini, E., Le Tertre, A. (2013). Associations between fine and coarse particles and mortality in Mediterranean cities: results from the MED-PARTICLES project. Environmental Health Perspectives (Online), 121(8), 932.

Schwartz, J., Dockery, D. W., & Neas, L. M. (1996). Is daily mortality associated specifically with fine particles? Journal of the Air & Waste Management Association, 46(10), 927-939.

Sun, Y., Zhuang, G., Wang, Y., Han, L., Guo, J., Dan, M., Hao, Z. (2004). The air-borne particulate pollution in Beijing—concentration, composition, distribution and sources. Atmospheric Environment, 38(35), 5991-6004.

Tie, X., Wu, D., & Brasseur, G. (2009). Lung cancer mortality and exposure to atmospheric aerosol particles in Guangzhou, China. Atmospheric Environment, 43(14), 2375-2377.

Yang, C., Peng, X., Huang, W., Chen, R., Xu, Z., Chen, B., & Kan, H. (2012). A time-stratified case-crossover study of fine particulate matter air pollution and mortality in Guangzhou, China. International archives of occupational and environmental health, 85(5), 579-585.

Zhu, Y., et al. (2002). "Study of ultrafine particles near a major highway with heavy-duty diesel traffic." Atmospheric Environment 36(27): 4323-4335.

CHAPTER 2 Review of PM integral measurement technique

Various particle instruments were developed to measure the different properties of particles, including particle number concentration, surface area concentration, mass concentration, chemical composition, etc. These particle instruments are usually characterized as two categories: sampling instruments and direct-reading instruments. For the particle sampling instruments, the particles are collected on some substrates, which are subsequently assessed for microscopic, gravimetric or chemical analysis. These instruments can be used for long-term measurement in which time-average concentration is required. However, for presenting the rapid changes on particles, the sampling instruments might encounter an issue. By using direct-reading instruments, the properties of aerosols can be obtained instantaneously. Along with the development of modern electronics, both particle size distribution and concentration can be obtained by these direct-reading instruments in a short period of time. Among these direct-reading instrument, many of them are used to measure the integral moment of a total particle size distribution, such as total number, surface area and mass concentration (Pui, 1996). In this chapter, several widely used direct-reading instruments for particle mass concentration and surface area measurement are reviewed.

2.1 PM mass concentration measurement

The direct-reading instruments used in particle mass concentration measurement are classified into three groups, according to their method of detection: mechanical, optical and electrical. PM mass monitors based on mechanical and optical detection methods have

existed for several decades, while the device based on the electrical method emerged recently.

2.1.1 Mechanical means

Tapered Element Oscillating Microbalance (TEOM) is one of the standard method in sampling the aerosol mass concentration continuously (Patashnick & Rupprecht, 1991). The schematic diagram of the main component in a TEOM is shown in Fig 2-1. The main component is a hollow tapered element that is maintained by an electronic feedback system. A filter is located at the end of this tapered element. As the pump turns on, the particles are sampled from the inlet and collected on the filter. The increased mass on the filter also changes the resonant frequency of the element. A light-emitting diode and a phototransistor are aligned perpendicularly to the oscillation plane of the tapered element, measuring the frequency of the element. The changed frequency can therefore be transferred into the electrical signals. The amount of particle mass sampled can be evaluated in a short time which is related to these electric outputs.

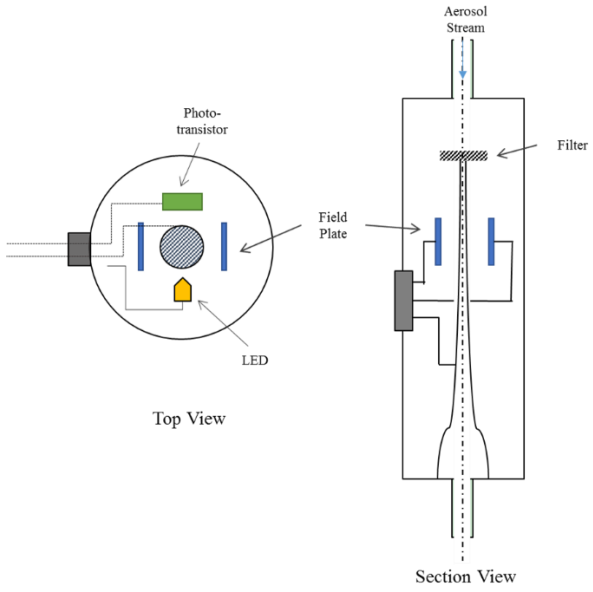

Figure 2 - 1 Schematic diagram of a Tapered Element Oscillating Microbalance (TEOM).

Personal dust monitor (PDM3700, Thermal Fisher Scientific Inc) is a portable PM monitor using the TEOM technique (Volkwein et al, 2004; Volkwein et al, 2006). It was developed by the United States National Institute for Occupational Safety and Health and the United States Mine Safety and Health Administration. It can be used to monitor the concentration of the respirable coal mine dust within the breathing zone of the miners continuously. The oscillating element in the PDM is a deformed metal tube. The change of loaded filter mass leads to the shifting of the vibrating frequency of the tapered element.

The key feature of the TEOM technique is that it measures the mass of sampled dust on a filter directly, regardless of dust composition, size or physical characteristics. This technique provides a more convenient way, which continuously monitors the PM concentration in the ambient environment. However, the TEOM technique still has its own disadvantages. The filter needs to be changed when it reaches a high percentage loading.

And, it is power consuming because of the pump operation. Also, it encounters problems in measuring the particles with volatile components.

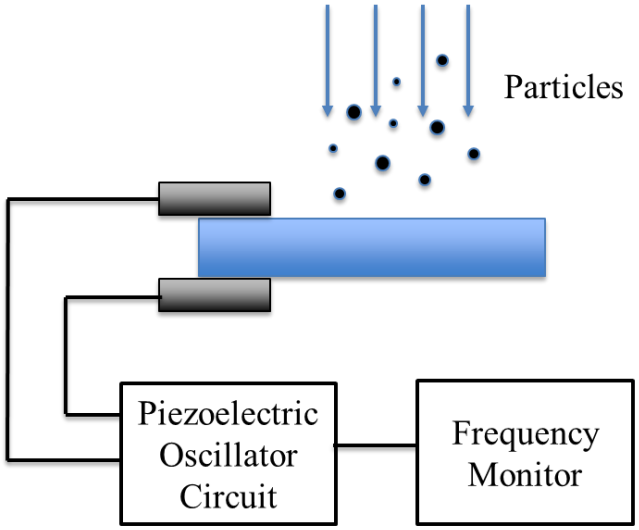

Figure 2 - 2 Schematic diagram of a Quartz Crystal Microbalance (QCM).

Another mechanical-type PM mass concentration monitor is the quartz crystal microbalance (Figure 2-2). The operation principle of QCM is similar to that of TEOM (Ward, and Buttry, 1990; Sem et al., 1977). A quartz crystal (i.e., piezoelectric material), sandwiched between two opposite metallic electrodes, is used in a QCM sensor. As particles deposited on the quartz crystal by either inertial impaction or by electrostatic precipitation, a shift in its natural vibrating frequency can be induced (which is proportional to the sampled mass). However, the frequency shift can be highly affected by the particle deposited location (Daley and Lundgren, 1975).

2.1.2 Optical means

For atmospheric studies, the total light-scattering coefficient of airborne particles is related to the atmospheric visibility (Waggoner and Charlson, 1976). Therefore,

photometers or integrating nephelometer are developed as PM monitors based on the particle optical properties and light scattering principle (Görner et al, 1995).

Due to the low cost of the elementary components (i.e., laser diode and photodiode) and simple configuration, many commercial mass monitors in the market are photometers. Table 2-1 lists some commercial photometer-type PM sensors. A photometer provides an indirect measure of particulate mass concentration based on the optical properties of the particles. It measures the intensity of the overall scattering light from the group of particles in the viewing volume. A light source and a detector are essential components in a photometer. Fig 2-3 shows the basic schematic diagram of a photometer. As the particles are drawn into the chamber, they are illuminated by the light source. A photodetector arranged at a certain angle to the light source detects the scattered light flux from the viewing volume. The photodetector converts the light signal to electrical signal, and the strength of the electrical signals are dependent on the mass of the particles passing through the volume.

Table 2 - 1 Some commercial portable photometers for PM mass concentration measurement

Model	Detection Range	Optics	Price
TSI DustTrak DRX Aerosol Monitor 8533 and 8534	1 to 100,000 µg/m³	Light source: 655nm detection angle: 90 ± 62°	$4995
Thermal Fisher Scientific personal DataRAM™ pDR-1200	1 to 400,000 µg/m³	Light source: 880nm detection angle: 50° to 90°	$5829
TSI Sidepak AM510	1-20,000 µg/m³	Light source: 650nm 90° light scattering	$3975
Met One AEROCET 531 Handheld Particle Mass Profiler and Counter	1-1,000 µg/m³	Light source: 780nm	$3090
Casella Microdust Pro	10 to 2500,000 µg/m³	Light source: 880nm Narrow scattering angle: 12 to 20°	$4580

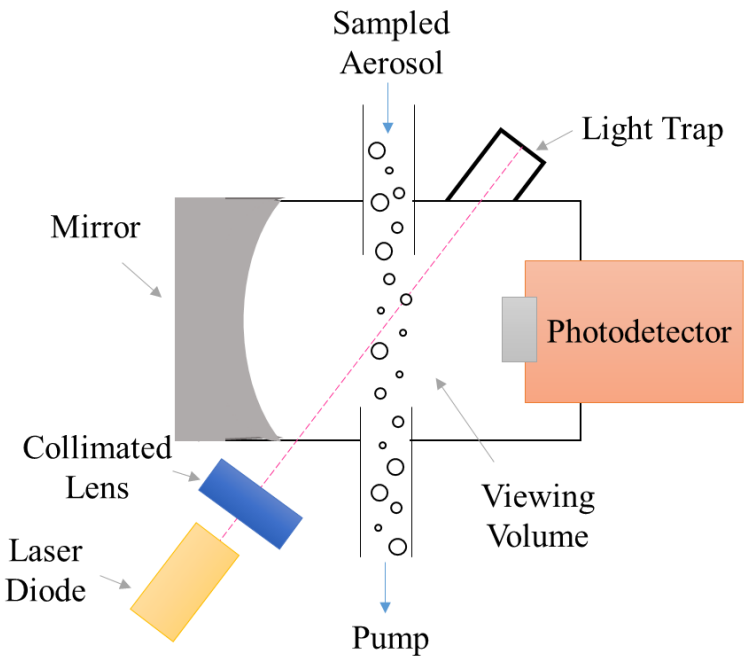

Figure 2 - 3 Schematic diagram of a photometer

The DustTrak DRX Aerosol Monitor (Model 8533 and 8534, TSI Inc) is the most representative photometer-type PM sensor (Wang et al., 2009). It uses the collimated laser beam with a wavelength of 655nm, and the scattering angle range is of 90 ± 62°. A gold-

coated spherical mirror can help to capture the scattering light and focus that onto a photodetector. Since these DustTrak monitors combines the photometric and optical pulse measurements, they can estimate higher aerosol mass concentration and provide more accurate mass concentration information. Photometric PM monitors have advantages over the mechanical-type PM monitors: no filter replacement, small in size, light in weight and relatively inexpensive. However, they also have their own limitations: the readouts are material dependent, and they cannot measure particles that are much smaller than the wavelength of the laser diode.

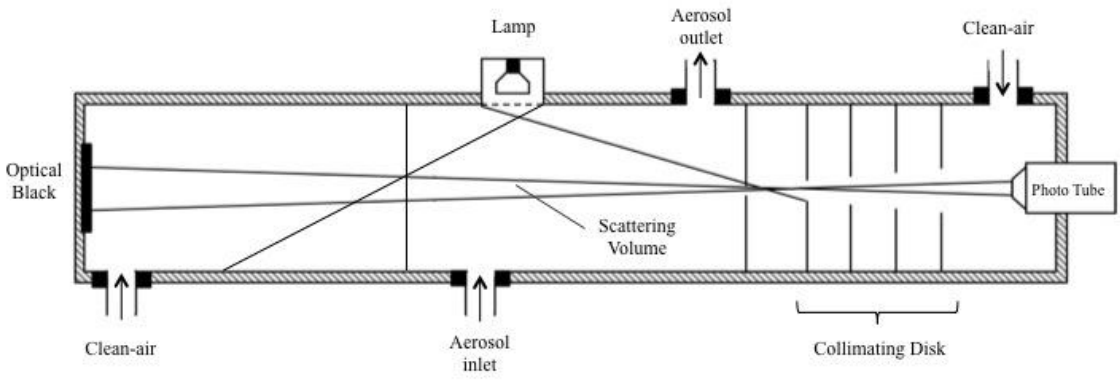

Figure 2 - 4 Schematic diagram of an integrating nephelometer. (Chen, D.C. and Pui, D. Y. H., 2013)

Figure 2-4 shows the schematic diagram of an integrating nephelometer. Particles entering the sensing volume are illuminated by a lamp. After passing a series of collimating disks, the scattered light from the particles is collected by the photoreceptor at a wide, off-axis angle. The signals of photoreceptor show a good relationship with the atmospheric mass concentration (Waggoner and Charlson, 1976; Butcher and Charlson, 1972). However, the scattered light would be attenuated when using the nephelometer for sooty particles measurement due to light absorption, which results in underestimation of mass concentration.

2.1.3 Electrical means

Figure 2 - 5 Simple schematic diagram of an electrical-based PM mass monitor

By manipulating the electrostatic charge of particles, the electrical method was proposed for PM mass concentration measurement. Figure 2-5 shows the simple schematic diagram of an electrical PM mass monitor. A charger, an ion trap and a current monitor are the three main components in an electrical-based monitor. As a high corona zone established by the charger, particles are charged by the ion attachment. Excess ions are removed by the ion trap, and the charged particles are then collected and detected as the electric current. The current is usually defined as the "escaping current," since it is measured at the exit of the function zone. Since the escaping current is proportional to the PM concentration, the measured current value is correlated to the particle mass concentration.

The Dekati mass monitor (DMM) and eFilter (Dekati Ltd., Finland) and Pegasor Particle Sensor (PPS, Pegasor Oy Ltd., Finland) are commercially available electrical mass sensors. In the DMM, a six-stage cascade low-pressure impactor is followed by the diffusion charger, classified the particles according to their aerodynamic diameters (Lehmann et al., 2004; Mamakos et al., 2006). In each stage, the current carried on these particles is measured. Since the charge per particle is obtained by charger evaluation, combined with the measured current from each stage, the total mass concentration of the particles can be derived. In the eFilter, signals of the electrical sensor are empirically

correlated to the mass concentration, and a gravimetric PM filter is integrated with the electrical PM sensor, providing the average mass concentration during the sample time. The output signal of PPS is calibrated for the diesel and gasoline emission particles with fixed size distribution (Lanki et al., 2011).

Since the charger performance is less material dependent, these electrical-based PM sensors are less affected by the various materials of the measured particles (Dhaniyala, 2011). Besides, they also have advantages, such as fast response, high sensitivity and simple configuration, which enable them to become a better choice for PM measurement compared to the mechanical and optical methods. However, the measured signals from the existing electrical mass sensor are empirically correlated the mass concentration, which might lead to huge error in measuring particles with large size distribution variation.

2.2 PM surface area measurement

Recent studies on nanoparticle toxicity have found the surface area of the nanoparticles strongly related to biological responses on human and animal lung cells. To better assess the health effect resulting from particle exposure, particle surface area has recently been proposed as a possible metric. Several techniques have been developed to measure the surface area of the particles.

Epiphaniometer, developed by Gäggeler in 1986, is one of the techniques capable of continuously measuring surface area (Gäggeler et al, 1986). Particles are sampled into a chamber containing radioactive lead isotopes (^{211}Pb), which is produced by the decay of a radon isotope (^{219}Rn). A capillary is used to remove the non-attached lead atoms, while the particles tagged by the lead atom are sampled on a filter. An α-detector is used to measure

the radioactivity on the filter. The radioactivity signal is proportional to the aerosol surface concentration. Due to the short half-life of ^{211}Pb, there is no need to change the filter during the monitoring process. Note that, the signal from the device is not correlated to the actual particle surface area, but the "active surface area" or "Fuchs surface area". The active surface area is defined as the surface of a particle that is involved in interaction with the surrounding gas (Keller et al., 2001). Because of the inclusion of a radioactive source, epiphaniometer is not commonly used, and the device is discontinued as a commercial product.

Another technique used for surface area concentration monitoring is based on diffusion charging, categorized as "diffusion charging sensor." LQ1-DC (Matter Engineering, Switzerland), DC2000CE (Ecochem, USA) and Nanoparticle Surface Area Monitor (NSAM; Model 3550, TSI Inc) are three commercial diffusion charging sensors for surface area monitors. However, the LQ1-DC is discontinued as a commercial product. Further, the DC2000CE has been used for measuring particles in the workplace (Vosburgh, 2014). The first two sensors (i.e., the LQ1-DC and DC2000CE) measure the active surface area, while the signal reported from the NSAM is correlated to lung-deposited surface area, which is defined as the surface of particles deposited in the alveolar or tracheobronchial region according to the deposition efficiency reported on the ICRP curve (Fissan et al., 2007). Figure 2-6 shows the schematic diagram of the NSAM. It is a jet-based diffusion charger sensor. Particle flow is sampled and split into two streams: one stream enters the charging chamber directly, while the other flow passes through the activated carbon filter and a HEPA filter, then carries the ions from corona zone into the charging chamber. After being mixed in the charging chamber, the combined aerosol flow is passed through the ion

trap and collected by a Faraday cage electrometer. By varying the voltage set on the ion trap, the measured signal can be correlated to lung-deposited surface area for the alveolar region or for the tracheobronchial region, respectively (Shin et al, 2007; Ntziachristos et al, 2007; Li et al., 2009). A portable version of NSAM is also available in the market as Aerotrak 9000 (TSI Inc).

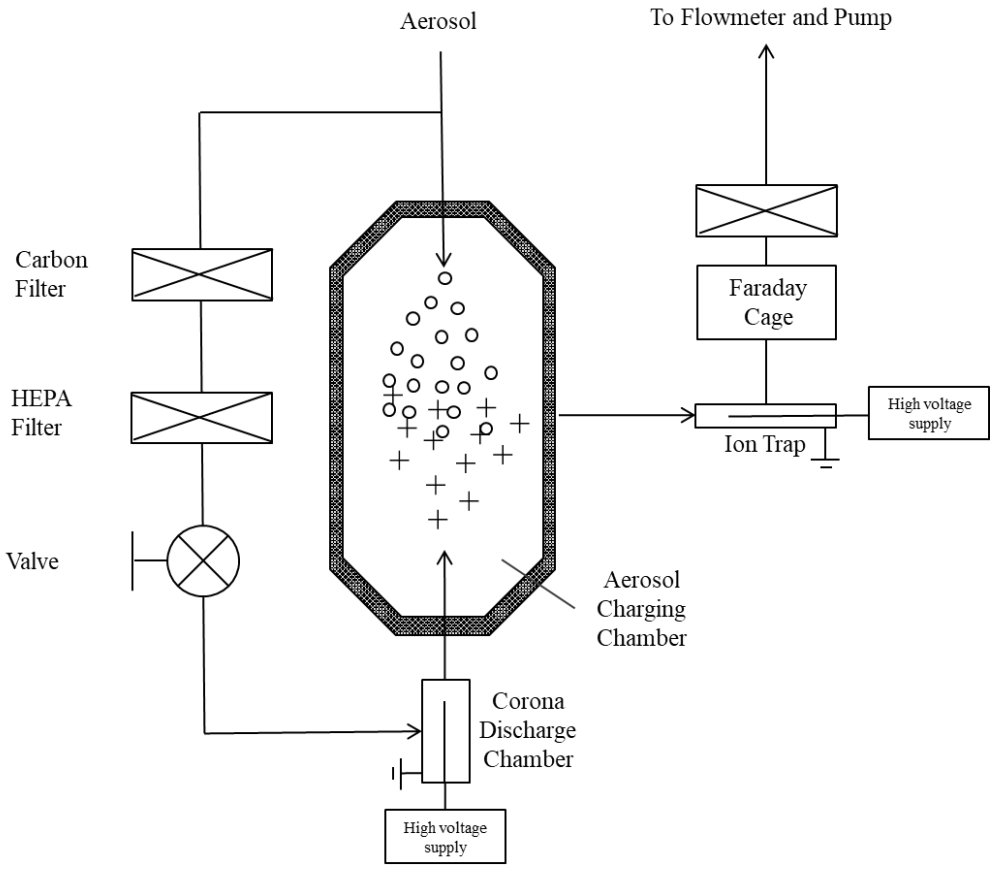

Figure 2 - 6 Schematic diagram of the nanometer surface area monitor (NSAM). (Chen, D.C. and Pui, D. Y. H., 2013)

2.3 Reference

Butcher, S. and R. Charlson "An Introduction to Air Chemistry (Academic, New York, 1972)." Google Scholar.

Chen, D.C. and Pui, D. Y. H., (2013). “Aerosol Instrumentation”. In Aerosol Science: Technology and Applications, edited by Ian Colbeck and Mihalis Lazaridis, 61-87. New York, UNITED KINGDOM, John Wiley & Sons, Incorporated.

Daley, P. S. and D. A. Lundgren (1975). "The performance of piezoelectric crystal sensors used to determine aerosol mass concentrations." American Industrial Hygiene Association Journal 36(7): 518-532.

Dhaniyala, S (2011). “Instrument based on electrical detection of aerosols”. In Aerosol measurement: principles, techniques, and applications, edited by P. Kulkarni, P.A. Baron and K. Willeke, 393-416. New York, UNITED KINGDOM, John Wiley & Sons, Incorporated.

Fissan, H., et al. (2007). "Rationale and principle of an instrument measuring lung deposited nanoparticle surface area." Journal of Nanoparticle Research 9(1): 53-59.

Gäggeler, H. W., et al. (1989). "Applications of the epiphaniometer to environmental aerosol studies." Journal of Aerosol Science 20(8): 1225-1228.

Görner, P., et al. (1995). "Photometer measurement of polydisperse aerosols." Journal of Aerosol Science 26(8): 1281-1302.

Keller, A., et al. (2001). "Surface science with nanosized particles in a carrier gas." Journal of Vacuum Science & Technology A: Vacuum, Surfaces, and Films 19(1): 1-8.

Lanki, T., et al. (2011). An electrical sensor for long-term monitoring of ultrafine particles in workplaces. Journal of Physics: Conference Series, IOP Publishing.

Lehmann, U., et al. (2004). "New Method for Time-Resolved Diesel Engine Exhaust Particle Mass Measurement." Environmental Science & Technology 38(21): 5704-5711.

Li, L., et al. (2009). "Evaluation of an electrical aerosol detector (EAD) for the aerosol integral parameter measurement." Journal of Electrostatics 67(5): 765-773.

Mamakos, A., et al. (2006). "Evaluation of the Dekati Mass Monitor for the Measurement of Exhaust Particle Mass Emissions." Environmental Science & Technology 40(15): 4739-4745.

Ntziachristos, L., et al. (2007). "Application of a Diffusion Charger for the Measurement of Particle Surface Concentration in Different Environments." Aerosol Science and Technology 41(6): 571-580.

Patashnick, H. and E. G. Rupprecht (1991). "Continuous PM-10 Measurements Using the Tapered Element Oscillating Microbalance." Journal of the Air & Waste Management Association 41(8): 1079-1083.

Pui, D. Y. H. (1996). "Direct-reading instrumentation for workplace aerosol measurements. A review." Analyst 121(9): 1215-1224.

Sem, G. J., et al. (1977). "Performance of the piezoelectric microbalance respirable aerosol sensor." American Industrial Hygiene Association Journal 38(11): 580-588.

Shin, W. G., et al. (2007). "Calibration and numerical simulation of Nanoparticle Surface Area Monitor (TSI Model 3550 NSAM)." Journal of Nanoparticle Research 9(1): 61-69.

Volkwein, J., et al. (2004). "Performance of a new personal respirable dust monitor for mine use." Report of Investigations 9663: 1-25.

Volkwein, C., et al. (2006). "Laboratory and field performance of a continuously measuring personal respirable dust monitor."

Vosburgh, D. J. H., et al. (2014). "Evaluation of a Diffusion Charger for Measuring Aerosols in a Workplace." Annals of Occupational Hygiene 58(4): 424-436.

Waggoner, A. and R. Charlson (1976). "Measurements of aerosol optical parameters." Fine Particles: 511-534.

Wang, X., et al. (2009). "A Novel Optical Instrument for Estimating Size Segregated Aerosol Mass Concentration in Real Time." Aerosol Science and Technology 43(9): 939-950.

Ward, M. D. and D. A. Buttry (1990). "In situ interfacial mass detection with piezoelectric transducers." Science 249(4972): 1000-1007.

CHAPTER 3 Evaluation of existed PM sensors

3.1 Introduction

The increasing awareness of adverse effect on the public health, caused by the exposure to particular matter (PM) in highly-polluted countries, such as China and India, has motivated the recent development of portable and personal sensors for monitoring the mass concentration of PM2.5 (defined as PM with the particle sizes less than 2.5 □m, i.e., fine particles). Sources of fine PM are present in our daily life, e.g., in industrial discharge, vehicle exhaust and commercial kitchen emission. The mass concentration of fine PM has been linked to the frequent occurrence of asthma, particularly for children and elders (Norris et al. 1999, Fan et al. 2015), and the cardiovascular-disease-related mortality and mortality (Brook et al., 2010). The increased rate of lung cancer cases has also been associated with the increased exposure of fine particles (Cohen and Pope 1995, Nyberg et al. 2000, Borm et al. 2004, Knaapen et al. 2004, Tie et al. 2009). In addition to its adverse public health effect, fine PM, once released, also increased the environmental burden (Dockery et al. 1993; Krewski, 2009; Evans et al. 2013; Potera, 2014).

Scientific instruments for measuring PM mass concentration are readily available in market. They are in general large in its final package and expensive for the ownership. As a result, it is not feasible to apply these scientific instruments for simultaneously monitoring the PM concentration at multiple sites. Monitoring the spatial distribution of PM in time for providing a better picture on the transient particle pollution status are required in recent air pollution study and control (Gao et al. 2015). More, the better correlation of PM exposure to related-heath data in epidemiology study requires the

measurement of PM exposure at the personal level. PM sensors in small packages and at low cost are thus in high demand.

Filter-based samplers are reliable devices for measuring the mass concentration of PM in the ambience. The requirement of offline gravimetric analysis to get the final particle mass concentration data makes them inconvenient and time-consuming in use. Direct-reading PM sensors, based on either the mechanical or optical operation principle, have thus been developed (Roessler 1982). Examples of mechanical PM monitors are the quartz crystal microbalance (QCM) (Alder and McCallum 1983) and Tapered Element Oscillating Microbalance (TEOM) (Patashnick and Rupprecht 1991). These mechanical monitors can be of high accuracy and independent of the size distribution and composition of PM. Photometers/nephelometers are representative instruments based on the light scattering. The simple configuration and continuous miniaturization/reduction of key components' makes optical PM sensors light in weight, compact in sizes and low in cost. Unfortunately, the performances of optical PM sensors are strongly dependent on the size distribution and composition of ambient particles.

Studies have been reported on the performance evaluation of low-cost optical PM sensors (Holstius, Pillarisetti et al. 2014, Austin et al. 2015, Wang et al. 2015, Sousan et al. 2016). All these studies reported a good linear relationship between the PM mass concentration and the responses of optical PM sensors. However, scanning mobility particle sizers (SMPSs), aerodynamic particle sizer (APS), SidePak or DustTrak was applied in these studies as the reference instruments for particle mass concentration measurement. SMPS/APS does not directly measure the mass concentration of PM. Instead, the mass concentration of PM was calculated from the measured number-based particle

size distributions under the assumption that particles are spherical and particle density is known. More critically, the error associated with calculated mass concentration is often amplified in the calculation with small measurement error in the number-based particle size distribution measurement. For example, a 5% in number-based particle size distribution can easily result in at least 15% error in mass/volume-based particle size distribution. The above calculation error would be even higher if particles were agglomerates. The use of both SidePak and DustTrak as the reference are also problematic. It is because both are photometric sensors and all PM sensors evaluated in previous studies are based on the same operation principle. Further, some of previous studies carried out the evaluation under the condition with transient particle mass concentration. With the consideration of measuring cycles for a SMPS /APS, the time delay between the responses of reference and evaluated PM sensors could result in the potential error in the sensor performance calibration. It is thus necessary to perform the calibration of PM sensors via proper reference instruments and under the conditions of steady particle mass concentration.

In this chapter, the performance of four low-cost optical PM sensors, i.e., Sharp, Shinyei, Samyoung and Oneair, one Personal Dust Monitor (PDM; Thermal Scientific) and one DustTrak (TSI Inc.) were calibrated using lab-generated particles in the size distributions of different mean sizes, geometrical standard deviation and composition, and under the condition of steady-state particle concentration. The scientific TEOM (Model 1405) was applied as the reference instrument.

3.2 Selection of PM sensors and reference

Table 3 - 1 Specification of low-cost sensors and portable PM sensors.

	Low-cost Sensors				**Portable Sensors**	
Sensor	Sharp	Shinyei	Samyoung	Oneair	Personal Dust Monitor	Dustrak
Model #	GP2Y1010AU0F	PPD42NS	DSM501A	CP-15-A4	PDM3700	8533
Size(mm)	46×30×18	59×45×22	59×45×20	45×35×23	243×172×83	135×216×224
Sampling method	Self diffusion	Thermal Convection	Thermal Convection	Active Sampling (Fan)	Pump sampling	Pump sampling
Detection Principle	Optical	Optical	Optical	Optical	Vibration	Optical
Detectable size range	N/A	~ 1.0 μm	~ 1.0 μm	0.3 ~ 10.0 μm	< 4.5 μm	PM_1, $PM_{2.5}$, PM_{10}, TSP
Concentration range	0.5 mg/m^3	28,000 #/L	1.4 mg/m^3	6 mg/m^3	200 mg/m^3	150 mg/m^3
Output signal	Analog output	Pulse width modulation	Pulse width modulation	Mass concentration	Mass concentration	Mass concentration

Table 3-1 summarizes the specification of low-cost and portable PM sensors tested in this study. Four low-cost optical PM sensors, i.e., Shinyei PPD42NS, Samyoung DSM501A, Sharp GP2Y1010AU0F and Oneair CP-15-A4, were selected because of their popularity and compact sizes. All these low-cost optical PM sensors are based on light scattering technique. For the reference, the schematic configurations of four low-cost PM sensors, illustrating the aerosol openings and passage in each low-cost sensor, are given in Fig 3-1. Fig 3-1(a) is the basic configuration of Shinyei and Samyoung sensors (both sensors share the same configuration). The configurations of Sharp and Oneair sensors are in Fig 3-1(b) and (c), respectively. Note that the solid lines in the diagrams represent the openings on the sensor cover surface. The shaded area in each diagram, are the potential space occupied by particles. In each of these low-cost sensors, an infrared (IR) emitting diode was used as the light source and a phototransistor as the detector for scattered lights. The scattering angles of these low-cost optical PM sensors are of 90~120 degrees. As particles pass through the sensing volume, defined by the optical path of illumination light and viewing angle of the detector, the phototransistor measures photons scattered from particles once irradiated. Thermal-driven upwind flows are generated in both Shinyei and Samyoung PM sensors by electrically heating a resistor near the sensor inlet to sample particles through sensing volumes. As a result, above both sensors are instructed to install vertically with the inlet facing downward. An Arduino microcontroller was applied in our experiment to provide required voltages for the operation and the readout collection of all low-cost PM sensors.

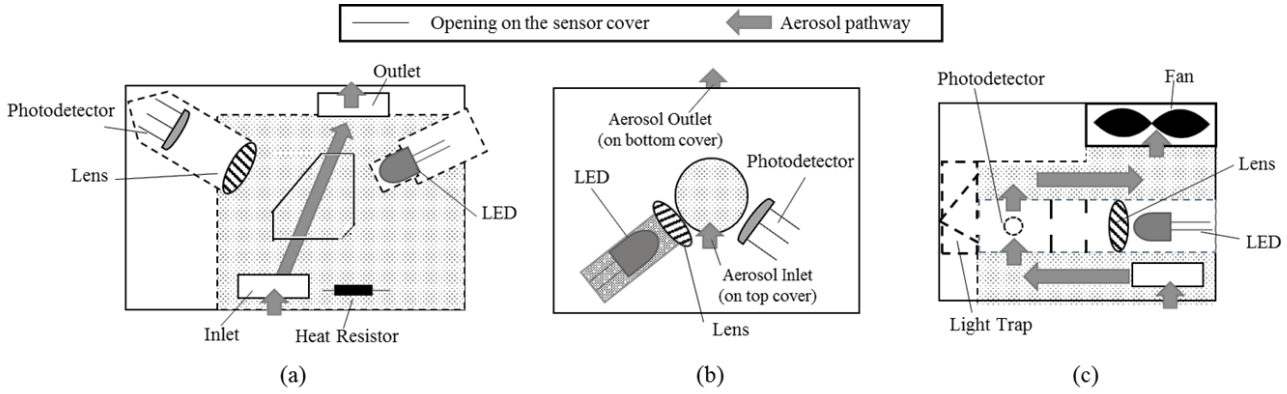

Figure 3 - 1 Schematic diagram of the low-cost sensor: (a) for Shinyei (Or Samyoung) sensor; (b) for Sharp sensor; (c) for Oneair sensor.

The readout of the Sharp sensor is an analog signal from its photodetector. The Sharp sensor outputs higher voltage signal as more scattered photons reach its detector. The readout of Oneair sensor is based on its built-in calibration curve, obtained by calibrating it against the readout of Dustrak II 8530 (TSI Inc.) in the factory. Different from Sharp and Oneair sensors, the readouts of both Shinyei and Samyoung sensors are so-called pulse-width modulated (PWM), i.e., these PM sensors only output a "High" state when particles are not present in the sensing volumes and a "Low" state when particles were present. The mass concentration of particles in the sensing volume is assumed to correlate with the low pulse occupancy ratio, which is calculated as $\frac{\#\ of\ low\ state\ output}{total\ \#\ of\ state\ output}$.

A DustTrak DRX Aerosol Monitor (TSI Model 8522) was also included in this experiment. Similar to four low-cost optical PM sensors, the DustTrak DRX measures particle mass concentration via light scattering technique. It operates at a total sampling flowrate of 3.0 liters/min (LPM), in which 1.0 LPM flow is filtered by a HEPA tube filter and used as sheath air. Different from IR emitting diodes in low-cost optical PM sensors, DustTrak DRX uses a laser diode with 655 nm in wavelength as its light source, and its light scattering angle is $90^o \pm 62^o$. A gold-coated spherical mirror is also included in the optical subsystem of DustTrak to collect the scattered photons in a wide angle and focus them onto its photodetector.

In addition to optical sensors, we included one mechanical PM sensor, i.e., Personal Dust Monitor (PDM model 3700; Thermo Fisher Scientific Inc.) in our study. The mechanical measurement principle of the PDM is the same as that of our reference instrument, i.e., tapered element oscillating microbalance, TEOM (Continuous Ambient

Particulate Monitor, Model 1405, Thermo Fisher Scientific Inc.). Both TEOM 1405 and PDM 3700 capture particles on a small disk filter located at the tapered end of an oscillating element. A tapered glass tube is used as the oscillating element in the TEOM 1405, while a deformed metal tube is in the PDM 3700. As particles are collected on the disk filter, the mass increase of disk filter leads reduces the vibrating frequency of tapered elements. PDM 3700 is a personal dust monitor for miners (by US NIOSH). The use of TEOM 1405 as the reference in our study is because it is a US EPA-approved instrument for measuring the mass concentration of ambient particulate matter (PM).

3.3 Experimental setup and testing conditions

Figure 3-2 shows the schematic diagram of experimental setup in this study. The setup included a large cylindrical test chamber (with the inner diameter, ID, of 30 cm), made of Plexiglas. A 4" PVC four-way connector was installed at the top of test chamber for introducing test particle stream and make-up clean air (if required) into the chamber. Test particles, once generated, were injected in the top opening of four-way connector. Makeup air flow was drawn in the connector from both side openings after passing through HEPA filter cartridges. A perforated metal plate was placed in the position near the bottom of test chamber to have uniform flow in the chamber. Two exits were designed at the chamber base to withdraw out the chamber flow. A valve and three external pumps were included in the setup to vary the total flow rate in test chamber. Seven tubes, for either mounting test optical PM sensors or as sampling probes are evenly spaced in the test chamber. Four low-cost optical PM sensors are vertically mounted on four tubes with one end sealed. The other three tubes are applied as sampling tubes for DustTrak, PDM and reference TEOM, which were placed directly underneath the test chamber.

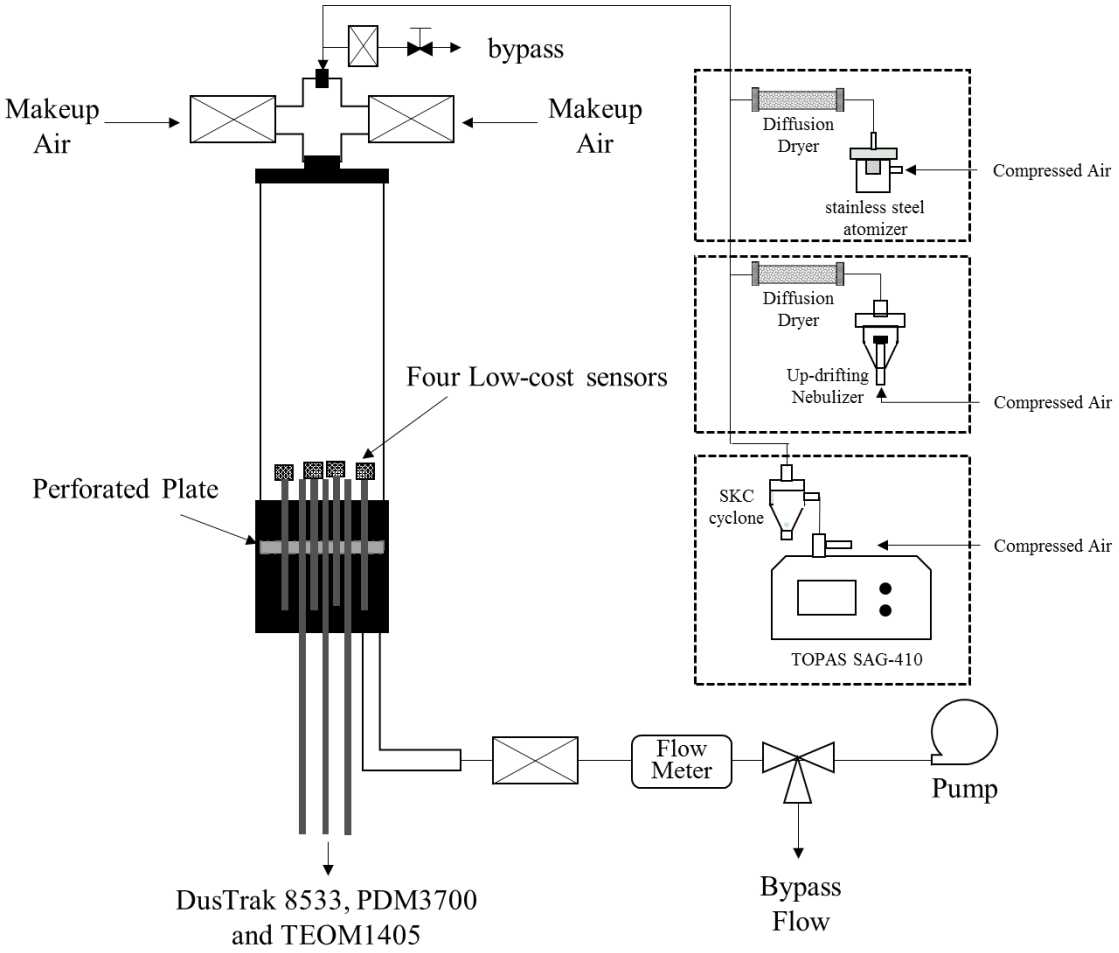

Figure 3 - 2 Schematic diagram of the calibration setup used in this study.

Aerosol generators of three different types were utilized to generate/airborne test particles. For test particles in the sub-micrometer size range, a custom-made Collison atomizer was used to produce droplets of different mean sizes by nebulizing solutions in different salt concentrations (i.e., Sodium Chloride, SC; Methylene blue, MB; and Fluorescein sodium, FS). An up-drifting nebulizer was also applied to generate droplets with the size distributions of the same peak sizes, but different standard deviations as those produced by the Collison atomizer. Droplets, once generated, were then passed through a diffusion dryer (with silica gel as the desiccant) to completely vaporize solvents in droplets prior to entering the 4-way connector. For test particles in the super-micrometer size range, a dust disperser (TOPAS SAG 410/U) was applied to airboren test dusts, i.e., A2 fine dust (or Arizona road dust, ARD), and a mixed dust (i.e., ARD and 2.5% ASHRAE #1 test dusts). A SKC cyclone was installed at the downstream of dust disperser to remove dust particles with the sizes larger than 2.5 μm (in a majority of experimental runs). A bypass for the particle stream was also included in our setup to release a portion of test particle stream prior to entering the 4-way connector. The mass concentration of particles in the test chamber was varied by adjusting both flowrates of particle stream and clean makeup air entering the connector.

Before our calibration, the spatial uniformity of particle concentration in the test chamber was characterized via DustTrak by taking the sequential measurement of particles sampled from each of seven tubes. The variation of measured particle concentration readings was in general less than 10%.

In this study, all PM sensors were primarily evaluated under steady particle concentration conditions. In the last part of our study, we further studied the calibration of

low-cost optical PM sensors under the calm air condition. For such calibration, test particles at desired high mass concentration were first filled up in the test chamber by flowing a stream of particles in high mass concentration in the chamber. External vacuum pumps and a particle generator were turn off once particles in high particle concentration was achieved in the test chamber. The mass concentration of particles in the test chamber was decayed as the function of time because of particle loss and general sampling flow of reference TEOM. The readings of low-cost optical PM sensors were taken until the mass concentration of test particles reduced to an undetectable level.

3.4 Experiment Results

In this study, we evaluated the performance of all selected PM sensors using polydisperse particles of different mass concentrations, mean sizes (D_p), geometrical standard deviation (σ_g), and compositions. The calibration of tested PM sensors was carried out under the conditions of steady-state particle mass concentration.

Note that the performance calibration of tested PDM is only reported herein in this article although it was included in our study (for the sake of paper saving). It is because that we obtained the same result in all our experimental runs when comparing the PDM readouts with reference TEOM readouts. A typical comparison of PDM and reference TEOM readings is shown in Figure 3: a) in wide mass concentration range (0~1000 $\mu g/m^3$) and b) in low concentration range (0~300 μg/m3). In this particular case, ARD was used as test particles. Good agreement between the readouts of PDM and TEOM is clearly evidenced in Fig 3-3a. However, the calibration data shown in Fig 3-3b indicates that the PDM lost its detection sensitivity when the mass concentration of ARD was less than 300

μg/m^3. The loss of detection sensitivity in low particle mass concentration for PDM is not a surprise given the consideration of its use of a deformed metal tube as the oscillating element.

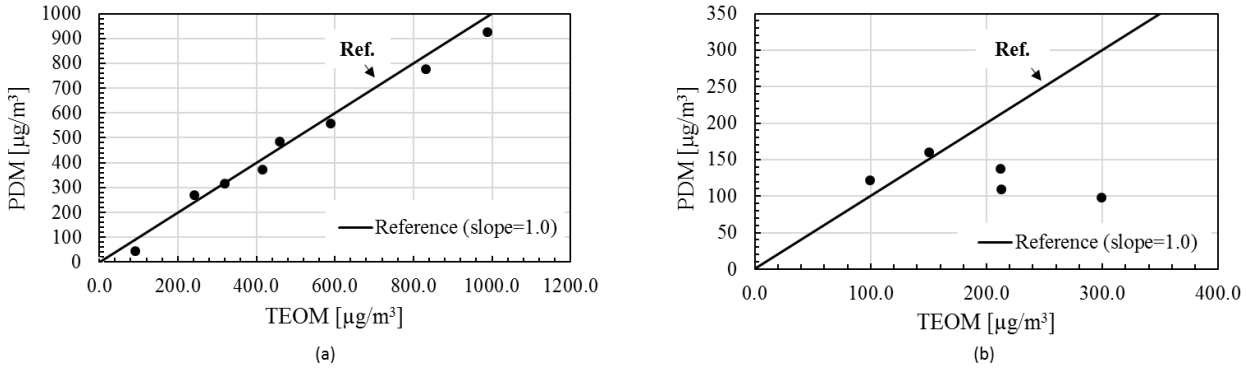

Figure 3 - 3 Comparison of PDM and TEOM readouts: (a) in high concentration range; (b) in the low concentration range.

3.4.1 Effect of the peak particle size

Test polydisperse particles in both sub-micrometers and super-micrometers were produced for this evaluation. For test particles in sub-micrometers, a custom-made Collison atomizer was applied to generate test particles by atomizing sodium chloride (NaCl) solutions in different volumetric concentrations. According to the measurement by the scanning mobility particle sizer (SMPS: TSI DMA 3081 with the platform model 3080), the number-based mean particle sizes, D_p, of test particles generated were 70, 86 and 95.0 nm, resulted from atomizing sodium chloride solutions of 0.1%, 0.5% and 1.0% by mass, respectively. To generate test particles in super-micrometers, ARD was airborne by a TOPAS powder disperser. Two different samples of test particles were used in this part of the calibration: one particle sample was obtained after passing through the SKC cyclone (to remove ones in the sizes larger than 2.5 μm) and the other sample obtained without the cyclone in the setup.

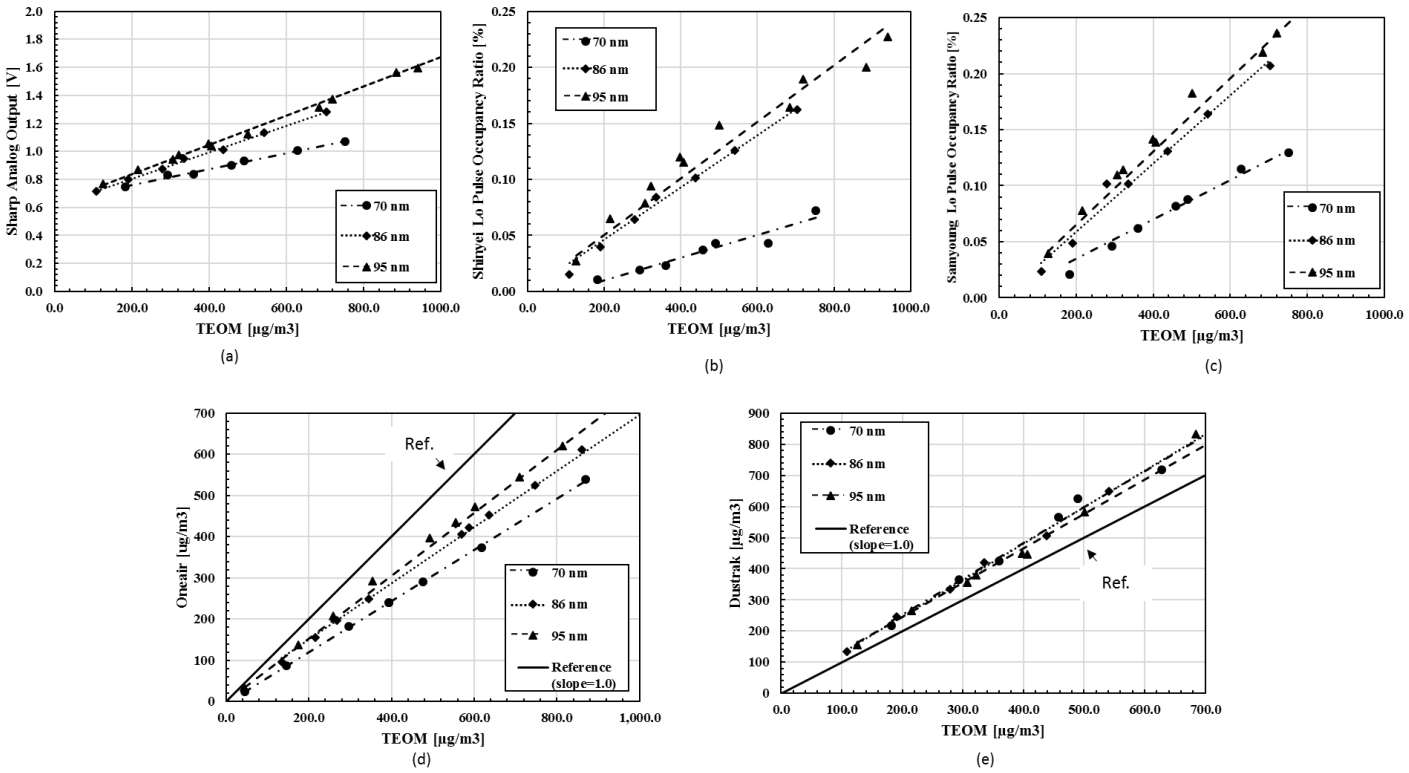

Figure 3 - 4 Calibration of optical PM sensors under the challenge of submicrometer-sized particles in the size distribution of different mean particle sizes (the geometrical standard deviation and composition of test particles are fixed): (a) for Sharp sensor; (b) for Shinyei sensor; (c) for Samyoung sensor; (d) for Oneair sensor; (e) for TSI DustTrak.

Figure 3-4 shows the calibration of four low-cost optical PM sensors (i.e., Sharp, Shinyei, Samyoung and Oneair) and TSI DustTrak under the challenging of sub-micrometer-sized NaCl particles having three different peak sizes but the same geometrical standard deviation. As evidenced, the readouts of four low-cost optical PM sensors and DustTrak were linearly increased as the mass concentration of test particles was increased (under the tested particle mass concentration less than 1,000 $\mu g/m^3$). The calibration lines of four low-cost optical sensors were, however, different from that of DustTrak. For the same particle mass concentration, the readouts of all four low-cost sensors were higher when tested with particles having larger peak sizes. The above trend was not observed for DustTrak. The above difference in the PM sensor performances might be due to different light sources and optical arrangements in all optical PM sensors and DustTrak. An infrared emitting diode (with the wavelength of ~ 900 nm) was used as the light source in all four low-cost PM sensors. DustTrak, on the other hand, uses a laser diode with the wavelength of 655 nm as the source. Lights with shorter wavelengths enable DustTrak to measure particles of smaller sizes. A spherical mirror also was applied in DustTrak to collect scattered photons in a wide scattering angle and to focus them onto the photodetector. The above arrangement makes DustTrak less dependent on the mean size of test particles when compared with the performances of low-cost optical PM sensors. It is worth noting that, although the readout of DustTrak was negligibly dependent on the mean sizes of submicrometer-sized test particles, its mass reading was not the same as that of the reference TEOM (i.e., the slope of calibration line is not 1.0). The readout of DustTrak is higher than that of reference TEOM (by ~ 20%).

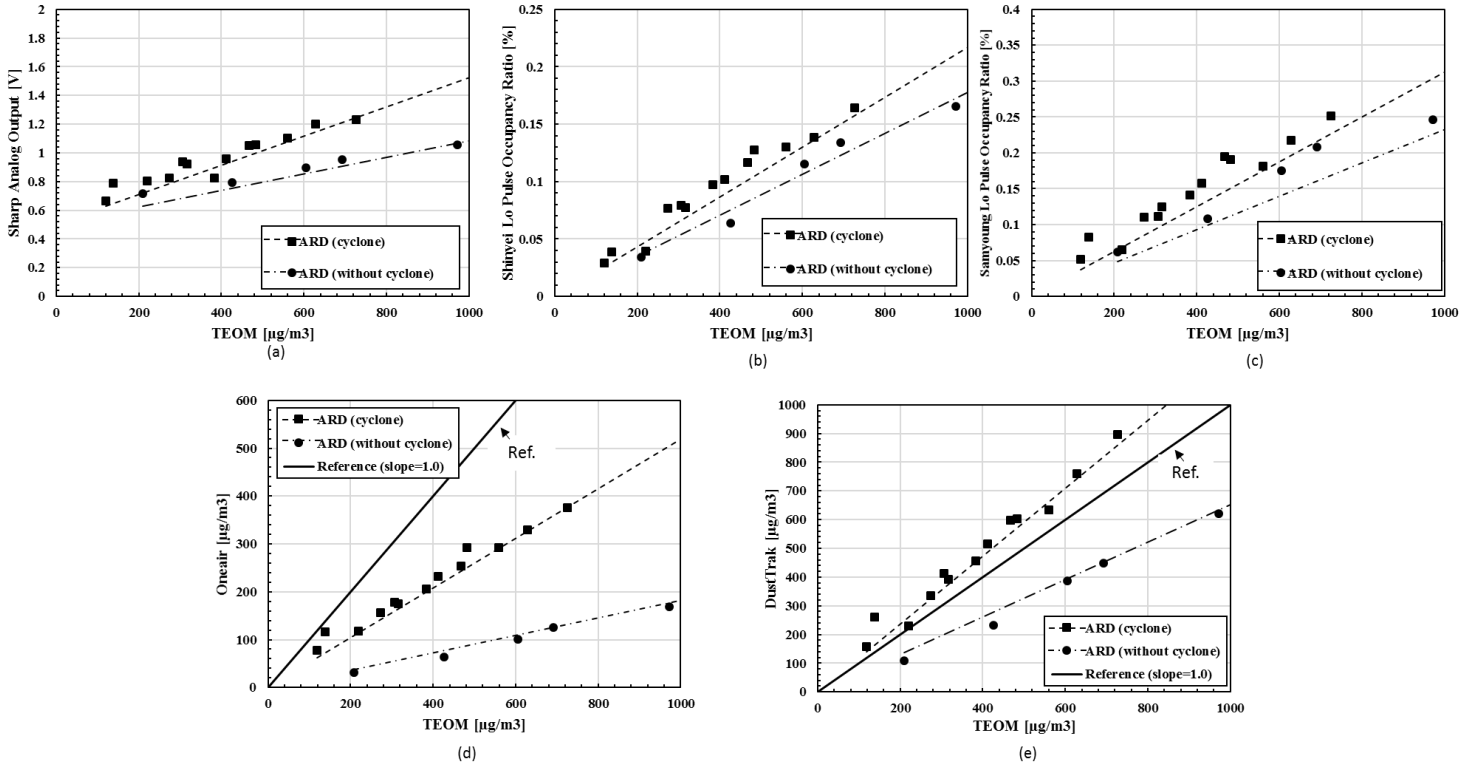

Figure 3 - 5 Performance of optical PM sensors under the testing of supermicrometer-szied particles with different mean particle size while keeping the same for geometrical standard deviation and composition): (a) for Sharp sensor; (b) for Shinyei sensor; (c) for Samyoung sensor; (d) for Oneair sensor; (e) for TSI DustTrak.

Figure 3-5 gives the calibration of four low-cost PM sensors and DustTrak under the challenge of super-micrometer particles. It is found that the slopes of calibration lines for all given PM sensors in the cases without particles in sizes larger than 2.5 μm were higher than those in the cases with particles in sizes larger than 2.5 μm. At the first look, the above finding is contradictory to what expected via the light scattering principle when large particles were present in the sensing volumes of low-cost optical PM sensors. The possible explanation for the above observation might be partially due to the sampling for low-cost optical PM sensors. Due to the inertia effect, particles with large sizes typically require a high flowrate to sample them into the sensing volumes of particle sensors. Gentle flow, moved by either the temperature gradient or a small fan in low-cost optical PM sensors, makes it difficult to sample large particles through their sensing volumes. Further, a small portion of large particles might be lost in the transport tubing for DustTrak. On the other hand, the iso-kinetic sampling was achieved for the reference TEOM to ensure the proper particle mass concentration measurement. As a result, the slopes of calibration lines for all the tested PM sensors are lower in the cases with large particles when compared with those in the cases without particles larger than 2.5 μm in sizes.

3.4.2 Effect of geometrical standard deviation

Two aerosol generators (i.e., custom-made Collison atomizer and updrifting nebulizer) were applied in this part of calibration to produce test particles having the same mean size of 76 ± 2 nm but different geometrical standard deviations (i.e., 1.802 and 2.486 respectively). The geometrical standard deviations of test particles were measured by TSI SMPS.

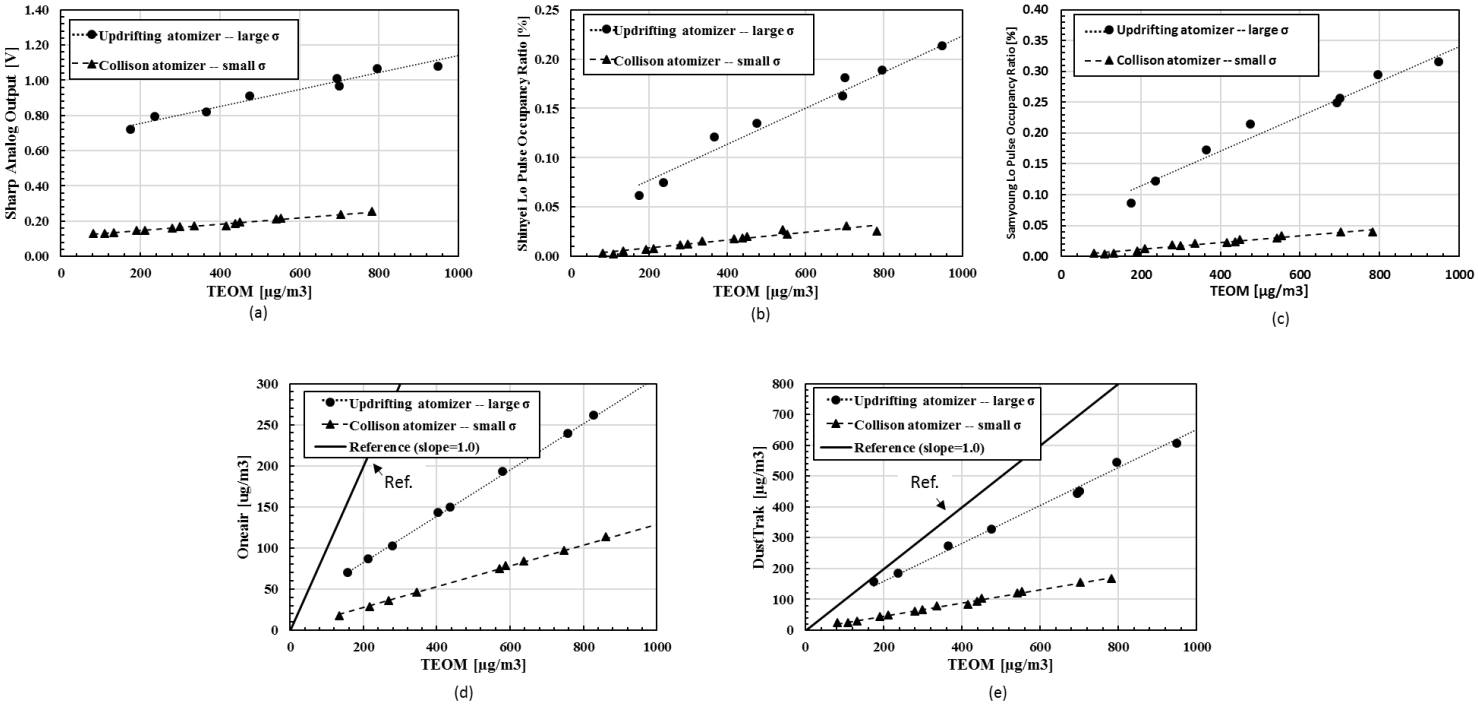

Figure 3 - 6 Performance of optical PM sensors under the testing of particles having different standard deviation values in size distributions (while keeping the particle composition and mean size the same): (a) for Sharp sensor; (b) for Shinyei sensor; (c) for Samyoung sensor; (d) for Oneair sensor; (e) for TSI DustTrak.

Figure 3-6 shows the performance calibration of all optical PM sensors when challenged by the above two samples of test particles. Notice that shown in the above figure is the normalized readouts as a function of the reference TEOM reading, instead of raw PM sensor readouts. The above normalization of PM readouts is because of different number concentrations of two test particle samples. As shown in Fig 3-6, the slopes of calibration lines for both test particle samples are again different. The larger the value of geometrical standard deviation of test particle samples, the higher the sensors' readouts. The above observation might be explained by the fact that more large particles are present in the test sample having a wide size distribution (i.e., large geometrical standard deviation value) compared to those in the test sample with a narrow size distribution. As a result, more particles of large sizes are present in sensing volumes of low-cost optical PM sensors when challenged with sample particles in a wide size distribution, resulting in more photon scattering.

A rough analysis was also carried out to understand the observed significant effect of geometrical standard deviation of particles. In this analysis, the light scattering from two samples of lognormal-size-distributed particles having the same total number concentration and peak size but two difference values of geometrical standard deviation (i.e., 1.8 and 2.5) were calculated. We assumed the wavelength of light source was 880 nm. The analysis further assume single particle scattering (i.e., no multiple light scattering) and 100% scattered light collection and detection. The Mie scattering program was used to compute the intensity of scattered light for particles in each size bin. The total scattered light was obtained by summing up the intensity in all the size bins. The above analysis shows that the total scattered intensity from the particle sample having the geometrical

standard deviation of 2.5 was a factor of 8 higher than that from particles with the geometrical standard deviation of 1.8. Under the consideration of multiple light scattering, multiple wavelengths of LED sources, and partial scattering angle light collection and detection, the above factor should be lower in the experimental observation. Indeed, a factor of 6 in the readouts was found in this part of calibration.

3.4.3 Effect of particle composition

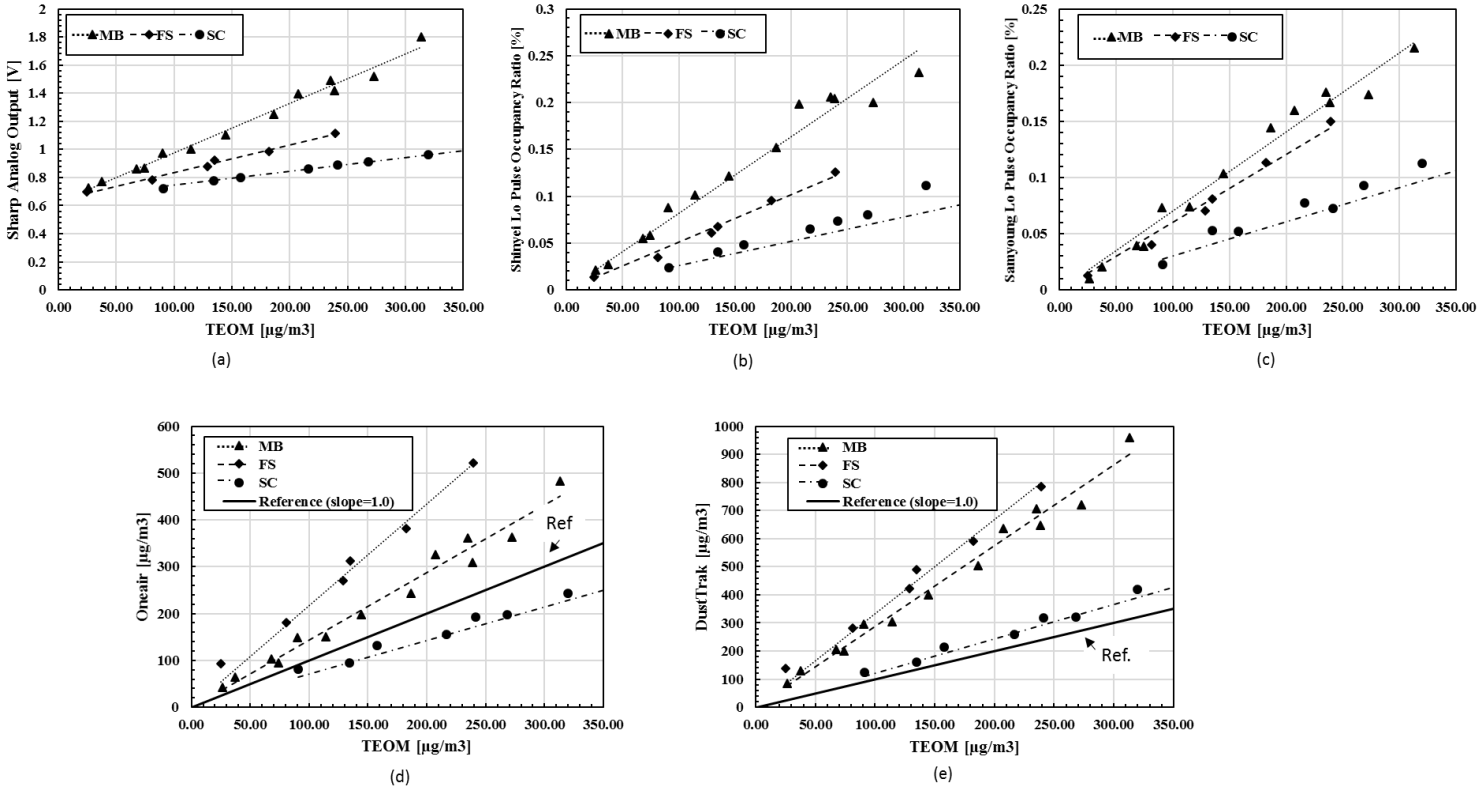

Figure 3 - 7 Performance of optical PM sensors under the testing of submicrometer-sized particles in three different compositions while keeping the mean size and geometrical standard deviation of size distributions constant: (a) for Sharp sensor; (b) for Shinyei sensor; (c) for Samyoung sensor; (d) Oneair sensor; (e) for TSI DustTrak.

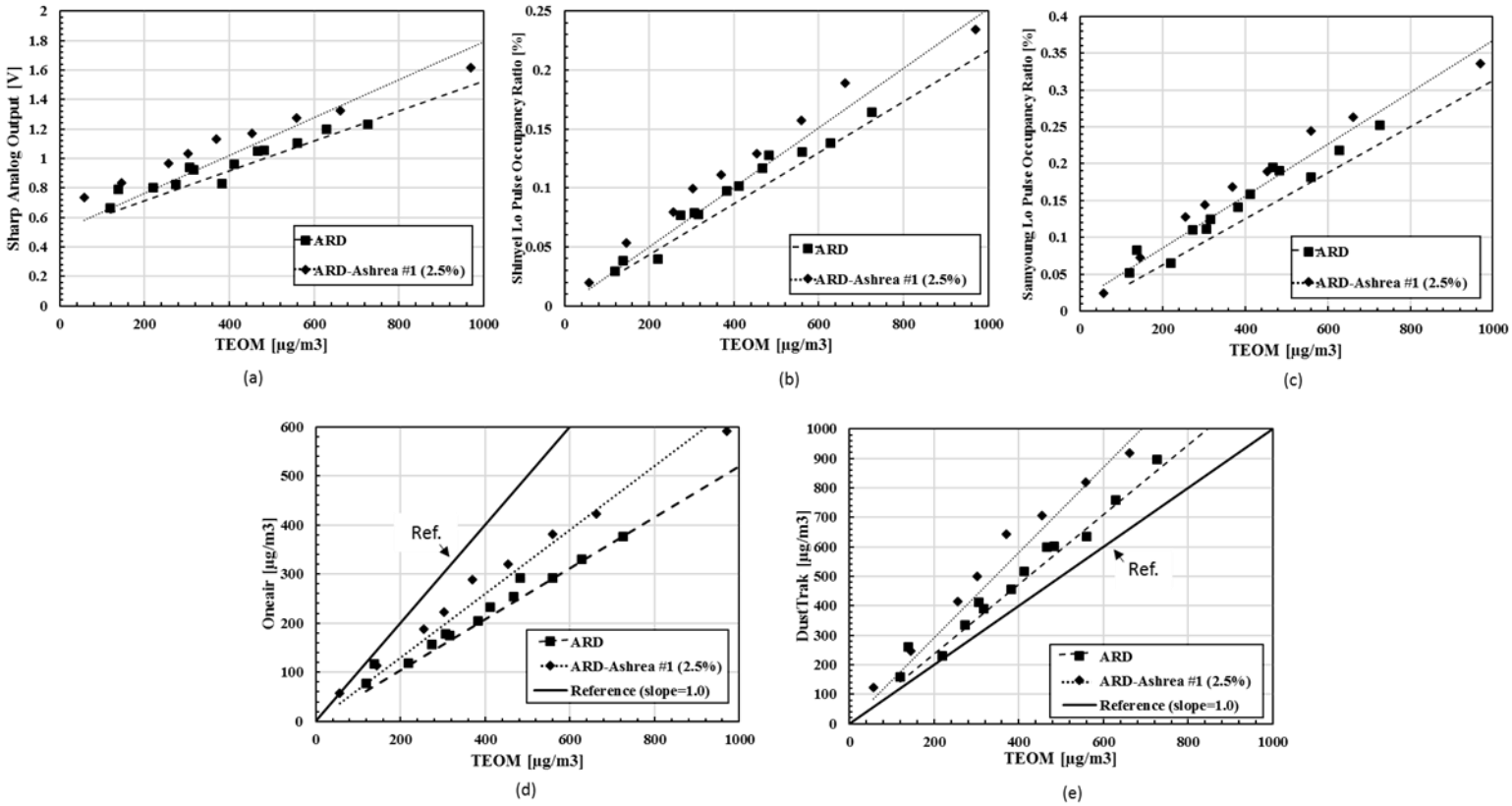

Figure 3 - 8 Performance of optical PM sensors under the testing of supermicrometer-sized particles in two different composition: (a) for Sharp sensor; (b) for Shinyei sensor; (c) for Samyoung sensor; (d) Oneair sensor; (e) for TSI DustTrak.

The material effect on the readouts of optical PM sensors was assessed using polydisperse submicrometer and supermicrometer particles of different compositions. For polydisperse submicrometer particles, the custom-made Collison atomizer was applied to produce them in three different compositions by spraying solutions of Methylene Blue (MB), Fluorescein Sodium (FS) and Sodium chlorine (NaCl), and completely evaporating solvents in generated droplets. The refractive indexes of MB, FS and NaCl at the red light wavelength are 1.55-0.6i, 1.364 and 1.544, respectively (Hinds, W. C. 1999). The calibration lines for four low-cost PM sensors and DustTrak are given in Figure 3-7. It is not a surprise that the composition of test particles has significant effect on the readouts of all optical PM sensors. The similar trend on the material dependence was observed in the performances of three low-cost optical PM sensors (i.e., Sharp, Shinyei and Samyoung): the highest slope of calibration lines is found in the cases with MB particles, lower slope for FS particles, and the lowest for NaCl particles. However, the calibration line slopes for both Oneair and DustTrak are the highest in the cases with FS particles and the lowest remain in the cases with NaCl particles. The above finding of the performance difference on the material dependence could be due to optical designs and the calibration curve of tested PM sensors.

In addition, we also dispersed ARD and a mix of ARD-ASHRAE #1 test dust (2.5%) in air to evaluate the optical PM sensor performance. Both samples of test particles were passed through the SKC cyclone to remove those with the sizes larger than 2.5 μm. The calibration result of studied PM sensors using the ARD and the particle mix is given in Figure 3-8. Again, the effect of particle material on the readouts of optical PM sensors was noticeable for super-micrometer particles of different compositions. At the same particle

mass concentration, the readouts for all test optical PM sensors were higher when challenged with the mixed particles compared to those in the cases with ARD only.

3.4.4 Performance calibration under steady and transient particle mass concentration conditions

Because of no/low sampling flowrates for three low-cost PM sensors (i.e., Sharp, Shinyei and Samyoung Sensors), it is worthwhile to compare the calibration results under the conditions of steady and transient particle mass concentration. In this last part of our investigation, we further evaluated the performance of optical PM sensors in calm air. In this part of experiment, the test chamber was first filled up with test particles in desired mass concentration by flowing test particles in test chamber and varying the makeup air flowrate. Once the particle mass concentration reached its steady state, the aerosol generator and vacuum pumps were turn off in the calm air testing. The particle mass concentration in the test chamber were slowly decreased because of particle loss and minor sampling flow driven by the reference TEOM. Submicrometer-sized NaCl particles were used in this testing.

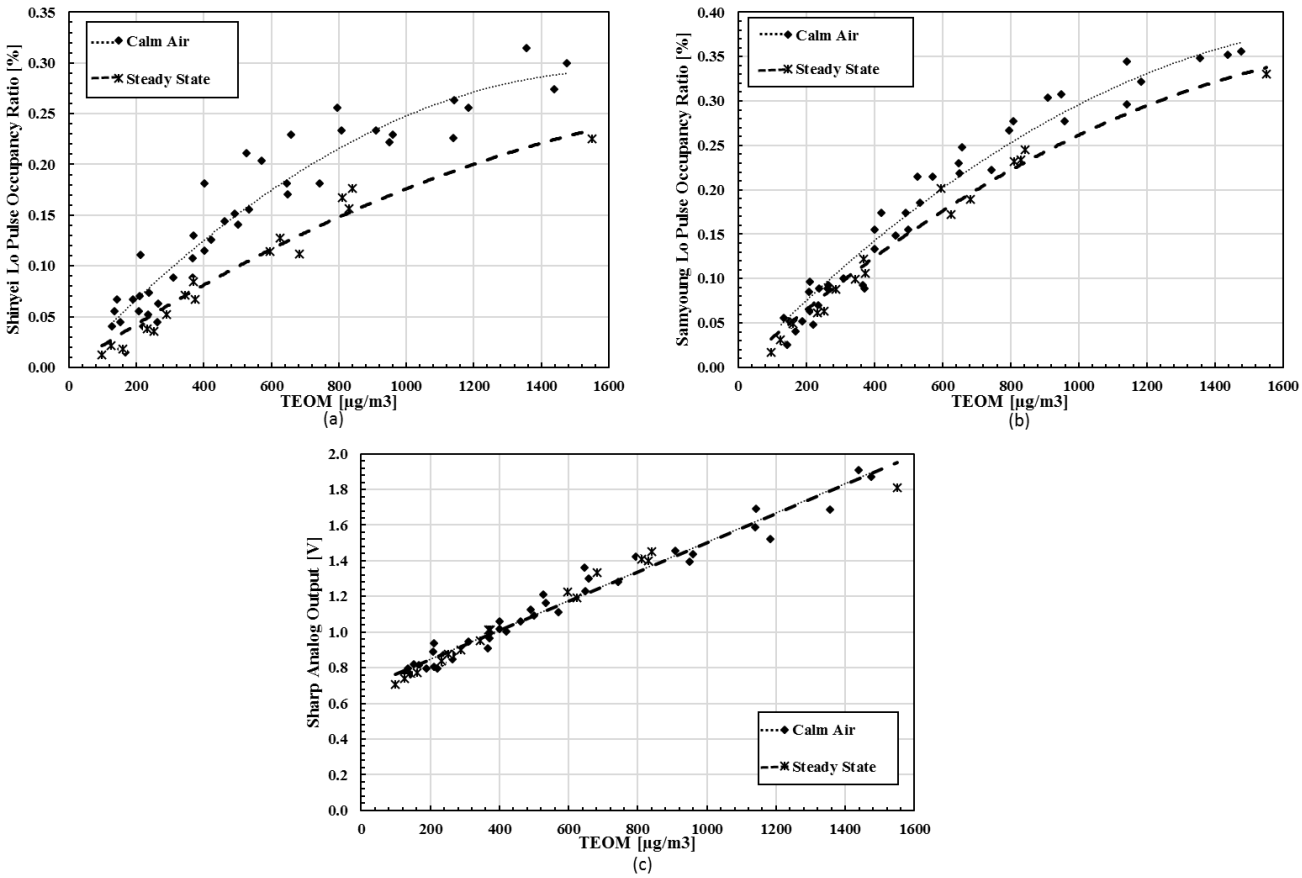

Figure 3 - 9 Comparison of the performance of low-cost optical PM sensors under the conditions of steady and transient particle mass concentrations: (a) for Samyoung sensor; (b) for Shinyei sensor; (c) for Sharp sensor.

Figure 3-9 shows the calibration result of the above three low-cost optical PM sensors under both calm air and steady-state particle mass concentration conditions. The given data shows that the readout of Sharp PM sensor maintains its linear calibration line at the particle concentration up to 1,600 $\mu g/m^3$ but the linearity of readouts for both Shinyei and Samyoung sensors was deteriorated as the increase of mass concentration.

It is also found that the slopes of Shinyei and Samyoung sensor calibration curves obtained under the calm air condition were in general higher than those obtained under the steady particle mass concentration condition while the difference for the Sharp sensor was negligible. The above finding might be partially attributed to the particle transport passage in both Shinyei and Samyoung sensors, having dead space in their passages. In the calm air testing, the test chamber and particle passages of low-cost PM sensors were initially filled up with particles in high concentration. Particles might be trapped in the dead space of particle passages inside Shinyei and Samyoung sensors. Because of slow sampling flow in both sensors, much long time was needed to synchronize the particle concentration in the dead spaces with that in the ambient. The above possibility could explain the high readouts of these two sensors when calibrated under calm air condition compared to those under steady particle mass concentration condition. The difference in the readouts under two testing conditions was not observed for Sharp sensor. It is because of its simple, straight-through particle passsage and our use of diffusive submicrometer-sized particles.

3.5 Conclusion

The performance of six PM sensors, including five optical and one mechanical PM sensors, i.e., Sharp, Shinyei, Samyoung, Oneair, TSI DustTrak and Personal Dust Monitor

(PDM), were calibrated under the steady particle mass concentration condition and using lab-generated particles of various physical and chemical properties, i.e., total mass concentration, peak size, geometrical standard deviation of particle size distribution, and particle composition. The scientific TEOM (Model 1405) was selected as the reference in this calibration. Our calibration result shows that the readouts of all test PM sensors are in the linear relationship with the particle mass concentration when challenged by particles having the fixed size distribution and composition. The response of PDM in general agrees well with the readout of reference TEOM for a particle mass concentration higher than 0.3 mg/m^3. The PDM lost its detection sensitivity for particles in the mass concentration less than 0.3 mg/m^3 because of the use of deformed metal tube as the oscillating element in a PDM. However, the readouts of all tested optical PM sensors are sensitive to the physical and chemical properties of test particles. In the cases without the sampling issue, the increase of mean particle size and standard deviation in the size distribution of test particles in the same material resulted in the readout increase for optical PM sensors. The composition of test particles (i.e., refractive index) also have significant effect on the readouts of optical PM sensors. The level of composition effect depends on the optical design of PM sensors. Our study further demonstrated that the calibration of low-cost optical PM sensors should be performed under the steady particle concentration condition, instead of the transient particle mass concentration condition even at very slow transient conditions (i.e., under calm air condition). It might be due to the presence of dead space in the particle passages of low-cost optical PM sensors. It is thus concluded that the proper interpretation of readouts from low-cost optical PM sensors requires users to calibrate them using representative ambient particles (which is often unknown) and under the steady-state

particle mass concentration. The potential sampling issue in the use of low-cost PM sensors should be also taken into the consideration when measuring large particles in the ambient.

3.6 Reference

Alder, J. F. and J. J. McCallum (1983). "Piezoelectric crystals for mass and chemical measurements. A review." Analyst 108(1291): 1169-1189.

Austin, E., I. Novosselov, E. Seto and M. G. Yost (2015). "Laboratory Evaluation of the Shinyei PPD42NS Low-Cost Particulate Matter Sensor." PLoS ONE 10(9): e0137789.

Borm, P. J., R. P. Schins and C. Albrecht (2004). "Inhaled particles and lung cancer, part B: paradigms and risk assessment." International Journal of Cancer 110(1): 3-14.

Brook, R. D., S. Rajagopalan, C. A. Pope, J. R. Brook, A. Bhatnagar, A. V. Diez-Roux, F. Holguin, Y. Hong, R. V. Luepker, M. A. Mittleman, A. Peters, D. Siscovick, S. C. Smith, L. Whitsel, J. D. Kaufman, o. b. o. t. A. H. A. C. o. Epidemiology, C. o. t. K. i. C. D. Prevention, P. A. Council on Nutrition and Metabolism (2010). "Particulate Matter Air Pollution and Cardiovascular Disease. An Update to the Scientific Statement From the American Heart Association." Circulation.

Cohen, A. J. and C. A. Pope (1995). "Lung cancer and air pollution." Environmental Health Perspectives 103(Suppl 8): 219-224.

Dockery, D. W., C. A. Pope , X. Xu , J. D. Spengler , J. H. Ware , M. E. Fay , B. G. J. Ferris and F. E. Speizer (1993). "An Association between Air Pollution and Mortality in Six U.S. Cities." New England Journal of Medicine 329(24): 1753-1759.

Evans, J., A. van Donkelaar, R. V. Martin, R. Burnett, D. G. Rainham, N. J. Birkett and D. Krewski (2013). "Estimates of global mortality attributable to particulate air pollution using satellite imagery." Environmental Research 120: 33-42.

Fan, J., S. Li, C. Fan, Z. Bai and K. Yang (2015). "The impact of PM2.5 on asthma emergency department visits: a systematic review and meta-analysis." Environmental Science and Pollution Research 23(1): 843-850.

Gao, M., J. Cao and E. Seto (2015). "A distributed network of low-cost continuous reading sensors to measure spatiotemporal variations of PM2.5 in Xi'an, China." Environmental Pollution 199: 56-65.

Hinds, W. C. (1999). Aerosol technology: properties, behaviour, and measurement of airborne particles. New York: Wiley.

Holstius, D. M., A. Pillarisetti, K. R. Smith and E. Seto (2014). "Field calibrations of a low-cost aerosol sensor at a regulatory monitoring site in California." Atmos. Meas. Tech. 7(4): 1121-1131.

Knaapen, A. M., P. J. Borm, C. Albrecht and R. P. Schins (2004). "Inhaled particles and lung cancer. Part A: Mechanisms." International Journal of Cancer 109(6): 799-809.

Krewski, D. (2009). "Evaluating the Effects of Ambient Air Pollution on Life Expectancy." New England Journal of Medicine 360(4): 413-415.

Norris, G., S. N. YoungPong, J. Q. Koenig, T. V. Larson, L. Sheppard and J. W. Stout (1999). "An association between fine particles and asthma emergency department visits for children in Seattle." Environmental Health Perspectives 107(6): 489-493.

Nyberg, F., P. Gustavsson, L. Järup, T. Bellander, N. Berglind, R. Jakobsson and G. Pershagen (2000). "Urban air pollution and lung cancer in Stockholm." Epidemiology 11(5): 487-495.

Patashnick, H. and E. G. Rupprecht (1991). "Continuous PM-10 Measurements Using the Tapered Element Oscillating Microbalance." Journal of the Air & Waste Management Association 41(8): 1079-1083.

Potera, C. (2014). "Toxicity beyond the Lung: Connecting PM(2.5), Inflammation, and Diabetes." Environmental Health Perspectives 122(1): A29-A29.

Roessler, D. M. (1982). "Diesel particle mass concentration by optical techniques." Applied Optics 21(22): 4077-4086.

Sousan, S., K. Koehler, G. Thomas, J. H. Park, M. Hillman, A. Halterman and T. M. Peters (2016). "Inter-comparison of low-cost sensors for measuring the mass concentration of occupational aerosols." Aerosol Science and Technology 50(5): 462-473.

Tie, X., D. Wu and G. Brasseur (2009). "Lung cancer mortality and exposure to atmospheric aerosol particles in Guangzhou, China." Atmospheric Environment 43(14): 2375-2377.

Wang, Y., J. Li, H. Jing, Q. Zhang, J. Jiang and P. Biswas (2015). "Laboratory Evaluation and Calibration of Three Low-Cost Particle Sensors for Particulate Matter Measurement." Aerosol Science and Technology 49(11): 1063-1077.

CHAPTER 4 Development of a new electrical PM sensor

4.1 Introduction

As more studies have revealed the deleterious health effects from both fine and ultrafine particles (Cohen and Pope, 1995; Pope et al., 2002; Potera, 2014; Lelieveld et al, 2015), the desire of development on PM instrument to monitor the particle concentration where the public are potentially to be exposed is increasing. Thus, a simple device capable of monitoring the integral parameters (i.e., total number, length, surface area and mass concentration) is needed. Because of the simple design and easy manipulation, "Electrical Aerosol Detector" (EAD) are proposed as a one of the popular technique for PM monitoring. One particle conditioner (i.e., charger) and one current monitor are the two main components in a EAD. The measured signal can be correlated to the aforementioned integral parameters.

Several personal monitors (DiSCmini, NanoTracer, Partector) based on unipolar charging are also used to assess the nanoparticle concentration (Marra et al, 2009 & 2010; Fierz et al, 2011 & 2014; Todea et al, 2017). Similar technique can be used to measure the total length concentration of particles: Electrical Aerosol Detector (EAD, Model 3070A, TSI Inc) is a commercial product to measure the total length concentration (i.e., the first moment of particle size distribution; Li et al, 2009). For the surface area measurement, the Nanoparticle Surface Area Monitor (NSAM, Model 3550) was carried out by TSI Inc, to measure the particle lung-deposited surface area (Shin et al, 2007; Ntziachristos et al, 2007). The design of NSAM is similar to the EAD. By varying the ion-trap voltage, the NSAM can measure the surface area concentration of particles deposited in the tracheobronchial

or alveolar region (Wilson et al, 2007). Besides, LQ1-DC (Matter Engineering, Switzerland) and DC2000CE (Ecochem, USA) were also developed to monitor the active surface area concentration, which is a fraction of the particle geometric surface area (Bau et al, 2012; Vosburgh, et al.,2014). Recently, some EAD were also developed to provide the particle mass concentration, such as eFilter (Dekati Ltd., Finland) and Pegasor Particle Sensor (PPS, Pegasor Oy Ltd., Finland; Amanatidis et al, 2013). However, most of the EAD mentioned above are semi-empirical instruments: the measure signal is simply correlated to the integral parameter, which the response can be trustable only if the sampled particles have similar size distribution. Thus, an EAD, in which the response is less affected by the particle size distribution variation, is needed.

Besides, none of the commercial EAD sensors measure the geometrical surface area. In fact, particle geometrical surface area is of great interest in many fields, such as toxicity of airborne particles, drug delivery and catalysts manufacturing. Cao et al developed a geometric surface area monitor by connected an electrostatic precipitator after the EAD mixing chamber, and measured the escaping current using a faraday cage electrometer in the downstream (2017). The measured signal was claimed to proportional to total surface area (i.e. d_p^2). However, the signal measured from the escaping current is not a pure power function of particle size, which could induce error during the measurement.

In this chapter, a new electrical PM sensor was developed, in which consist of a direct-type charger and a disk electrostatic precipitator. The signal was measured at the wall of the precipitator and the current was induced by the deposited particles. This was different from the previous EAD, in which a Faraday Cup was collected the charged particles exiting the device. By altering the operation parameters of each component, the measured signal

is aimed to proportional to either the geometrical surface area (i.e., the second moment of particle size distribution) or the volume (i.e., the third moment of particle size distribution).

4.2 Design of sensor

4.2.1 Overall concept

There are two main components in the new electrical PM sensor: a corona charger and an electrostatic precipitator. As particles sampled into the sensor, they are charged on the charging zone by ions attachment. Then, the charged particles go through the precipitator and some particles are precipitated due to electrical force. An sensitive electrometer is used to monitor the induced current on the precipitator wall. The response function of the electrical PM sensor is showed in below equation:

$$\mathrm{I} = \mathrm{e} * \mathrm{Q} * \sum_{i=1}^{n} N_i(dp) * n_{ave}(dp) * \eta_{ex}(dp) * P(dp) \qquad (4\text{-}1)$$

Where e is the elementary charge, $1.6 * 10^{-19}$ C; Q is operational flowrate through the electrostatic precipitator; N_i is the particle number concentration; n_{ave} is the average charge number on a particle; η_{ex} is the extrinsic charging efficiency of a particle passing though the charger; P is the precipitation efficiency of the particle under given voltage (i.e., percentage of particles deposited inside the precipitator). Additionally, the n_{ave} and η_{ex} are related to the charger performance, which can be determined by charger evaluation; P can be obtained by calibration results from the precipitator. All these three parameters are power functions of particle size dp.

For the particles integral property measurement, the total particle surface concentration and total volume concentration can be represented by the following two equations, respectively:

$$\mathrm{S} = \mathrm{Q} * \sum_{i=1}^{n} N_i(dp) * \frac{\pi * d_{p,i}^2}{4} \tag{4-2}$$

$$\mathrm{V} = \mathrm{Q} * \sum_{i=1}^{n} N_i(dp) * \frac{\pi * d_{p,i}^3}{6} \tag{4-3}$$

According to eq.(4-1), the relationship between the multiplication of n_{ave}, η_{ex} and P and particle size dp can be re-written as following:

$$\mathrm{I} = \mathrm{e} * \mathrm{Q} * \textstyle\sum_{i=1}^{n} N_i(dp) * k * D_p^x \tag{4-4}$$

Where $k * D_p^x$ is the multiplication of n_{ave}, η_{ex} and P; k is a constant coefficient, related to the performance of the charger and precipitator; x is the power of dp. If the value of x is equal to 2, which means the measured signal I is proportional to the total surface area of the sampling particles. Likewise, if the value of x is equal to 3, the measured signal I is thus proportional to the total volume of the sampling particles. The challenge in this study is to manipulate the performance of the charger and precipitator by altering the operation parameters (i.e., sampling flowrate, charger current, etc) to meet the desire index, such as particle total surface area (i.e., x=2) and total volume (i.e., x=3).

4.2.2 Charger design

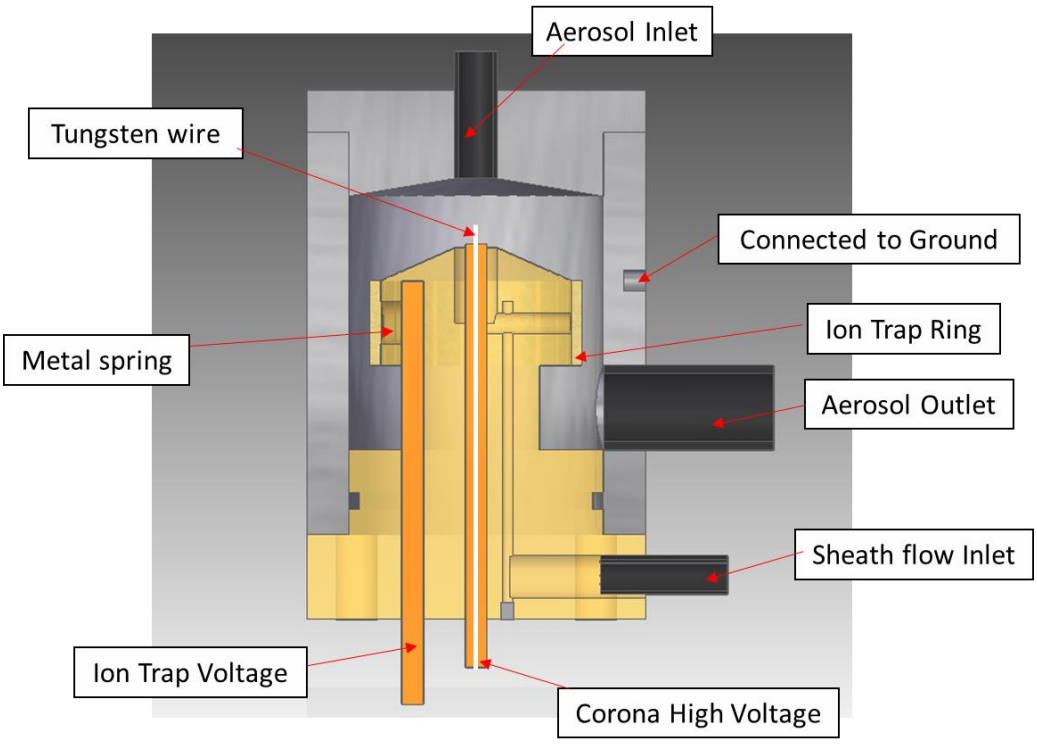

Figure 4 - 1 Schematic diagram of the prototype charger

The average charge per particle of the existing unipolar charger are relatively low: the charge per particle is proportional to $d_p^{0.91} - d_p^{1.28}$, which might not be appropriate to use in this application. In order to achieve high index value, the charger design is based on the direct-type charging method, which the corona is directly exposed to the particles. Figure 4-1 showed the schematic diagram of the charger used in the new electrical PM sensor. The overall size of this charger is comparable to a US quarter coin. A tungsten wire (50 μm in diameter), inserted through a metal rod, is used to create corona. Particles entering from the inlet can pass the corona zone and get charged. A contraction region between the ion trap ring and wall is for removing the excess ions. After passing the contraction region, the charged particles are exited at one side of the charger. During the operation, a gentle sheath flow is used to protect the tip from particle contamination, and the wall of the charger is connected to the ground.

4.2.3 Precipitator design

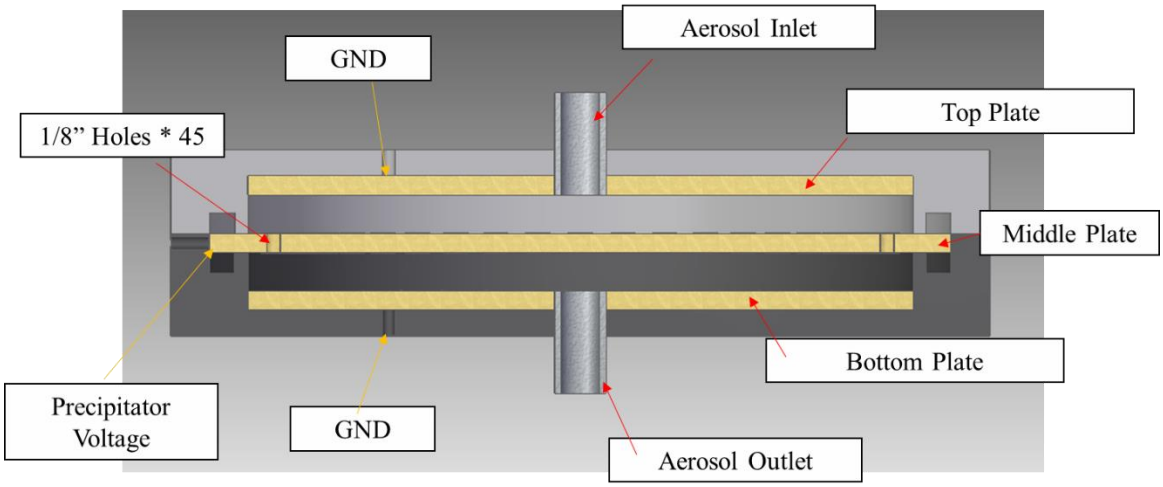

Figure 4 - 2 Schematic diagram of the electrostatic precipitator

The design of the electrostatic aerosol precipitator is a disk-type precipitator, which is like Qi's mini-disk electrostatic aerosol precipitator (2008) but a scaled-up version. It contains three metal plates (i.e., top plate, middle plate and bottom plate.), in which the middle plate was sandwiched between the top and metal plate symmetrically. Forty-five 1/8" diameter holes are in an annulus closed to the outer edge of the middle disk. The particles exiting from the top space can be re-mixed and entered the bottom space by passing through these small holes. Two central tubes connected to the top and bottom plate are aerosol flow inlet and exit, respectively. During evaluation or operation, voltage is applied to the middle plate though high voltage cable, while the top and bottom plates are electrically grounded or connected to the electrometer. The disk design of the precipitator leaves users an option to use it as single-stage precipitator or dual-stage precipitator. The usage of the dual-stage precipitator can ease the high index value requirement on charger performance, which might be favor in total volume measurement.

4.3 Experimental setup

4.3.1 Charger evaluation

Two parameters of the prototype charger were characterized experimentally: (i) the charging efficiency (i.e., both intrinsic and extrinsic charging efficiency), and (ii) the average charge per particle. The experimental setup is shown in Fig 4-3. Polydisperse particles were generated by either the evaporation-condensation technique (i.e., furnace; for particle mean diameter smaller than 40 nm) or the custom-made Collison atomizer (for particle mean diameter larger than 40 nm). These polydisperse particles were then classified by a Nano-Differential Mobility Analyzer (Nano-DMA, TSI Model 3085) to obtain monodisperse particles of diameter less than 40 nm, or by a long DMA (TSI model 3081) to obtain monodisperse particle of diameters in the range of 40 – 500 nm. These charged monodisperse particles were neutralized by the Po^{210} and the rest charged particles were removed by following charged particle remover (i.e., 1st Precipitator), to obtain neutral test monodisperse particles.

For charging efficiencies measurement, including intrinsic and extrinsic charging efficiency, particle concentration was measured by condensation particle counter (CPC, TSI Model 3775). Intrinsic charging efficiency was used to characterize the fraction of particles being charged. It was measured using the method of Romay and Pui (1992), and defined as:

$$\eta_{in} = 1 - \frac{N_1}{N_2} \tag{4-5}$$

Where η_{in} is the intrinsic charging efficiency; N_1 and N_2 are the particle number concentration both measured downstream of the 2nd precipitator, while N_1 is measured with

both charger and 2nd precipitator on, and N_2 is measured similarly to N_1 but with both charger and 2nd precipitator off.

The extrinsic charging efficiency was measured by the method of Chen and Pui (1999), which taken the particle loss during charging and transportation processes into account. The extrinsic charging efficiency are described as following equation:

$$\eta_{ex} = \frac{N_3 - N_1/P_{cpr}}{N_4} \tag{4-6}$$

Where η_{ex} is the extrinsic charging efficiency; N_3 is the particle number concentration exiting the charger (i.e., without passing through the 2nd precipitator); N_4 is the particle number concentration measured before entering the charger; and, P_{cpr} is the penetration of neutral particles in the 2nd precipitator.

At the meantime of measuring N_3, an aerosol electrometer (TSI Model 3068B) was also used to measure the induced current carried by the charged particles, which can be used to derive the average charge per particle:

$$n_{ave} = \frac{I}{(N_3 - N_1/P_{cpr}) * e * Q_e} \tag{4-7}$$

Where I is the measured current by the aerosol electrometer; e is the elementary charge, $1.6 * 10^{-19}$ C; Q_c is the flowrate of the aerosol electrometer.

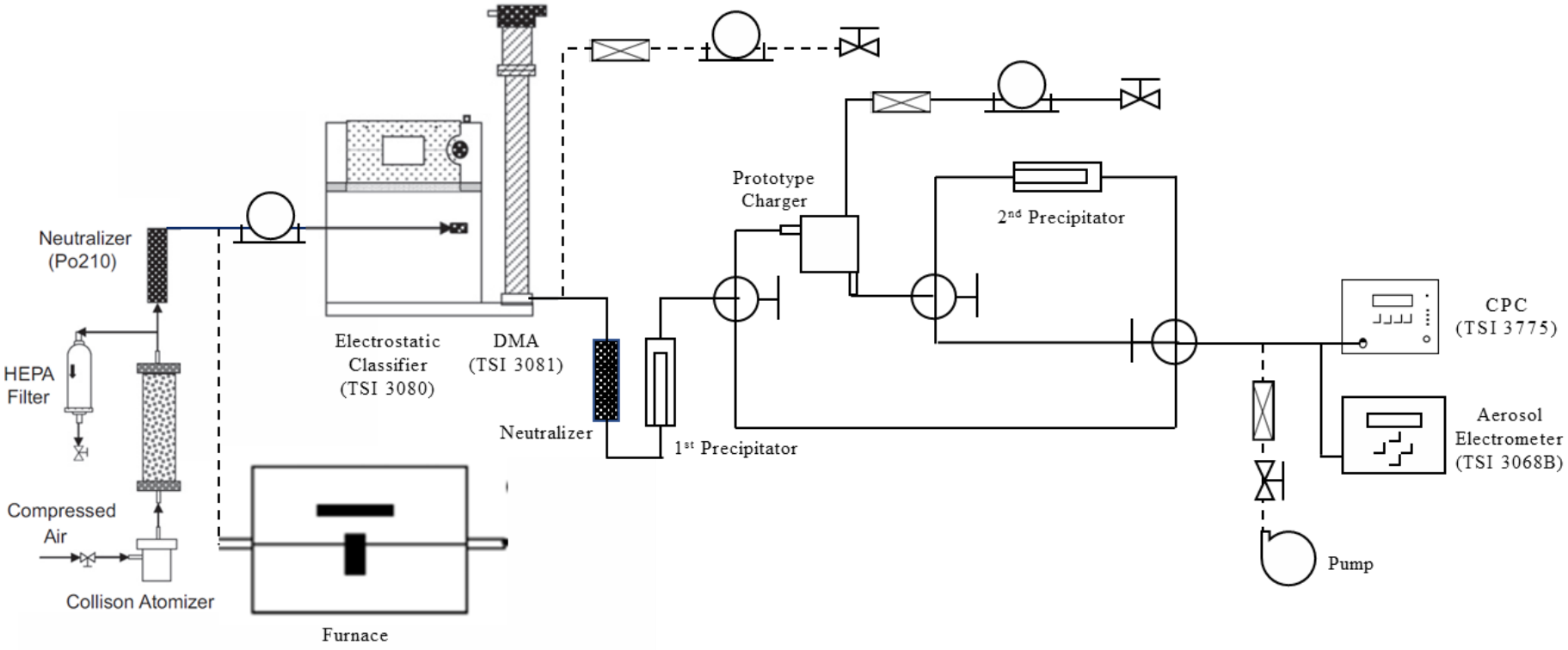

Figure 4 - 3 Experimental Setup of the prototype charger evaluation

4.3.2 Precipitator evaluation

The schematic diagram of the experimental setup for the evaluation of the disk precipitator is shown in Figure 4-4. The polydisperse NaCl particles were generated by either the evaporation-condensation technique (i.e., furnace) or the custom-made Collison atomizer. Monodisperse particles, ranged from 15-500 nm, were obtained by the classification from a Nano-Differential Mobility Analyzer (Nano-DMA, TSI Model 3085) or a long DMA (TSI model 3081). The transmission efficiencies of both singly charged and neutral monodisperse particles were evaluated for all particle sizes when all plates are electrically grounded. The penetration curve of singly charged monodisperse particles was obtained by using CPC (TSI Model 3775) to monitor the particle concentration in the downstream of the precipitator. During the measurement, a voltage was applied on the middle plate while the top and bottom plate kept electrically grounded. For each test particle size, the particle penetration P is defined as following equation:

$$P = \frac{N(V)}{N(0)} \tag{4-8}$$

Where $N(0)$ is the particle concentration with zero voltage applied on the middle plate; $N(V)$ is the particle concentration measured in the downstream, corresponding to an applied voltage V. The $N(0)$ was measured before and after each test particle size to make sure the stability of the particle concentration in the upstream.

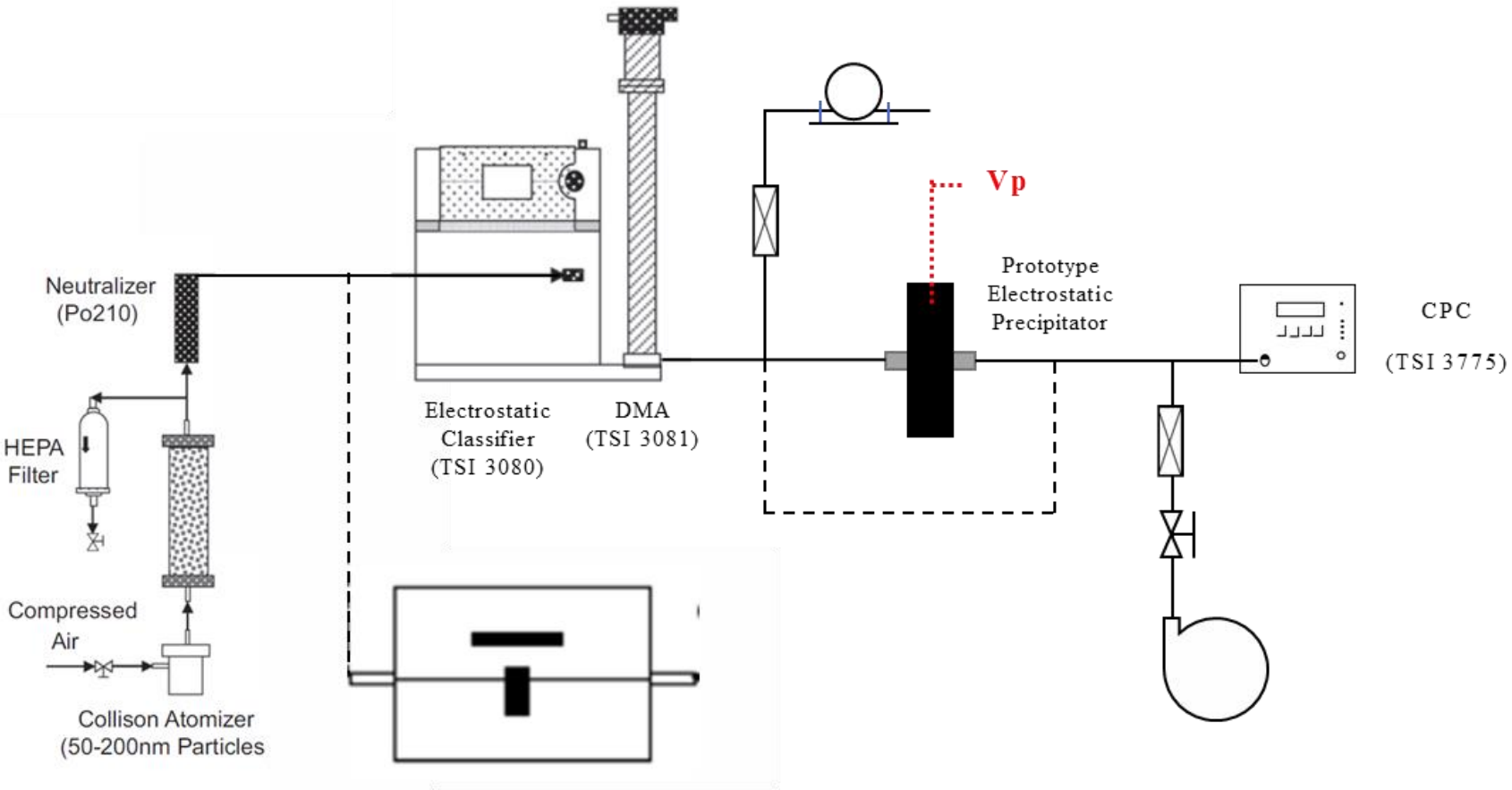

Figure 4 - 4 Experimental Setup of the prototype electrostatic precipitator evaluation.

4.3.3 Overall sensor evaluation

By assembling the charger and precipitator together, the overall performance of the new electrical PM sensor (eM sensor) was challenged by different polydisperse particle groups. The electrical PM sensor was evaluated as both total surface area and volume monitor. The experimental setups for the two cases were very similar. Figure 4-5 shows the schematic diagram of the experimental setup. Polydisperse particles with different mean particle sizes (ranged from 50 to 120 nm), standard deviation values (ranged from 1.6 to 2.0) and materials were generated by either a custom-made Colison atomizer or Hudson nebulizer. These particles were dried by a diffusion dryer and diluted by an aerosol diluter (Liu, 2014). Before being detected, these polydisperse particles were also neutralized by a Po^{210} radiation source, and the rest of the charged particles were removed by the following charged particle remover. In each testing case, the concentration of the polydisperse particles was varied by the aerosol diluter.

The neutral polydisperse particles stream was then split into two: one stream was introduced to the eM sensor, while the other stream was introduced to an SMPS (TSI Model 3936). The aerosol to sheath flow ratio of the SMPS was set to 1:3 (i.e., 1.5 lpm for aerosol flowrate and 4.5 lpm for sheath flowrate), which can cover most of the particle size range. As reference, the data recorded by SMPS for each sample can be used to deduce the total surface area or total volume values. In the eM sensor stream, test particles were passed though the charger and precipitator in sequence. The working flowrates of the charger and precipitator were designed according to the calibration results from the charger and precipitator experiment previously mentioned: the flowrate of the precipitator was kept at 2.0 lpm for both as total surface area monitor or total mass monitor; while the charger

flowrate was 2.0 lpm for total surface area monitor and 9.0 lpm for mass monitor. When the eM sensor was used as mass monitor, a flow split was applied for the test particles after the charger. This was because the desire working flowrate of the charger and precipitator were not matching. However, when the eM sensor was used as surface monitor, all flow was entered the precipitator after exiting from the charger. A voltage was applied on the middle plate of the precipitator, in which charged particles were deposited on either top or bottom plated according to their electrical mobility. Two electrometers were electrically connected to the precipitator top and bottom plate, respectively. The measured signal from the two electrometers can be referred to the total surface area or volume.

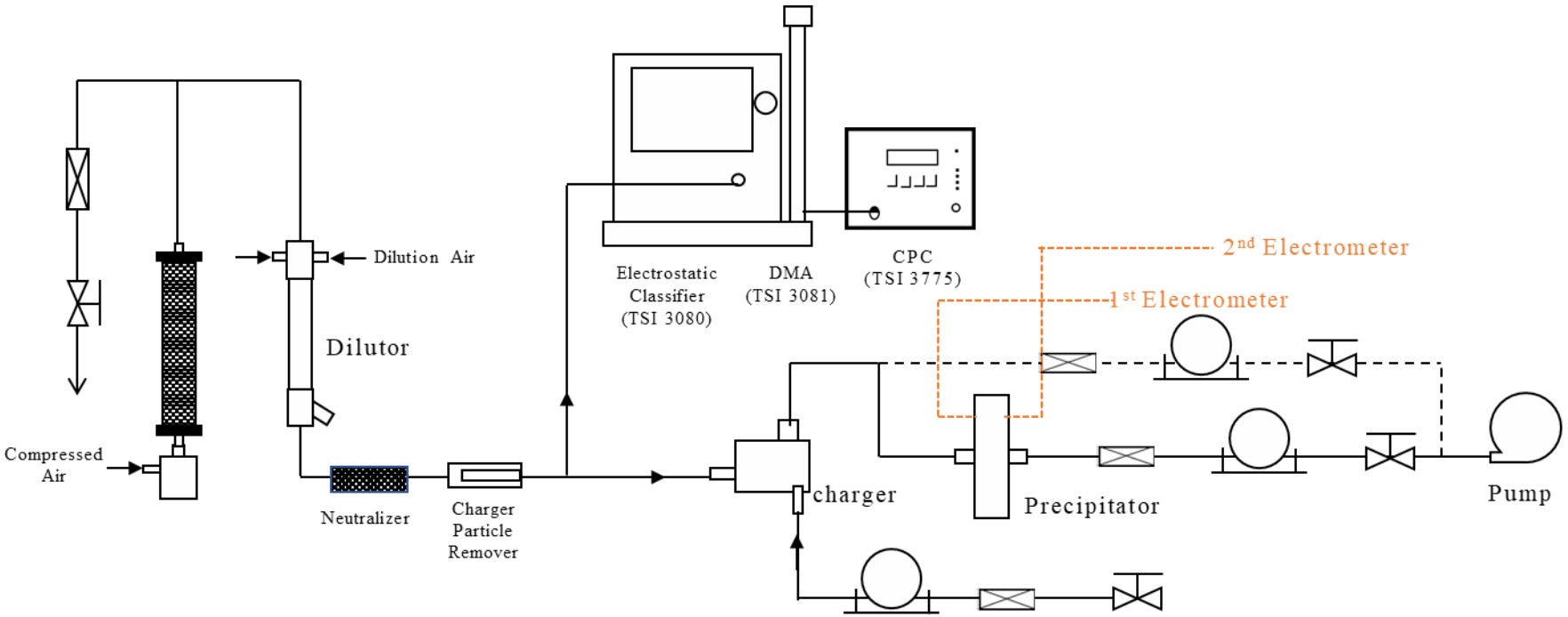

Figure 4 - 5 Experimental Setup of the assembled PM sensor evaluation

4.4 Results and discussion

4.4.1 Surface area monitor

(1) Charger performance

Both the charging efficiency and average charge performance of the prototype charger were experimentally evaluated for different particle size. The working flowrate of the charger were chosen at 1.0, 1.5 and 2.0 lpm, and the corona current of the charger was fixed at 1.0 μA. Figure 4-6 shows the intrinsic charging efficiency of the charger under different flowrate. The intrinsic charging efficiency increased as particle size increased and reached 100% for particles with diameters larger than 45nm, which represented the all particles with diameters larger than 45 nm were charged. This highly charged performance is due to the design of the charger, which particles were passed through the corona zone. It was also found that the intrinsic charger efficiency was higher in lower flowrate (i.e., 1.0 lpm). This is because that lower operational flowrate results in longer residence time in the corona zone, which enabled more ions to be attached on a particle.

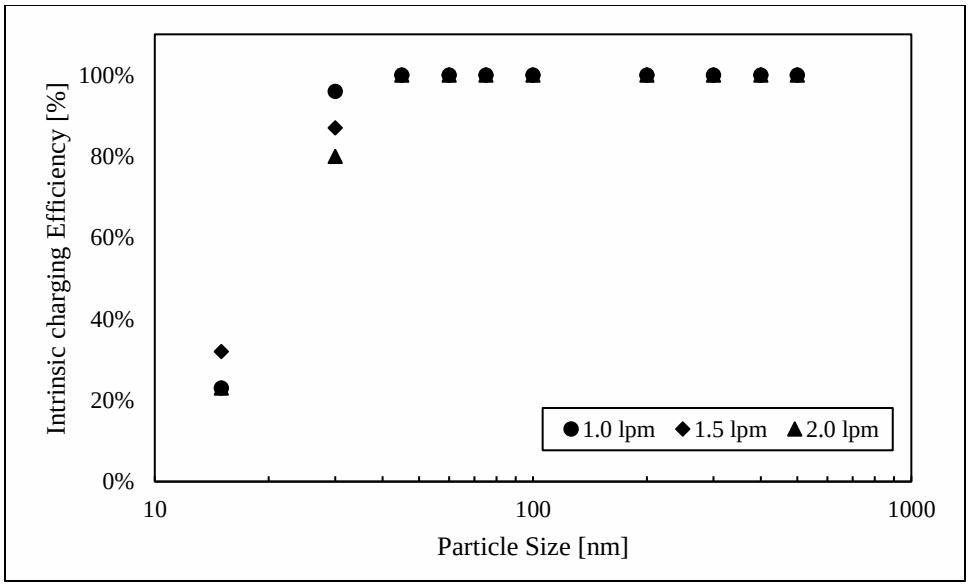

Figure 4 - 6 Intrinsic charging efficiency of the prototype charger under different flowrate.

Figure 4-7 shows the extrinsic charging efficiency for different particle size at 1.0, 1.5 and 2.0 lpm aerosol flowrate. The trend of the curves was similar under the each aerosol flowrate: the extrinsic charging efficiency increased as particle size increased for the particles with diameter smaller than 100nm. For particles larger than 100 nm, the rising trend was eased. The extrinsic charging efficiency was stayed around 42%, 51% and 58% for 1.0, 1.5 and 2.0 lpm, respectively. However, obvious differences were found among the three aerosol flowrates. Larger extrinsic charging efficiency was achieved at higher aerosol flowrate. The reason for this is that higher aerosol flowrate results in shorter particle residence time and thus leads to less charged particle loss.

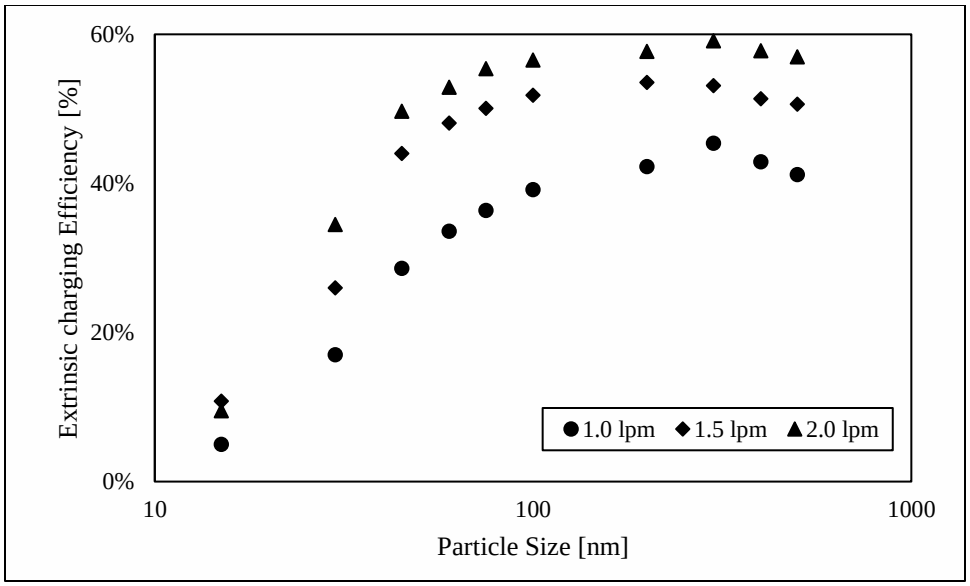

Figure 4 - 7 Extrinsic charging efficiency of the prototype charger under different flowrate.

Figure 4-8 shows the number of average charge on particles as a function of particle size under 1.0, 1.5 and 2.0 lpm. The number of average charge grew in power function of particle size. The exponents of the power function were 1.3433, 1.4101 and 1.4076 for 1.0, 1.5 and 2.0 lpm, respectively. Figure 4-9 replots figure 4-8, by changing the y-axis into the multiplication of the mean charge per particle and the extrinsic charging efficiency. These values were still increased exponentially along with the increase of particle size. The exponents of the power function were 1.5864, 1.6015 and 1.6588 for 1.0, 1.5 and 2.0 lpm, respectively. According to Figure 4-8 and Figure 4-9, even the exponents were not the same, there were no obvious differences in the absolute values of mean charge per particle for these three aerosol flowrates. For the sake of reducing the particle loss, the aerosol flowrate was better chosen at 2.0 lpm, in which the extrinsic charging efficiency was the highest.

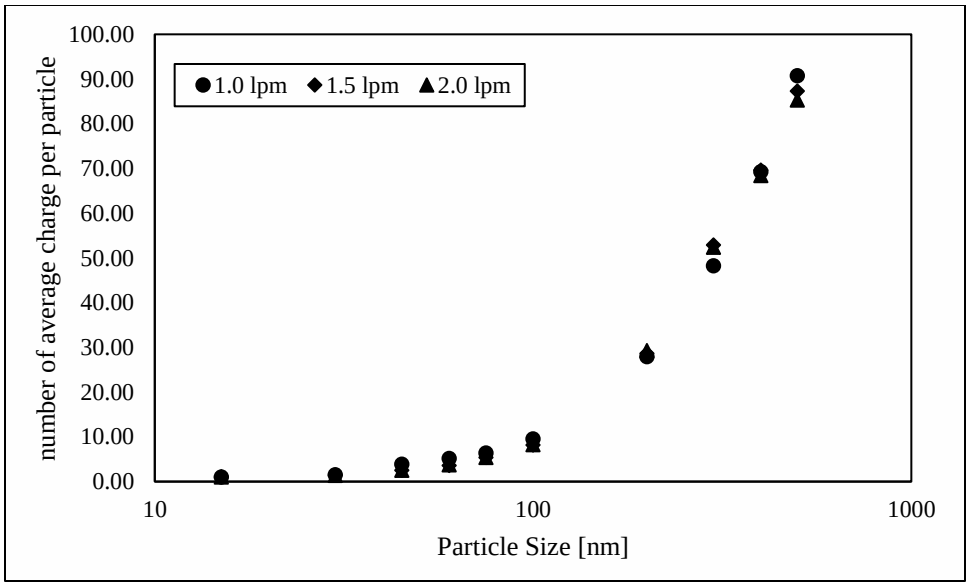

Figure 4 - 8 Mean charge per particle for monodisperse particle under different flowrate.

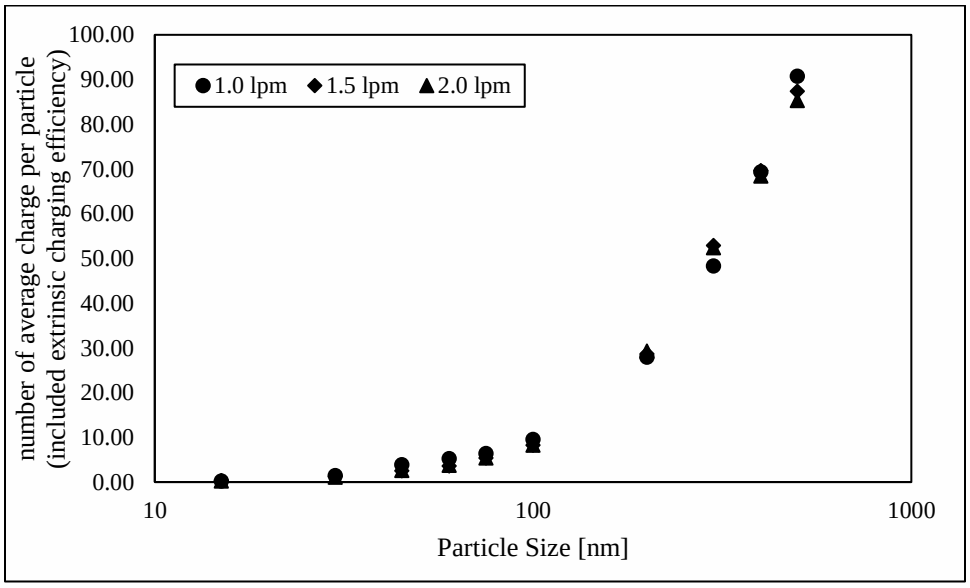

Figure 4 - 9 Mean charge per particle (considering the extrinsic charging efficiency) for monodisperse particle under different flowrate.

(2) Precipitator performance

The prototype precipitator was evaluated under the following condition: both top and bottom plate were grounded, and a high voltage was applied at the middle plate. The particle penetration curve was obtained by taking the ratio of the concentration in the upstream to the downstream. Figure 4-10 shows the particle penetration curve for different

particle size under four different sampling flowrates (i.e., 1.0, 2.0, 3.0 and 5.0 lpm). Monodisperse particles, ranged from 15 to 500 nm, were used for the evaluation. The particle penetration curves appeared slightly nonlinear, which was because of the remixing and redistribution of the particle concentration after passes through the small holes in the middle plate and enters the bottom chamber. Qi developed a model to derive the transfer function for the disk-type electrostatic precipitator (2008). According to the remixing assumption, the penetration of charged particle through the precipitator was showed as the following equations:

$$\mathrm{P}_p = (1 - KV)^2 \tag{4-9}$$

$$\mathrm{K} = \frac{\pi r_0^2}{2bQ\alpha} * Z_p \tag{4-10}$$

Where K is the characteristic slope of particle precipitation for the curve, related to the dimension and operation parameter of the precipitator; V is the applied voltage; r_0 is distance between the center of middle plate to one small hole; 2b is the height of either the top or bottom chamber. α is an empirical coefficient.

The penetration of single chamber can be obtained by taking the square root of eq.(4-9) on both sides:

$$P_p^{0.5} = 1 - \mathrm{KV} \tag{4-11}$$

Figure 4-11 shows the square root of the experimental particle penetration, $P_p^{1/2}$, as a function of normalized voltage (V/V_{50}). V_{50} is defined as the applied voltage at 50% particle penetration. The linear relationship is demonstrated in the figure, especially for the

sampling flowrate of 2.0 and 3.0 lpm. Besides, under these two flowrates (i.e., 2.0 and 3.0 lpm), the normalized penetration curves were merged well with each other, which further prove the size-independent performance for this precipitator. It is better to operate this precipitator under these two flowrates.

Further calculation was also carried out based on the model developed by Qi, to define the empirical coefficient α for both 2.0 and 3.0 lpm sampling flowrate. Figure 4-12 shows the comparison of experimental and modeled K values for the two different flowrates, as the function of particle electrical mobility. The proposed model shows a good agreement with the experimental data, and the empirical factor α is set at 0.873 and 1.06 for 2.0 and 3.0 lpm, respectively.

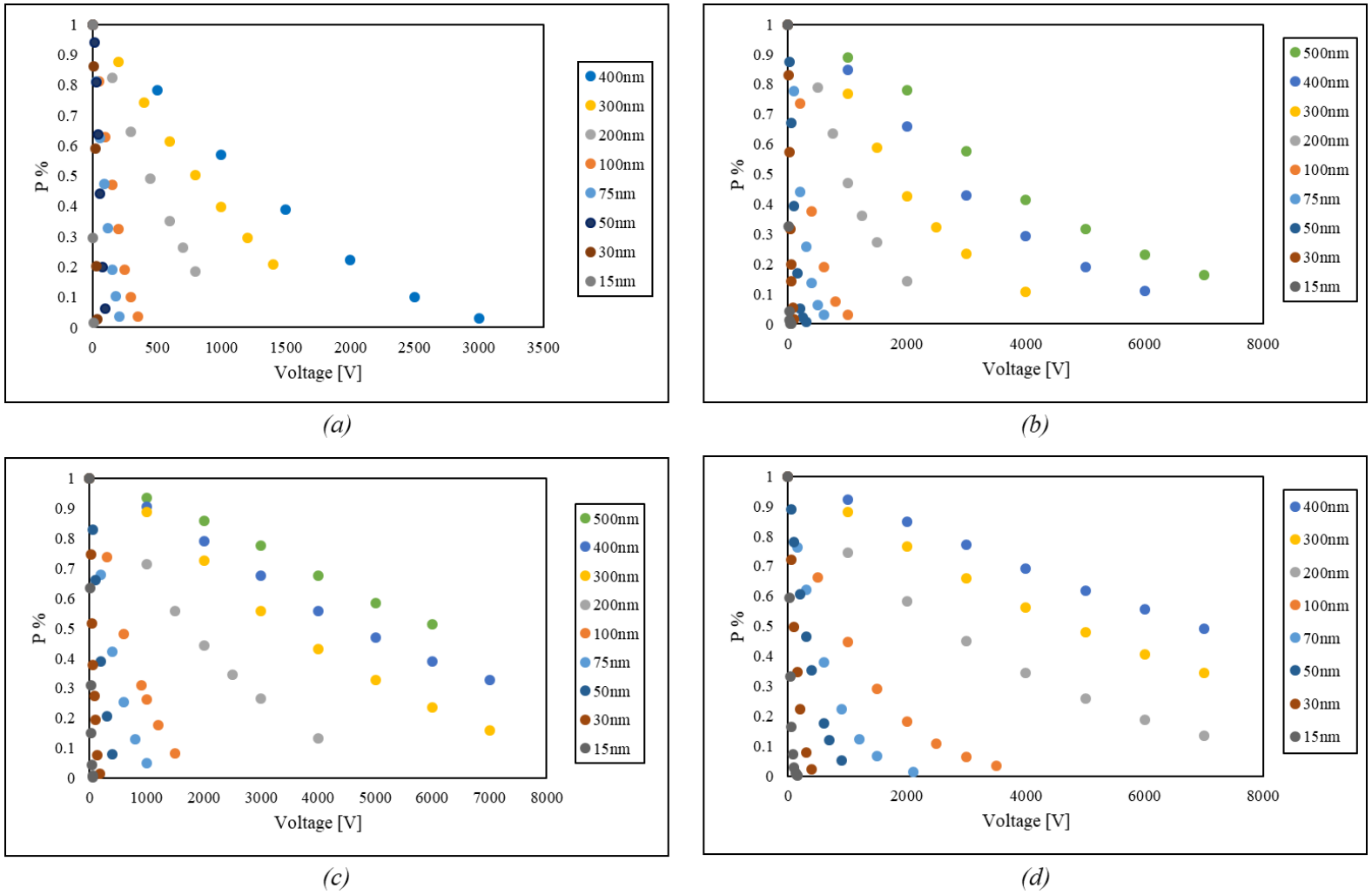

Figure 4 - 10 Particle Penetration curves of the disk-type aerosol precipitator under different sampling flowrates. (a)1.0 lpm; (b) 2.0 lpm; (c) 3.0 lpm; (d) 5.0 lpm.

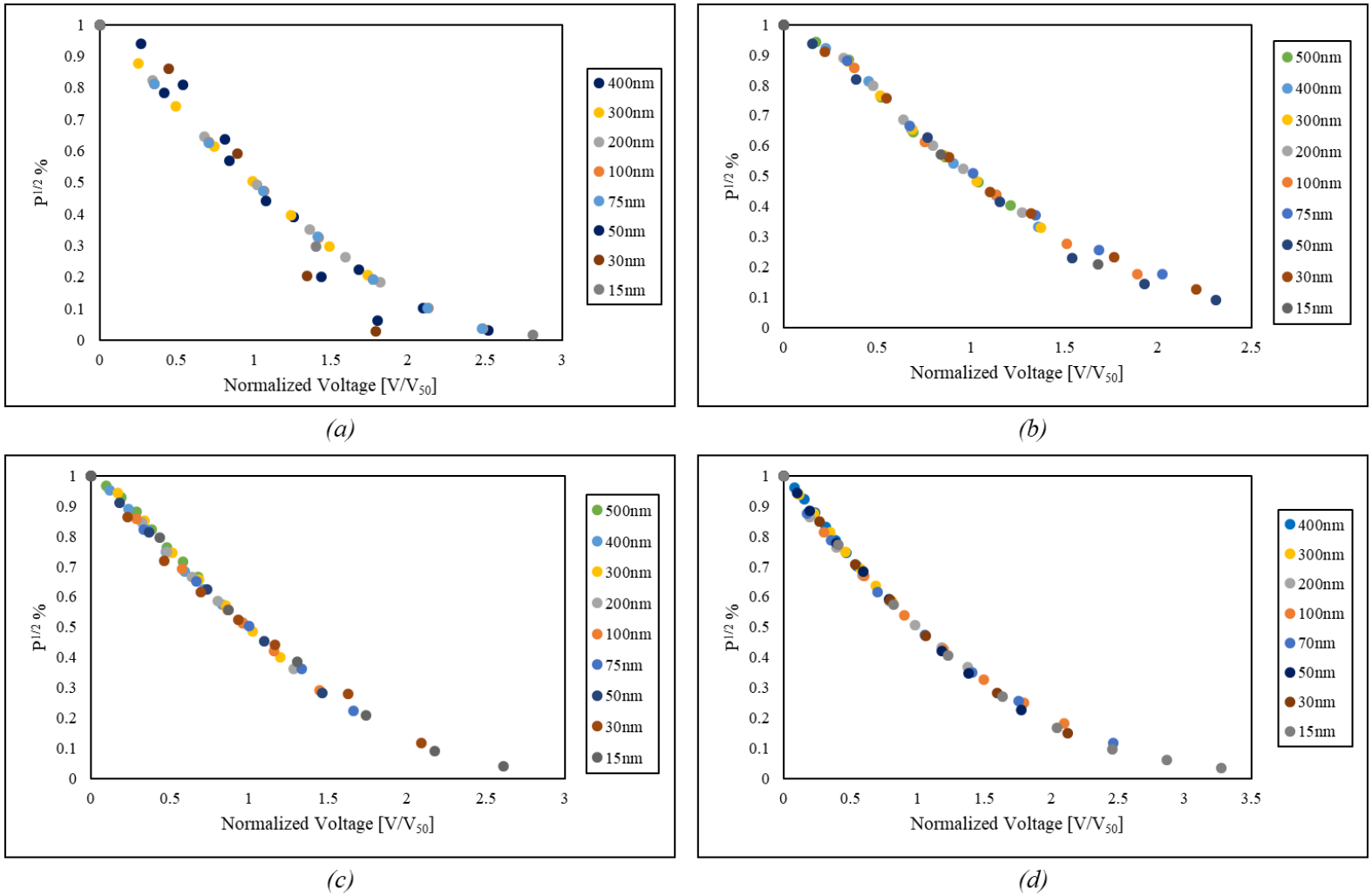

Figure 4 - 11 $P^{1/2}$ of the disk-type aerosol precipitator under different sampling flowrates. (a)1.0 lpm; (b) 2.0 lpm; (c) 3.0 lpm; (d) 5.0 lpm

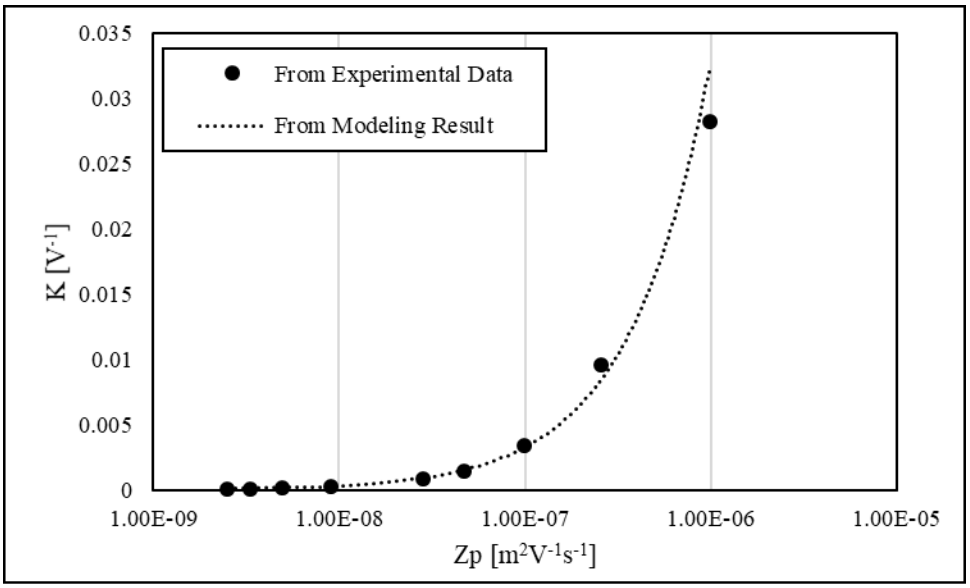

(a)

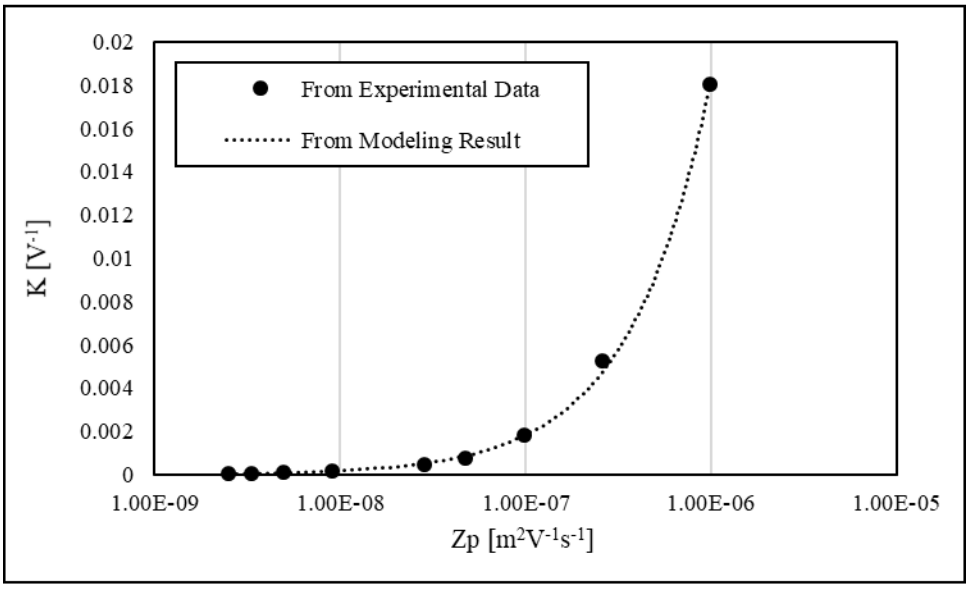

(b)

Figure 4 - 12 Fitting the model of K with experimental data. (a)2.0 lpm; (b) 3.0 lpm.

(3) Overall performance

By assembling the charger, precipitator and the current monitor (i.e., electrometer) together, the overall performance of the sensor can be evaluated. The charger current was set at 1.0 μA, and the operational flowrate of the charger and precipitator was 2.0 lpm. An electrometer was used to measure the current induced by the particles deposit on the precipitator top plate. In section 4.2.1, the equation of the measured signal has been derived as:

$$\mathrm{I} = \mathrm{e} * \mathrm{Q} * \sum_{i=1}^{n} N_i(dp) * n_{ave}(dp) * \eta_{ex}(dp) * P(dp) \quad (4\text{-}1)$$

The expression for P is shown as:

$$P = 1 - P_p^{0.5} = \mathrm{KV} \quad (4\text{-}12)$$

$$\mathrm{K} = \frac{\pi r_0^2}{2bQ\alpha} * Z_p \quad (4\text{-}10)$$

$$Z_p = \frac{n_{ave} e C_s}{3\pi\mu D_p} \quad (4\text{-}13)$$

Where μ is the viscosity of the gas; C_s is the Cunningham slip correction factor.

According to eq.(4-12), eq.(4-10) and eq.(4-13), the linear relationship between P and Z_p can be derived. For the particle size range concerned in the total surface area, the contribution of slip correction factor C_s to the exponent of D_p can be assumed as minor. Since n_{ave} was proportional to $D_p^{1.4076}$, P was linearly related to $D_p^{0.4076}$ according to a

rough calculation. In addition, the multiplication of n_{ave} and η_{ex} was proportional to $D_p^{1.6588}$. Therefore, eq.(4-1) can be rewriten as:

$$I = \mathrm{e} * \mathrm{Q} * \sum_{i=1}^{n} N_i(dp) * k * D_p^{1.6588+0.4076} \approx \mathrm{e} * \mathrm{Q} * \sum_{i=1}^{n} N_i(dp) * k * D_p^2$$

According to the equation showed above, the measured signal of the assembled device should show a good linear relationship to the total surface area concentration. To prove the hypothesis, experiment was carried out to challenge the sensor under test particles with different mean particle sizes, standard deviation values and materials.

Solid particle test. Figure 4-13 shows the evaluation of the electrical PM sensor under the challenge of solid particle groups. For the mean particle size test (fig 4-13a), the number-based mean particle sizes, D_p, of test particles generated from atomizing sodium chloride solutions with different concentration, was 55, 65 and 85 nm, respectively. It was found that all the curves merged together and showed a linear relationship to the total surface area concentration. Similar results were also found in the test particles with different geometric standard deviation values (figure 4-13b): the curves from two particle groups, generated by two different aerosol atomizers (i.e., the Hudson nebulizer and Colison atomizer), were also showed no difference. The polydisperse particles generated by the Hudson nebulizer has a larger standard deviation value (around 2.2), while the Colison atomizer produced particles with a smaller standard deviation value (around 1.8). Particles with different materials were also tested for the device. Figure 4-13c shows the experimental curves of NaCl and sucrose particle, of which the dielectric constant values were 6.1 and 3.3, respectively. Likewise, no obvious differences were found for these two curves. In sum, the assembled monitor showed a single linear curve when challenged by

solid particles with different properties. This proves the result that the measured signals of the monitor were truly proportional to D_p^2.

Liquid particle test. Similar to figure 4-13, figure 4-14 shows the evaluation of electrical PM sensor under the challenge of liquid particles. The test particles with different mean particle sizes were generated by dissolving DEHS into ethanol at different concentration. The mean particle size for the three liquid particle groups were 75, 110 and 140 nm, respectively. The particles with different standard deviation values were obtained by using Hudson nebulizer and Colison atomizer. Additionally, the performance curves from DEHS and Oleic Oil particles were also included (dialectical constant: DEHS 5.1 and Oleic Oil 2.4-2.5). Negligible difference can be found in all the three cases. This further represents that the variation of mean particle size, standard deviation value and material has minor effects on the performance of the electrical PM monitor.

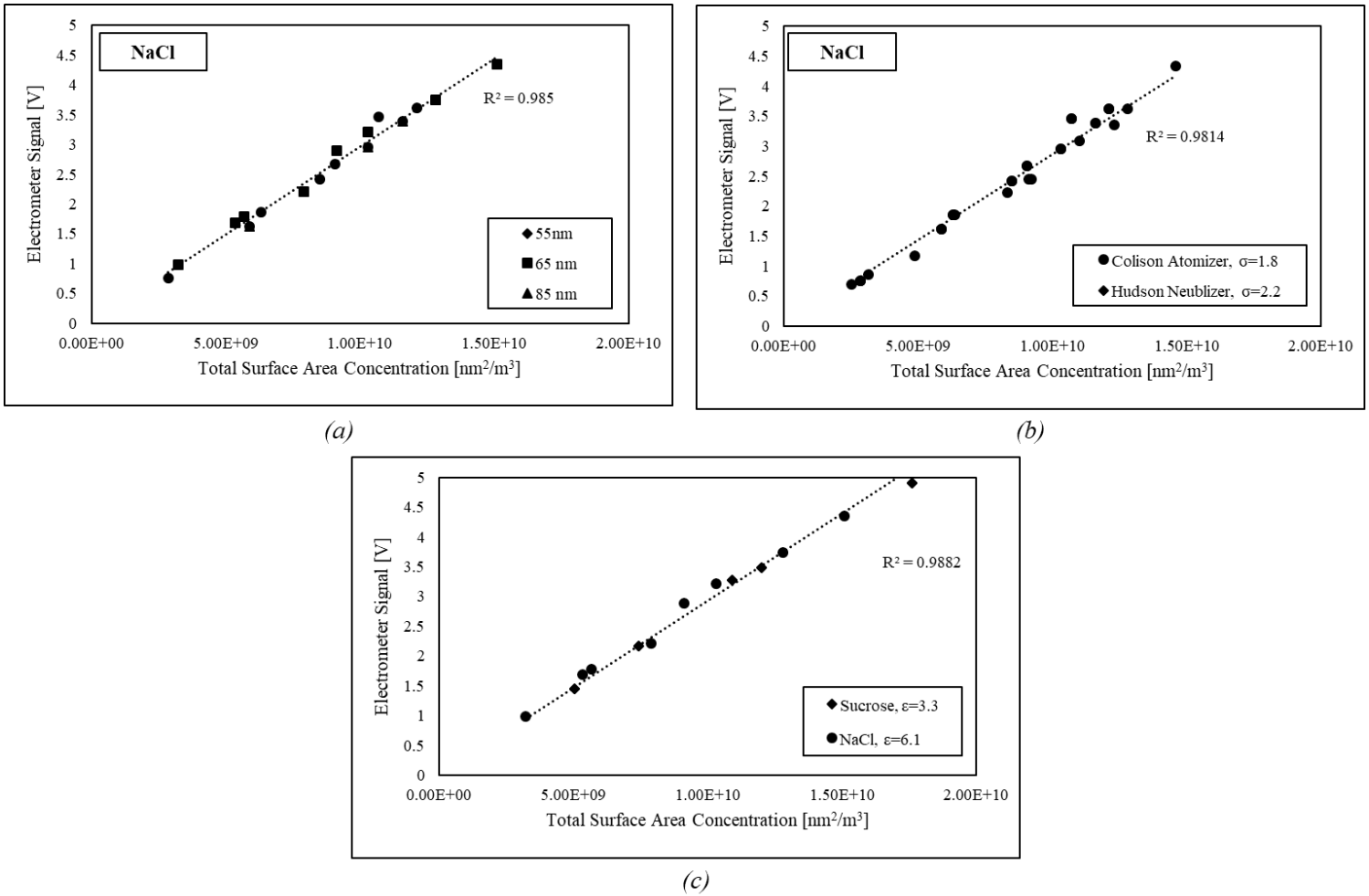

Figure 4 - 13 PM sensor correlation curves between the measured signal to the total surface concentration of solid particles with different (a)mean particle size; (b) standard deviation value; (c) material.

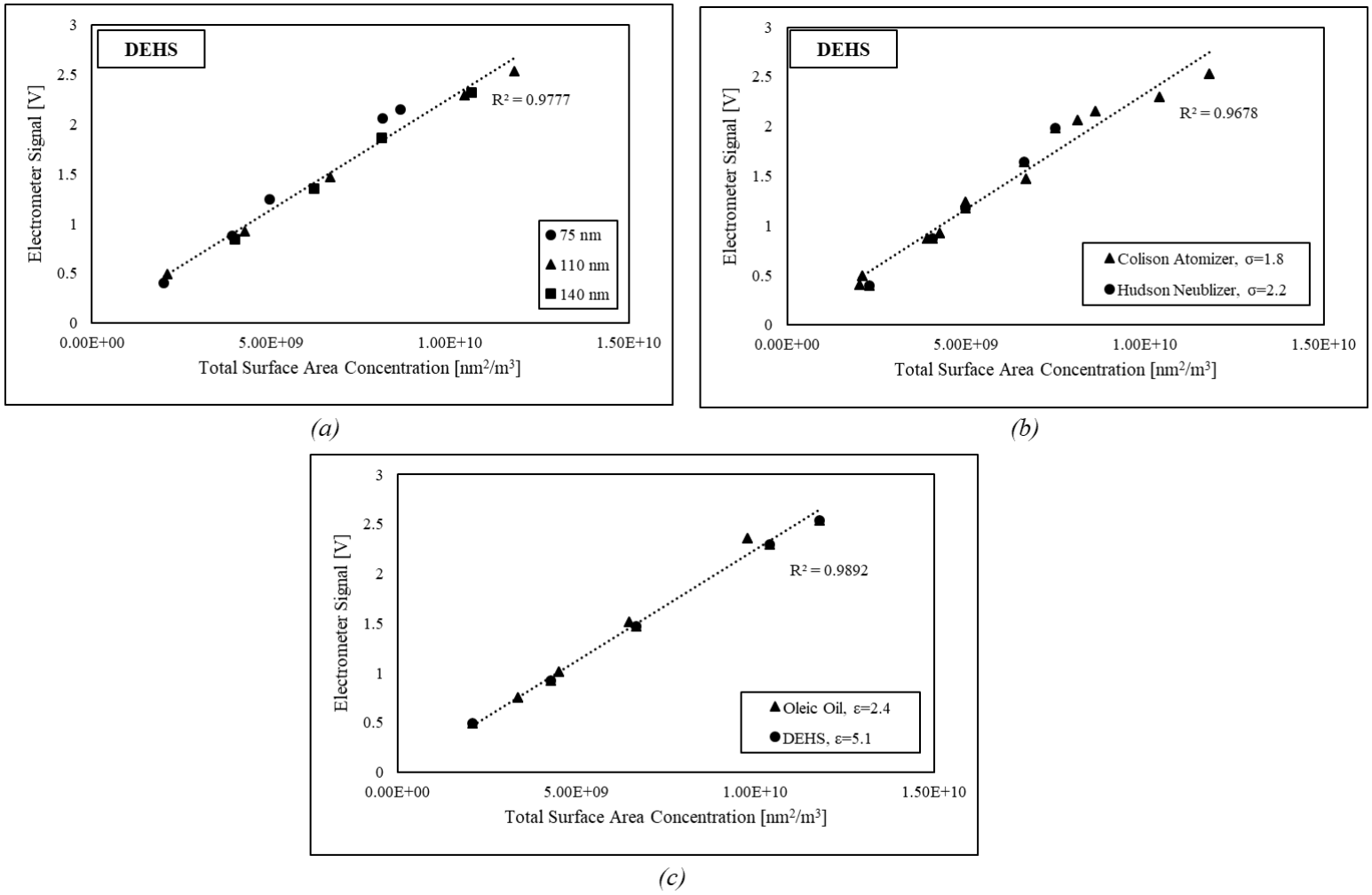

Figure 4 - 14 PM sensor correlation curves between the measured signal to the total surface concentration of liquid particles with different (a)mean particle size; (b) standard deviation value; (c) material.

4.4.2 Mass monitor

Except for being used as a total surface concentration monitor, the prototype was also studied as a mass concentration monitor. Thus, the measured signal I (from eq.(4-1)) was expected to be proportional to D_p^3. In order to achieve the exponent as three, the charger current and flowrate were increased. Besides, the signal was measured from both top and bottom plates of the precipitator.

Figure 4-15 shows the charger intrinsic and extrinsic charging efficiency performance under increased flowrates (i.e., 3.0, 6.0 and 9.0 lpm) and currents (i.e., 2.0 μA and 4.0 μA). The intrinsic charging efficiency increased as particle size increased and reached 100% for particles with diameters larger than 75nm. This indicated the all particles with diameters larger than 75 nm were charged. It was found that the intrinsic charging efficiency was higher in lower flowrate (i.e., 3.0 lpm), which had longer residence time for particles to get charged. At a fixed sampling flowrate, it was also found that the intrinsic charging efficiency was higher in higher charger current (i.e., 4.0 μA). This is because higher charger current results in stronger corona, which also lead to higher charging fraction. In the figure 4-15b, the extrinsic charging efficiency for 6.0 and 9.0 lpm cases were similar to each other, while the 3.0 lpm case was obviously lower. This is because that lower aerosol flowrate results in longer particle residence time and thus leads to more charged particle loss.

Figure 4-16 shows the mean charge per particle performance of the charger under different test conditions. The number of average charge grew in power function of particle size. In a fixed charger current, larger number of charge per particle can be found in a lower sampling flowrate. It is due to the longer residence time in low flowrate, which allow more

ions to be attached on a particle. It was also found that the mean charge per particle was higher in larger charger current. Even though observable difference can be found in the mean charge per particle among these cases, the exponent in the power function of these curve are closed. The exponents were 1.6243, 1.6023 and 1.6040 for 3.0, 6.0 and 9.0 lpm on charger current of 2.0 μA, respectively, and 1.6202 for 9.0 lpm on charger current of 4.0 μA. For the sake of saving energy (i.e., lower electricity usage) and reducing particle loss, the charger was set to operate at 9.0 lpm with 2.0 μA charger current. Thus, the multiplication of mean charge per particle and extrinsic charging efficiency is power function to particle size with exponent of 1.6579.

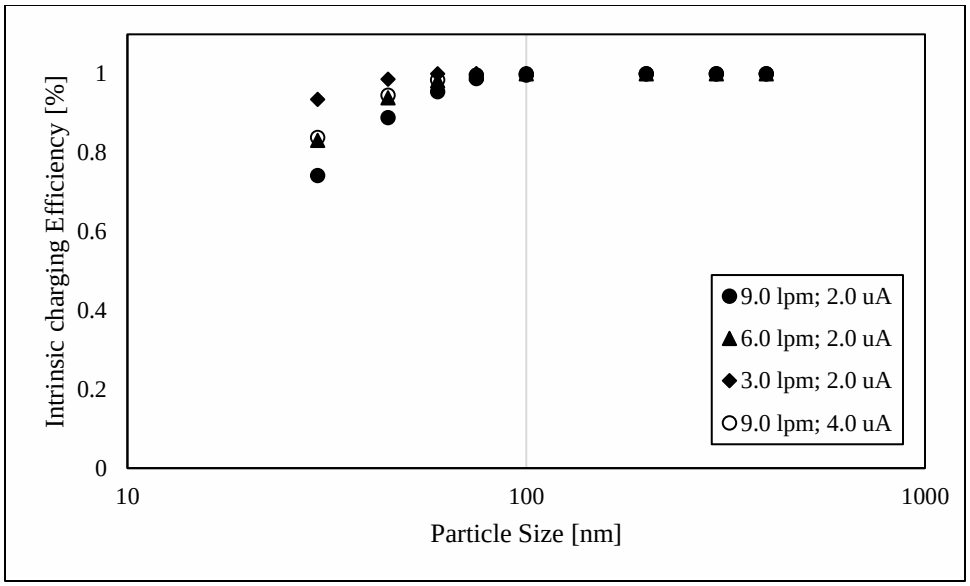

(a)

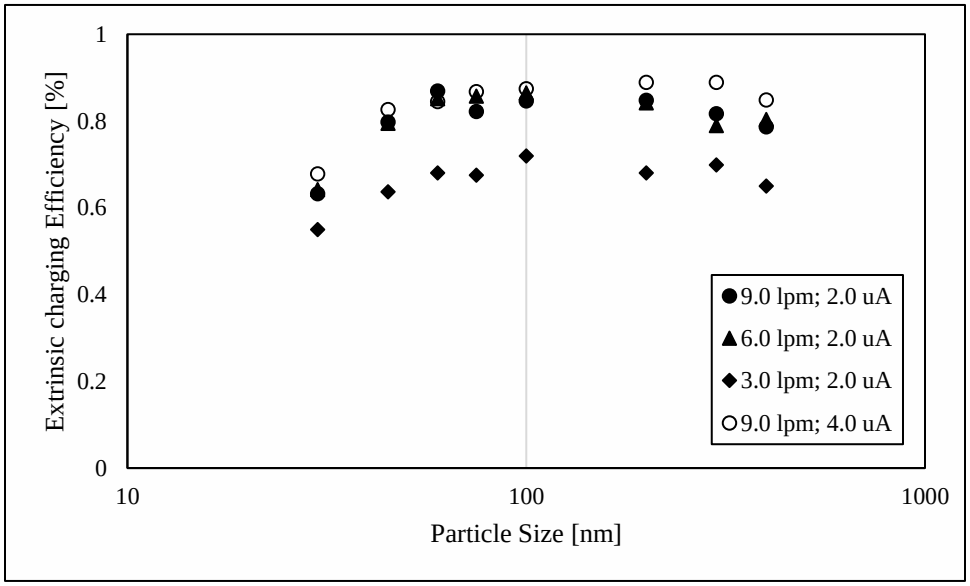

(b)

Figure 4 - 15 Charging efficiency of the prototype charger for mass monitor. (a) Intrinsic charging efficiency; (b) extrinsic charging efficiency.

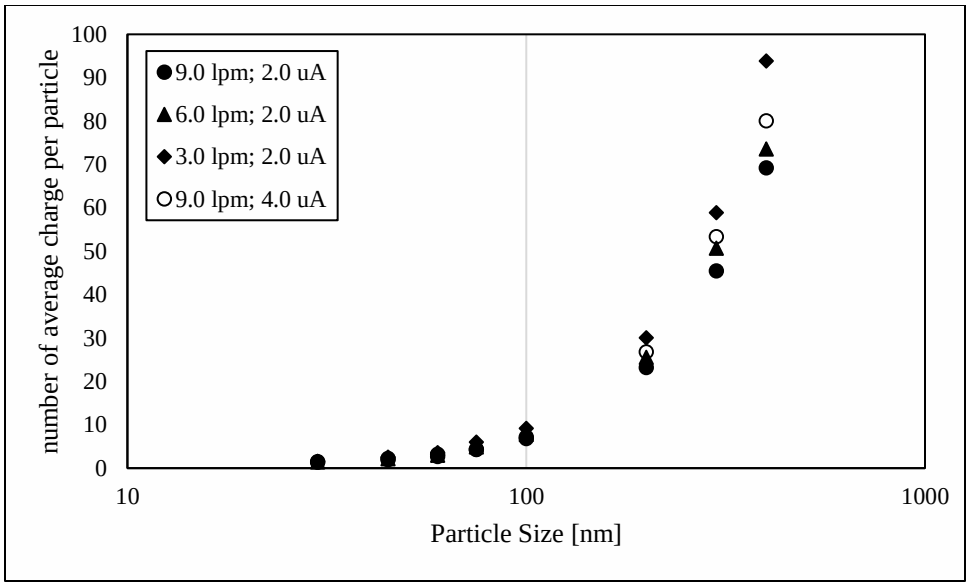

Figure 4 - 16 Mean charge per particle of the prototype charger for mass monitor.

The precipitator was kept operating at 2.0 lpm, in order to maintain the linear transfer function performance. Thus, a flow split was used after the stream exiting from the charger and before entering the precipitator. As mentioned, there were two measured signals in the mass monitor cases: one from the top plate and the other from the bottom plate. The measured signal from the top and bottom plate can be expressed as following eq.(4-14) and eq.(4-15), respectively:

$$\mathrm{I}_{top} = \mathrm{e} * \mathrm{Q} * \sum_{i=1}^{n} N_i(dp) * n_{ave}(dp) * \eta_{ex}(dp) * \mathrm{KV} \tag{4-14}$$

$$\mathrm{I}_{bottom} = \mathrm{e} * \mathrm{Q} * \sum_{i=1}^{n} N_i(dp) * n_{ave}(dp) * \eta_{ex}(dp) * (1 - \mathrm{KV}) * \mathrm{KV} \tag{4-15}$$

The difference between I_{top} and I_{bottom} is shown as:

$$\mathrm{I} = \mathrm{I}_{top} - \mathrm{I}_{bottom} = \mathrm{e} * \mathrm{Q} * \sum_{i=1}^{n} N_i(dp) * n_{ave}(dp) * \eta_{ex}(dp) * (KV)^2 \tag{4-16}$$

Like the derivation in the surface monitor section, eq.(4-16) can be rewritten by including the experimental data in this section:

$$I = \mathrm{e} * \mathrm{Q} * \sum_{i=1}^{n} N_i(dp) * k * D_p^{1.6579+0.604*2} \approx \mathrm{e} * \mathrm{Q} * \sum_{i=1}^{n} N_i(dp) * k * D_p^{2.8659} \tag{4-17}$$

Even though the calculated signal was not proportional to D_p^3, the experiment was still carried out to evaluate the performance of the PM monitor. Using the same approach in the surface area monitor evaluation, different solid and liquid particle groups were used to challenge the performance of the PM monitor. Polydisperse solid particles (NaCl) and

liquid particles (DEHS) were used as the test particles. The various mean particle sizes were obtained by atomizing solutions with different concentration. Figure 4-17(a) shows the experimental curves of NaCl particles with different mean particle sizes. Differences can be observed among these three curves. The differences are even more obvious in the plot of DEHS particles, figure 4-17(b). Figure 4-17(c) shows the test particles with different standard deviation values. Likewise, differences between the curves still existed. The reason for the differences among the experimental curves might be attributed to the exponent of the particles in the measured signal, which didn't reach three.

A rough mathematic calculation was carried out to estimate the slope of the curves for particles with different size distribution. The size distribution of the generated particle cases was presented in the following equation:

$$df = \frac{1}{\sqrt{2\pi}*\ln \sigma_g} * exp\left\{-\frac{(\ln d_p - \ln \overline{d_p})^2}{2*(\ln \sigma_g)^2}\right\} d(\ln d_p) \quad (4\text{-}18)$$

Where df is the particle fraction; σ_g is the standard deviation value; $\overline{d_p}$ is the mean particle size. Total volume concentration for each case was calculated by eq.(4-3). The signal was calculated according to eq.(4-17). The generated cases had the standard deviation value ranged from 1.6 to 2.2 and the mean particle size ranged from 50 to 500 nm. Figure 4-18 shows the calculation results. The y-axis is the ratio of the normalized signal I' to the total calculated volume concentration, which denotes the slope of the curve of particles under a fixed size distribution. The x-axis is the mean particle size, while dots in the same color represent the particle groups with same standard deviation value. Under a fixed standard deviation value, it was thus found the slope values were higher in particles with smaller mean particle size. This finding was in accordance with what had shown in

figure 4-17 (a) and (b). Besides, it is also found that the slope of particles with larger standard deviation value were higher than that of particles with smaller standard value, which also agreed with figure 4-17(c). According to the experiment data and the mathematic calculation, it was concluded that the measured signals should be closed to D_p^3 for reducing the effects from size distribution variation.

Last but not least, we replotted figure 4-17(a) in figure 4-19 as an example, by changing the coordinate axis in log-scale. It's surprised to find that the differences between the curves have been minimized. This is a trick frequently used in many literatures. The log-scale axis can visually reduce the absolute variation of experimental data, and give the readers an impression of good matching. However, the difference still exists and measuring error is inevitable. This is a point for reader to keep in mind.

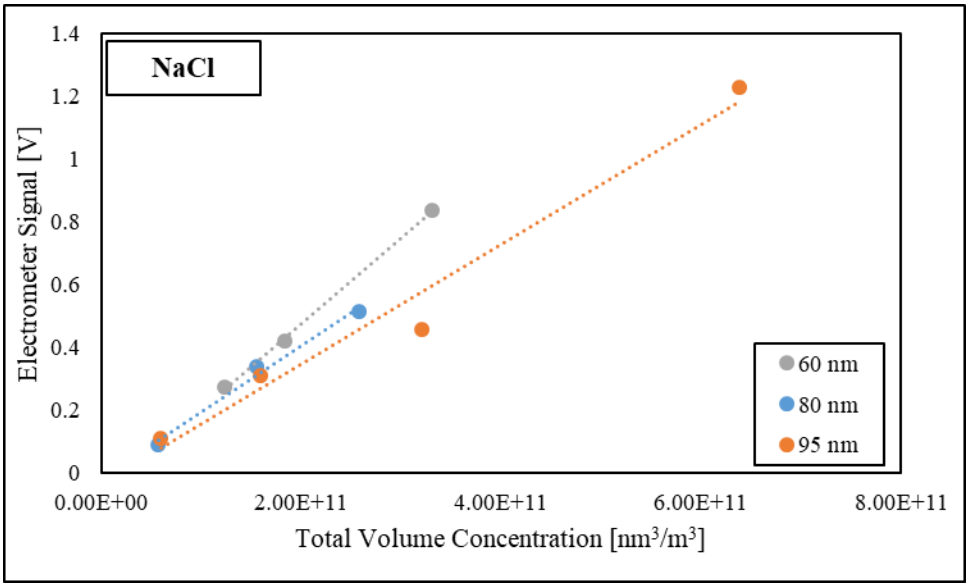
NaCl
Electrometer Signal [V]
1.4
1.2
1
0.8
0.6
0.4
0.2
0
0.00E+00
2.00E+11
4.00E+11
6.00E+11
8.00E+11
Total Volume Concentration [nm³/m³]
60 nm
80 nm
95 nm

(a)

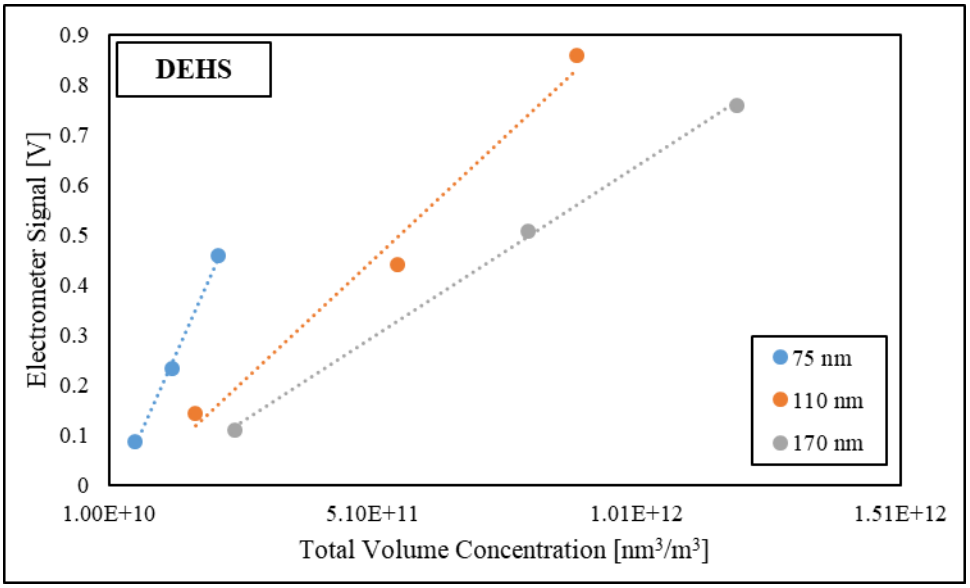
DEHS
Electrometer Signal [V]
0.9
0.8
0.7
0.6
0.5
0.4
0.3
0.2
0.1
0
1.00E+10
5.10E+11
1.01E+12
1.51E+12
Total Volume Concentration [nm³/m³]
75 nm
110 nm
170 nm

(b)

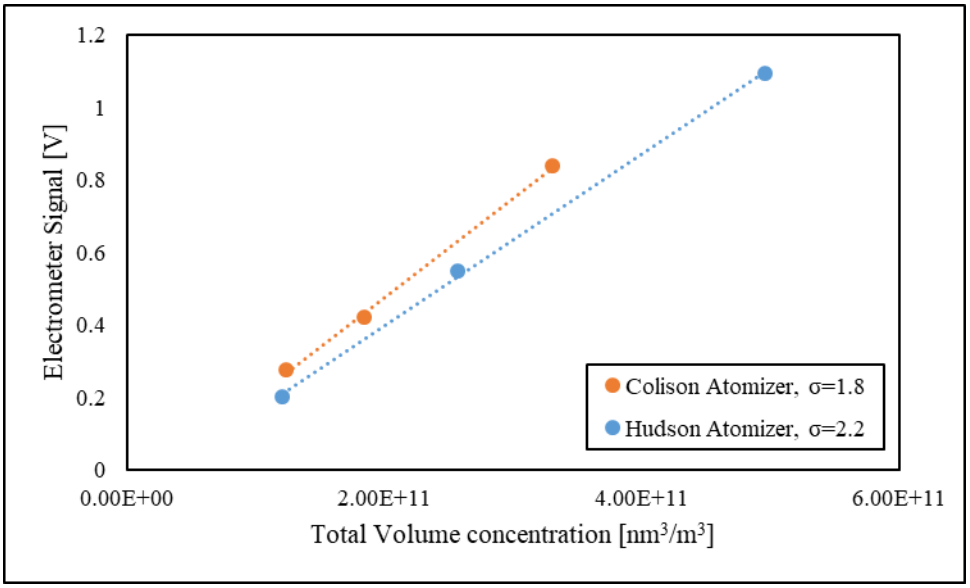

(c)

Figure 4 - 17 PM sensor correlation curves between the measured signal to the volume concentration of (a) solid particle with different mean particle size; (b) liquid particle with different mean particle size; (c) standard deviation value.

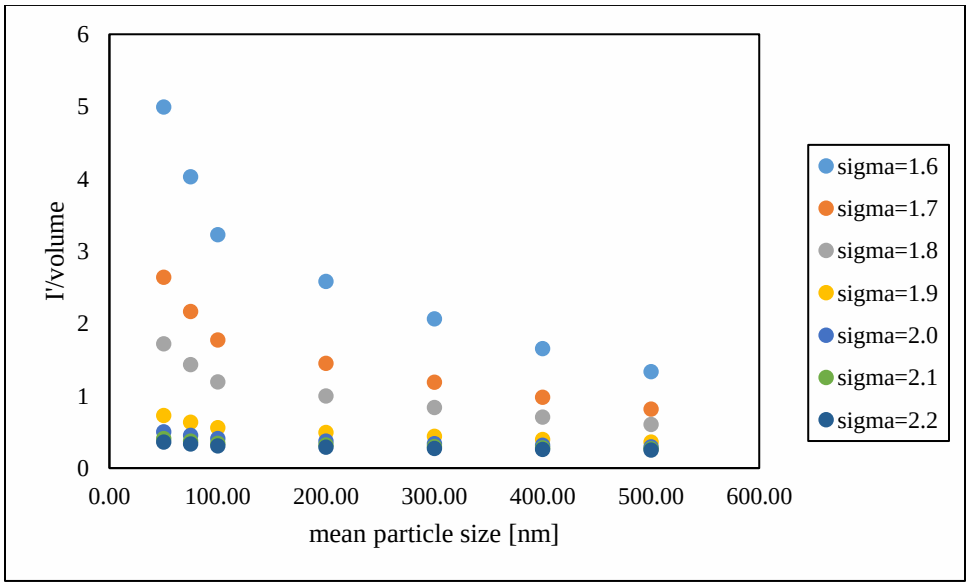

Figure 4 - 18 Mathematic calculation for predicting the slope of correlation curves of particles with different size distribution.

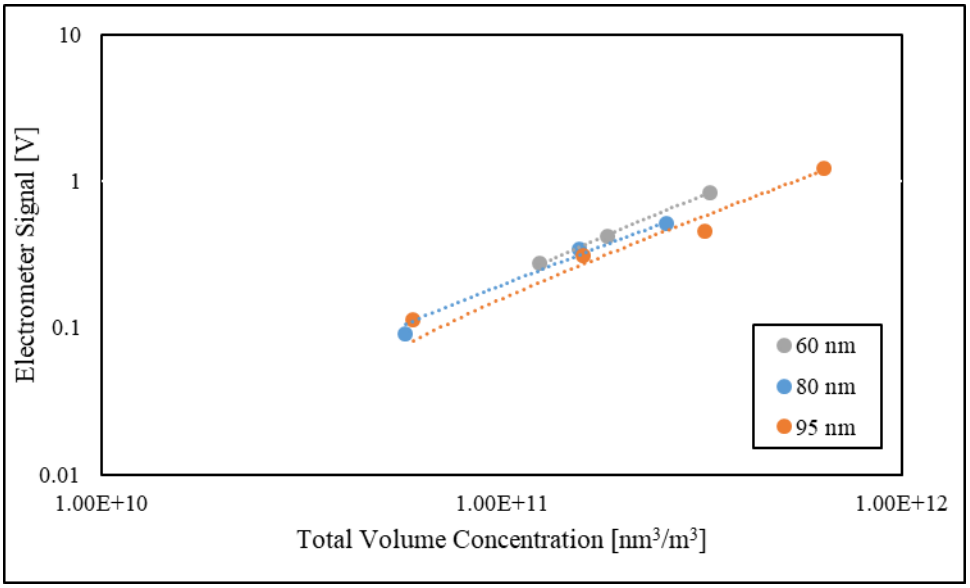

Figure 4 - 19 Replot the correlation curves between the measured signal to the volume concentration of solid particles with different mean particle sizes in log-scale axis.

4.5 Summary

An electrical PM sensor was designed and constructed in this study. The main components of this sensor are a unipolar charger, a disk-type electrostatic precipitator and sensitive current meters. The prototype charger was designed as a direct-charging type, which the corona zone was directly exposed to particles. The performances of charging efficiency and mean charge per particle were experimentally evaluated. The penetration curves of the electrostatic precipitator were also obtained for particles with different electrical mobility. By assembling the charger, precipitator and the current monitor (i.e., electrometer) together, the PM sensor was evaluated as both total surface area and volume concentration monitor. Polydisperse particles with different mean particle sizes, standard deviation values and materials were used as test particles. By monitoring the current from the top plate of the precipitator, the prototype PM sensor was capable of measuring the total surface area concentration of particles. The performance was less affected by the physical properties and chemical composition of the test particles. In addition, by measuring the current from both plates of the precipitator, the PM sensor was used as a mass monitor. The measured signal was the difference between the two measured currents. However, the experimental curves from different test particle groups showed observable difference. This is because the measured signal of each particle size was not proportional to the particle volume. Further improvements are thus needed to enable the PM sensor for particle volume measurement.

4.6 Reference

Amanatidis, S., et al. (2013). Applicability of the Pegasor Particle Sensor to Measure Particle Number, Mass and PM Emissions, SAE International.

Bau, S., et al. (2012). "Evaluating three direct-reading instruments based on diffusion charging to measure surface area concentrations in polydisperse nanoaerosols in molecular and transition regimes." Journal of Nanoparticle Research 14(11): 1217.

Cao, L. N. Y., et al. (2017). "Development of a geometric surface area monitor (GSAM) for aerosol nanoparticles." Journal of Aerosol Science 114(Supplement C): 118-129.

Cohen, A. J. and C. A. Pope (1995). "Lung cancer and air pollution." Environmental Health Perspectives 103(Suppl 8): 219-224.

Fierz, M., et al. (2011). "Design, Calibration, and Field Performance of a Miniature Diffusion Size Classifier." Aerosol Science and Technology 45(1): 1-10.

Fierz, M., et al. (2014). "Aerosol Measurement by Induced Currents." Aerosol Science and Technology 48(4): 350-357.

Lelieveld, J., et al. (2015). "The contribution of outdoor air pollution sources to premature mortality on a global scale." Nature 525: 367.

Li, L., et al. (2009). "Evaluation of an electrical aerosol detector (EAD) for the aerosol integral parameter measurement." Journal of Electrostatics 67(5): 765-773.

Liu, B. Y. and K. Lee (1975). "An aerosol generator of high stability." American Industrial Hygiene Association Journal 36(12): 861-865.

Liu, Q.-L. and D.-R. Chen (2014). "A programmable aerosol diluter for generating time-varied sub-micrometer particles." Aerosol Air Qual Res 14: 1838-1850.

Marra, J., et al. (2009). "Nanoparticle monitoring for exposure assessment." IEEE Nanotechnology Magazine 3(2): 6-37.

Marra, J., et al. (2010). "Monitor for detecting and assessing exposure to airborne nanoparticles." Journal of Nanoparticle Research 12(1): 21-37.

Ntziachristos, L., et al. (2007). "Application of a Diffusion Charger for the Measurement of Particle Surface Concentration in Different Environments." Aerosol Science and Technology 41(6): 571-580.

Qi, C., et al. (2008). "Fundamental Study of a Miniaturized Disk-Type Electrostatic Aerosol Precipitator for a Personal Nanoparticle Sizer." Aerosol Science and Technology 42(7): 505-512.

Pope, I. C., et al. (2002). "LUng cancer, cardiopulmonary mortality, and long-term exposure to fine particulate air pollution." JAMA 287(9): 1132-1141.

Potera, C. (2014). "Toxicity beyond the Lung: Connecting PM($_{2.5}$), Inflammation, and Diabetes." Environmental Health Perspectives 122(1): A29-A29.

Shin, W. G., et al. (2007). "Calibration and numerical simulation of Nanoparticle Surface Area Monitor (TSI Model 3550 NSAM)." Journal of Nanoparticle Research 9(1): 61-69.

Todea, A. M., et al. (2017). "Inter-comparison of personal monitors for nanoparticles exposure at workplaces and in the environment." Science of the Total Environment 605-606: 929-945.

Vosburgh, D. J. H., et al. (2014). "Evaluation of a Diffusion Charger for Measuring Aerosols in a Workplace." Annals of Occupational Hygiene 58(4): 424-436.

Wilson, W. E., et al. (2007). "Use of the Electrical Aerosol Detector as an Indicator of the Surface Area of Fine Particles Deposited in the Lung." Journal of the Air & Waste Management Association 57(2): 211-220.

CHAPTER 5 Development of small cyclones as size-selective inlet

5.1 Introduction

Cyclones are particle separators that separate particles according to their inertia performance in flow field. Because of their simple design, low-cost in manufacturing, operating and maintenance, cyclones are widely used in many fields. In industry, large-scale cyclones are used to remove debris, large particulate or abrasive material in the air stream, which can greatly reduce maintenance time and extend filter life for emission system.

Particulate matter (PM) have been identified as one of the air pollutant, and many epidemiologic studies have shown their adverse health effects on the human being. (Fan, et al. 2015; Pui, et al. 2014; Potera, 2014; Samoli, et al. 2013; Evans, et al. 2013; Ma, et al. 2011). Therefore, in order to monitor the personal exposure to the particulate matter, the development of the personal particle sensors become popular. Many small size cyclones are developed as size-selective inlet for these compact particle monitors to remove large particles in the sampling stream, which can reduce the measurement error caused by these large particles. Besides working as size-selective inlets, some small size cyclones can be used standalone as personal particle collectors (Görner, et al., 2001).

Previous researches have been conducted to investigate the performance of some small cyclones. Three low flowrate cyclone families for personal sampling have been developed and tested by Kenny and Gussman in 2000. Hsiao (2009) developed two miniature cyclones to remove particles larger than 1.0 and 0.3 μm, respectively, at the flow rate of 0.3 lpm. However, the proper use of a cyclone requires keeping the aerosol inlet

always facing the desired sampling direction. Such sampling requirement is not easy to achieve in field studies, especially in the studies related to personal exposure. Moreover, it is not easy to get representative sampling with one-inlet cyclone when ambient UFPs are not uniform in spatial. One of the possible solutions to remedy the above issue is to use cyclones with multiple inlets.

Besides, some researches had pointed out the body shape effects on cyclone performance. Kenny and Gussman mentioned that the cone part has an important impact on cyclone performance (2000). Avci and Karagoz concluded that increasing the body contract angle of cyclone can cause a considerable increase in the collection efficiency and pressure drop (Avci and Karagoz, 2003). Xiang also inspected three cyclones with different body angle and drew the same conclusion (Xiang et al., 2001) as Avci and Karagoz. However. the body of these small cyclones in the previous studies are usually cylindrical or contain a tapered part which is connected after a cylindrical part. The tapered body can maintain/increase the tangential velocity, which might improve the performance of a cyclone. However, as particle flow swirling in the cylindrical body firstly, tangential velocity decreases due to fiction loss, which might reduce the contribution of the tapered part. Therefore, the hypothesis of maximizing the conical body in a cyclone to increase the centrifugal force effect has been proposed. Park studied a three stages cyclone separator in 2015, which inspired an idea of a cyclone with only the tapered body.

In this chapter, two types of small cyclone were developed. One was a quadru-inlet cyclone for solving the directional sampling issue, which always encountered in a single-inlet cyclone. The other type was a group of cyclones only contain the tapered body, which aim to maximize the performance of the traditional design cyclones.

5.2 Design of the prototype cyclone

5.2.1 Design of the quadru-inlet cyclone

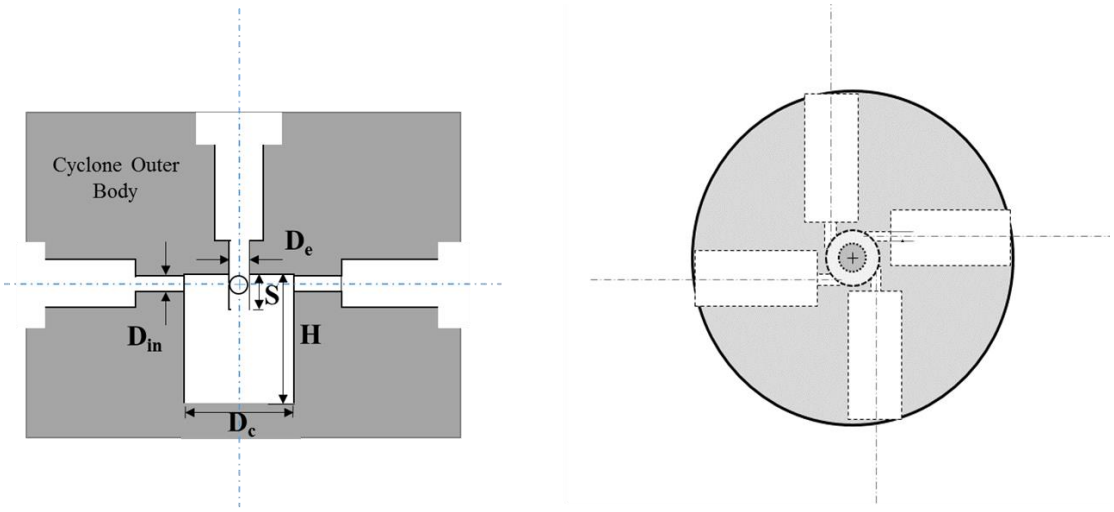

Figure 5 - 1 Schematic diagram of the prototype quadru-inlet cyclone.

A miniature quadru-inlet cyclone is designed. It has advantages on solving the directional sampling issue, which are often encountered in a single-inlet cyclone.

Table 5 - 1 Dimension of the prototype quadru-inlet cyclone

Model	Dc (mm)	Din (mm)	Ain (mm^2)	De (mm)	S (mm)	H (mm)
Quadru-inlet cyclone	3.91	0.56	0.98	1.02	1.60	5.08

Figure 5-1 shows the schematic diagram of the prototype quadru-inlet cyclone. The cyclone body configuration of this cyclone is similar to those named as extra-sharp-cut cyclones (ESCCs) in the work of Kenny, Gussman and Meyer (Kenny at el., 2000), which have a sharp particle penetration curve and simple geometry. The cross-sections of the inlets were circular. They were installed tangentially to the inner wall of cyclone body. The base of this quadru-inlet mini-cyclone was attached to the cyclone body by threads, enabling the easy cleaning of the prototype. Table 5-1 shows the detail dimensions of the prototype quadru-inlet mini-cyclone (i.e., the inlet diameter, D_{in}; the total inlet area, A_{in};

the cyclone body diameter, D_c; the outlet diameter, D_e; the vortex finder length, S; and the cyclone body length, H).

5.2.2 Design of the tapered body cyclone

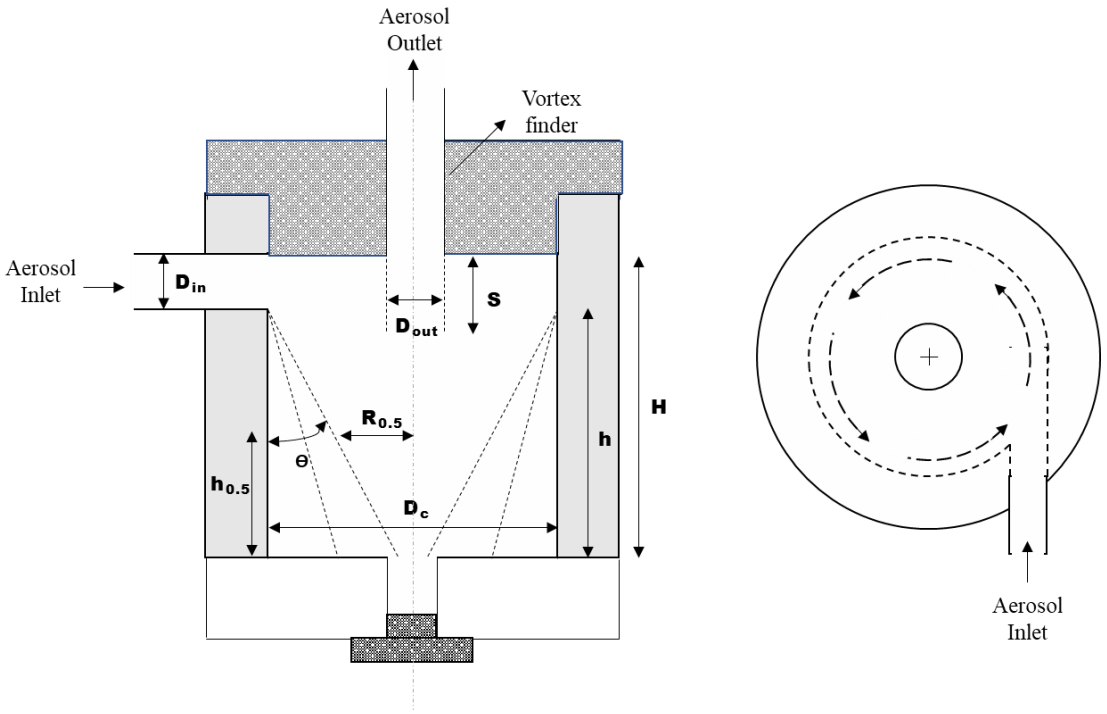

Figure 5 - 2 Schematic diagram of the prototype tapered body cyclones.

Figure 5-2 (i.e., the side and top cross-sectional views) shows the schematic diagram of studied cyclones. The flow is tangentially introduced into the studied cyclones. A majority of key dimensions remains the same for all studied cyclones except the contraction angle, Θ, of cyclone body is varied (i.e., 0º, 15º and 30º). At the contraction angle, Θ, of zero, the studied cyclone is the same as the extra-sharp-cut cyclone (ESCC) studied by Kenny and Gussman (2000). The above cyclone was used as the reference. The other two cyclones have the conical contraction angles of 15° and 30°. Note that the conical contraction of cyclone body started right below the cyclone inlet in the above two cyclones

(i.e., no cylindrical body section). A vortex finder (as the cyclone outlet) tube was installed at the cyclone cap. The overall size of these studied cyclones is comparable to the size of a US quarter coin. Table 5-2 shows the key dimensions of studied cyclones: the inlet diameter (D_{in}), the body diameter (D_c), the outlet diameter (D_{out}), the insertion length of the vortex finder (S), the cyclone body length (H), the contraction body height (h) and the cyclone body contraction angle (Θ).

Table 5 - 2 Geometrical dimensions for the prototype cyclones.

Θ (°)	D_c (inch)	D_{in} (inch)	D_{out} (inch)	S (inch)	h (inch)	H (inch)
0, 15 or 30	0.635	0.125	0.068	0.2, 0.35 or 0.5	0.5	0.625

5.3 Experimental Setup for Cyclone Performance Evaluation

5.3.1 Experimental setup for pressure drop measurement

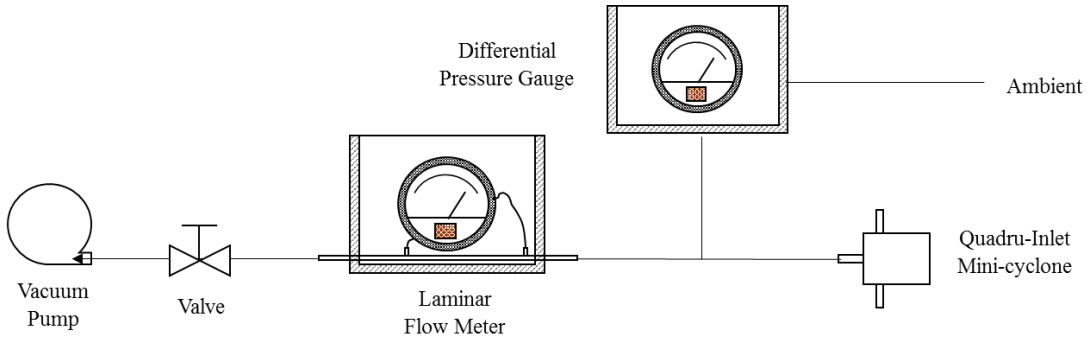

Figure 5 - 3 Schematic diagram of experimental setups for performance pressure drop evaluation of the quardru-inlet cyclone.

Experimental setups showed in Figure 5-3 are built for evaluating the cyclone pressure drop. The pressure drop of both the quadru-inlet cyclone and the tapered body cyclones were evaluated under different flowrates. The sampling flowrate was controlled by a needle valve which connected to a vacuum pump, and monitored by a laminar flowmeter. The laminar flowmeter was calibrated by the primary flow calibrator

(Gilibrator-2, SENSIDYNE 800271). The pressure drop of the cyclone was then measured by a differential pressure gauge (Series 2000, Magnehelic).

5.3.2 Experimental setup for particle penetration curve measurement

5.3.2.1 The quadru-inlet cyclone setup

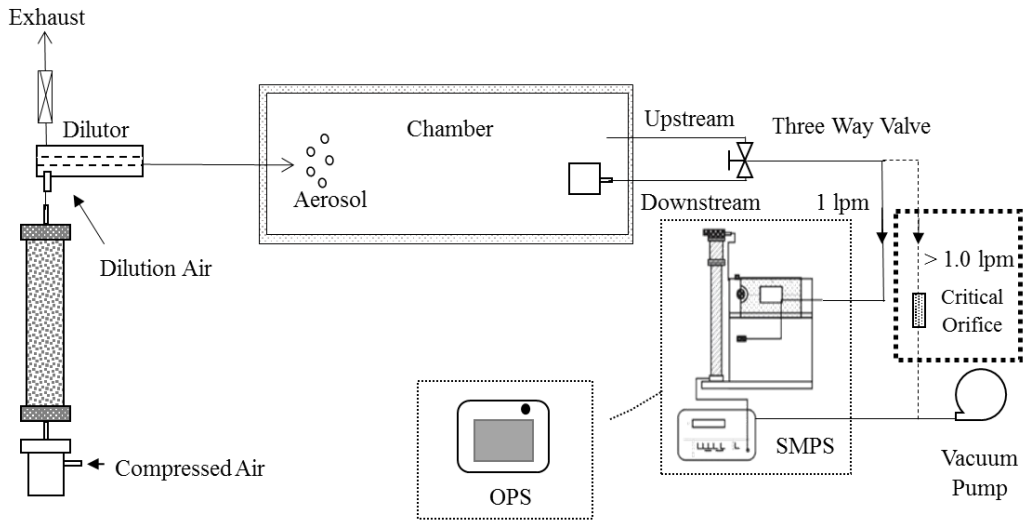

Figure 5 - 4 Schematic diagram of experimental setups for performance particle penetration curve evaluation of the quardru-inlet cyclone.

The schematic diagram of the experimental setup to calibrate the particle penetration of the studied quadru-inlet mini-cyclone is shown in Figure 5-4. A custom-made Colison atomizer was used to generate polydisperse NaCl particles. Generated polydisperse NaCl particles were passed through a diffusion dryer (with silica gel as the desiccant), aerosol dilutor and a charge neutralizer prior to entering the test chamber. Two sampling tubes were placed at the bottom of the test chamber; one was used as the downstream tube for the studied cyclone and the other as the upstream particle sampling probe. A three-way valve was used in the setup for measuring particles at the upstream and downstream of the cyclone. Depending on the particle size range sampled particles were characterized by either a scanning mobility particle sizer (SMPS, TSI 3096) or an optical

particle sizer spectrometer (OPS, TSI 3330). Additional air was further provided in the setup to meet the sampling flowrate required for the sizers. A critical-orifice flowmeter connected at the inlet of the vacuum pump was applied to control the make-up flowrate while making sure the prototype cyclone was operated at the desired flowrate. To acquire the penetration curves, consequently determining the particle cutoff size of the prototype at a given flowrate, size distributions of particles at the upstream and downstream of the prototype were measured. The particle penetration as a function of particle size was then derived from the measured upstream and downstream particle size distributions. The prototype cyclone was tested at four different flowrates (i.e., 1.0, 1.5, 2.0 and 4.0 l/min).

5.3.2.2 the tapered body cyclone

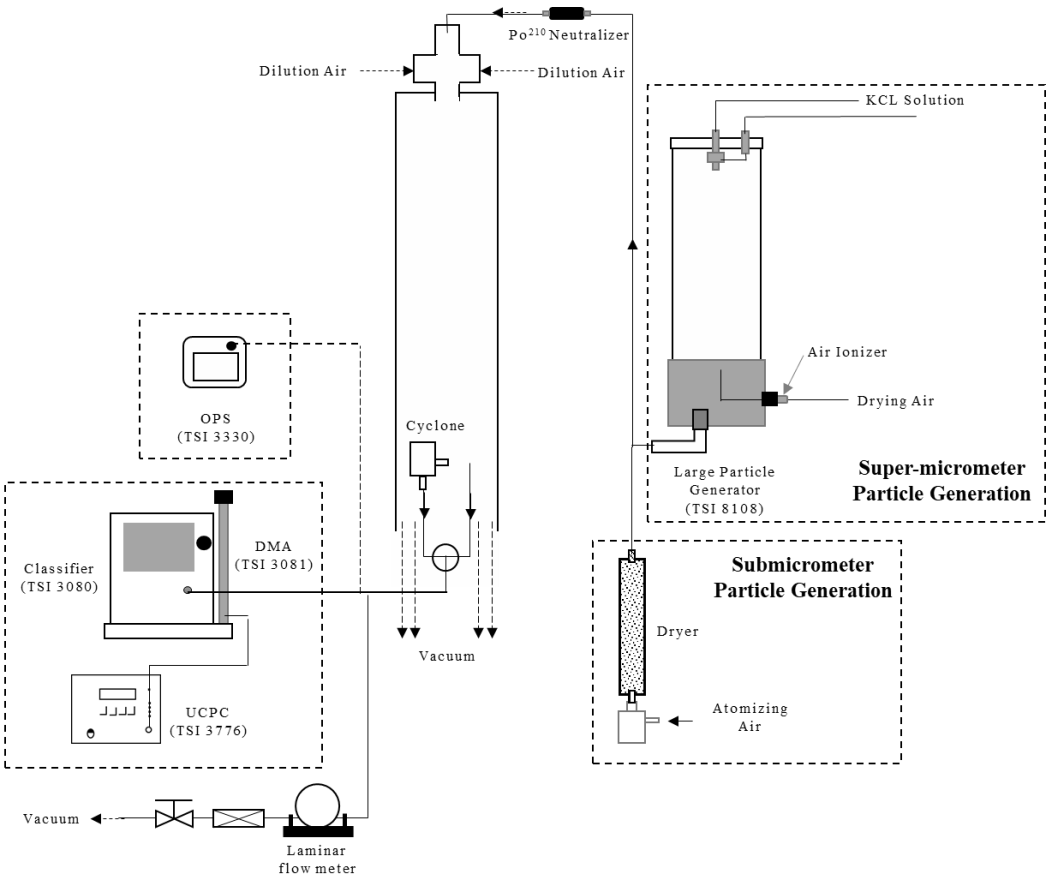

Figure 5 - 5 Schematic diagram of experimental setups for the penetration curve testing of the tapered body cyclones.

Figure 5-5 shows the schematic diagram of the experimental setup for the measurement of cyclone particle penetration curve. The studied cyclones were challendged by particles in a wide particle size range, i.e. 30 nm to 10 μm. Two sets of experimental setups were used for this part of evaluation: one is for sub-micrometer particle testing and the other is for super-micrometer particle testing. Particle generators and particle detectors were different in both setups.

The test chamber, installed vertically, was a cylindrical PVC pipe with 0.09 m in diameter and 1.5 m in height. A PVC cross connector was attached to the chamber top for introducing test particles from the top opening of the cross and filtered dilution flow from both side openings of the cross. Studied cyclone was placed near the bottom of the chamber. A three-way valve with one channel connected to the cyclone and the other one directly to a sampling tube for upstream particle measurement. By switching the valve channel, the particle size distributions at the upstream and downstream of the studied cyclones were measured. A vacuum pump was applied at the chamber bottom to vent the excess flow.

For the submicrometer particle testing, a custom-made Collison atomizer was used to generate polydisperse droplets containing KCl. Before introducing into the test chamber, generated droplets were dried in a diffusion dryer with Silica gel as the desiccant and charge-minimized by a radioactive Po^{210} neutralizer. The scanning mobility particle sizer (SMPS, TSI 3096) was used to measure the particle size distributions upstream and downstream of a studied cyclone. In the super-micrometer particle testing, the large particle generator (TSI 8108) were used to generate super-micrometer-sized KCL particles. In the large particle generator, testing particles were generated by spraying a KCl solution via a

mechanical sprayhead and mixing with drying air carried with bipolar ions. An optical particle sizer (OPS, TSI 3330) was used to characterize the size distributions of super-micrometer-sized particles. The particle penetration curves of studied cyclones were obtained by taking the ratio of the particle concentration in each size bin at the cyclone downstream to that at the upstream.

Prototype cyclones were tested under five different flowrates (i.e., 1.0, 2.0, 3.0, 5.0 and 7.0 l/min). A makeup flow line with a HEPA filter cartridge, a laminar flow meter, a needle valve and a vacuum pump was included in the measurement line to ensure the operational flow rate of a studied cyclone.

5.4 Results and Discussion

5.4.1 Pressure drop of the quadru-inlet mini-cyclone

Figure 5-6 plots the experimental pressure drop data for the quadru-inlet cyclone as a function of the cyclone inlet velocity, under one-, two- and three- inlets opened conditions. In the two-inlet opened condition, two scenarios were included: one was that the two blocked inlets were at opposite position, while the other case was that the two blocked inlets were at the side-by-side position. The pressure drop values of the quadru-inlet cyclone increased quadratically as the inlet velocity increased. However, there is no obvious difference from the two cases of the two-inlets opened condition. The pressure drop of this cyclone can thus be simply modeled by the inlet dynamic pressure (i.e., $\rho_g V_i^2/2$) with a dimensionless loss coefficient, K_L:

$$\Delta P = K_L * \frac{\rho_g * V_i^2}{2}, \quad (5\text{-}1)$$

where ρ_g is the gas density and V_i is the inlet velocity. The fitted K_L value is 14.2, 10.8, 6.3 and 2.6 for four-, three-, two- and one- inlet open, respectively. The K_L value can be expressed as a function of inlet number, n:

$$K_L = 3.93 * n - 1.35, \quad n \leq 4 \tag{5-2}$$

The linear relationship between the K_L value and the inlet number n implies that the pressure drop of the quadru-inlet cyclone was primarily attributed to the flow pressure drop in the cyclone body, not at the cyclone inlets.

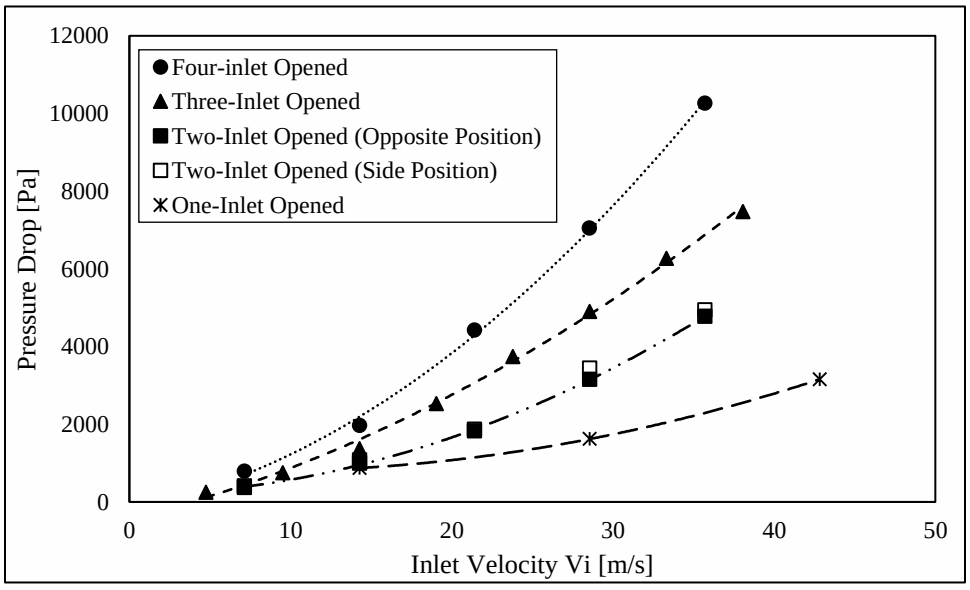

Figure 5 - 6 Pressure drop as a function of inlet velocity of the quardru-inlet cyclone.

Instead of using the inlet velocity as the abscissa, figure 5-7 replots the experimental pressure drop values for the quadru-inlet cyclone as a function of the cyclone total flowrate. The data of the quadru-inlet cyclone were under four-inlet opened condition. Besides, the pressure drop values of mini-cyclone developed by Hsiao et al. were also

included in figure 5-7. It shows that the quadru-inlet cyclone has a lower pressure drop than Hsiao's mini-cyclones when operated at the same flowrate.

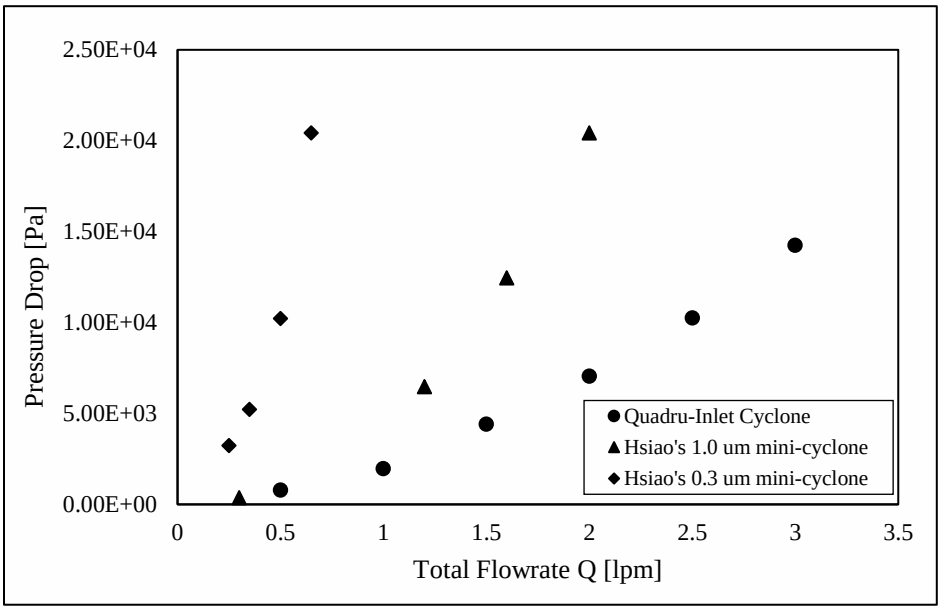

Figure 5 - 7 Pressure drop as a function of the aerosol flow rate.

5.4.2 Pressure drop of the tapered body cyclones

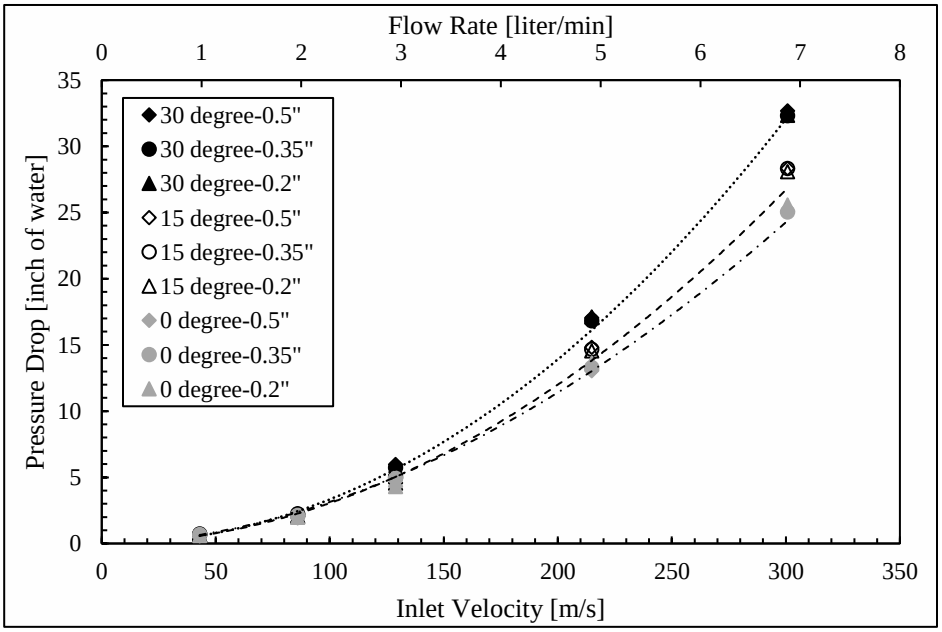

Figure 5 - 8 Pressure drop as a function of inlet velocity and sampling flowrate of the prototype cyclones.

Figure 5-8 shows the experimental pressure drop of the studied cyclones as a function of the both inlet velocity and sampling flowrate. The pressure drop data of the studied cyclones with three different body contract angles (i.e., 0°, 15° and 30°) and three insertion lengths (i.e., 0.2, 0.35 and 0.5 inch) were included in this figure. It was found that the cyclone pressure drop varied with the cyclone body contraction angle. At the same operational flow rate, the cyclone with 30° body contraction angle has the highest pressure drop and one with the 0° body contraction angle has the lowest. The effect of vortex finder length on the cyclone pressure drop was found negligible for each tested cyclone under the same operational flow rate.

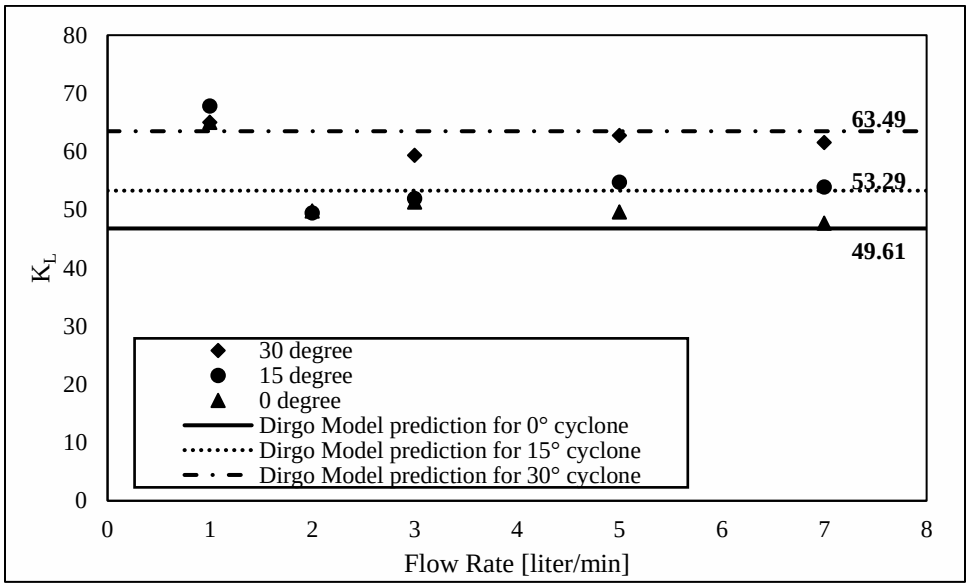

Figure 5 - 9 Comparison of the loss coefficient (K_L) as a function of inlet velocity for the prototype cyclones, predicted by the Dirgo.

Similar to the other small size cyclones, the pressure drop values of these cyclones increased quadratically as the inlet velocity increased. Therefore, the inlet dynamic pressure ($\rho_g V_i^2/2$) multiplied by a dimensionless loss coefficient (K_L) can be used to model the pressure drop of these cyclones. The fitted values K_L are 49.61, 55.59 and 62.17 for these tapered body cyclones with 0°, 15° and 30° body contract angle, respectively. Many

studies had proposed semi-empirical model to predict the dimensionless loss coefficient (K_L) for calculating cyclone pressure drop. However, none of these models are for the cyclone with purely tapered body. Hsiao (2009) used Dirgo model to calculate the value of K_L for his mini-cyclones, which are cylindrical body. In this study, the prototype cyclone with 0° body contract angle are similar to Hsiao's mini-cyclone. Dirgo model gave a reasonable prediction for this prototype cyclone with 0° body contract angle, but not for the cyclone with 15° and 30° body angle. Therefore, a semi-empirical model based on the Dirgo's model, was proposed to calculate the value of K_L for the taped-body cyclone. The working equation of Dirgo and the proposed model in this study are shown as follows:

(1) Dirgo Model

$$K_L = 19.7 * \left(\frac{ab}{D_e^2}\right)^{0.99} * \left(\frac{S}{D_c}\right)^{0.35} * \left(\frac{H}{D_c}\right)^{-0.34} * \left(\frac{h}{Dc}\right)^{-0.35} * \left(\frac{B}{D_c}\right)^{-0.33} \quad (5\text{-}3)$$

(2) Proposed model

$$K_L = 17.81 * \left(\frac{ab}{D_e^2}\right)^{0.99} * \left(\frac{S}{D_c}\right)^{0.35} * \left(\frac{H}{D_c}\right)^{-0.33} * \left(\frac{H-h}{Dc}\right)^{-0.06} * \left(\frac{B}{D_c}\right)^{-0.095} \quad (5\text{-}4)$$

As shown in Figure 5-9, the K_L values of the prototype cyclones can be reasonably estimated by the new proposed model. The proposed model was also checked for Hsiao's mini-cyclone (2009) and Liu's quadru-inlet cyclone (2015). The results were also showing a good agreement.

5.4.3 Particle penetration curve of the quadru-inlet mini-cyclone

The particle penetration curve is the other parameter to evaluate cyclone performance, which is obtained by taking the ratio of the concentration in the downstream

to that in the upstream. The cutoff particle size, $D_{p,50}$, defined as the particle size at 50% particle penetration, is one of the key performance parameters for a cyclone. Both the penetration curves of the quadru-inlet mini-cyclone and the tapered body cyclone were obtained under different conditions.

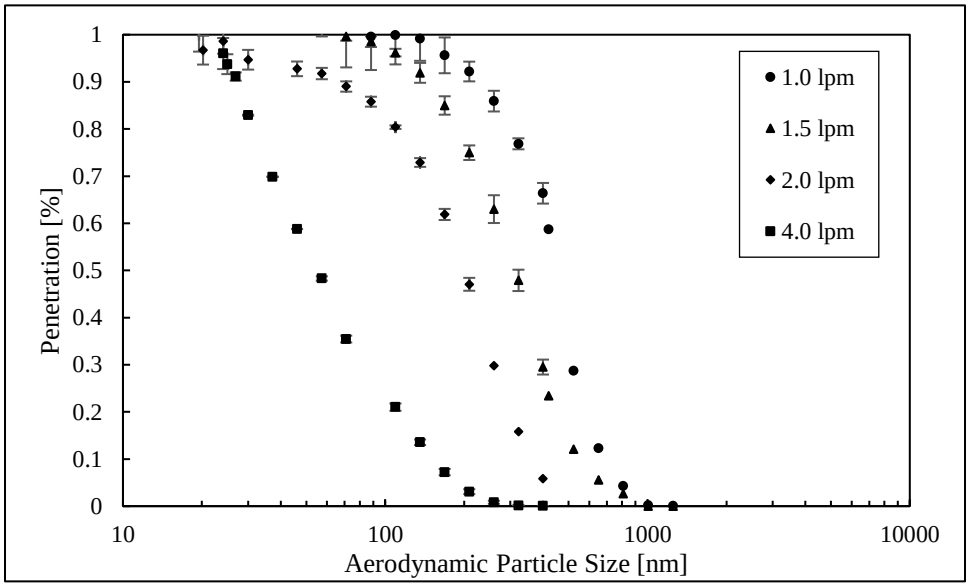

Figure 5 - 10 Particle penetration as a function of aerodynamic particle size for the quadru-inlet cyclone.

Figure 5-10 shows the particle penetration curves as a function of particle size for the studied quadru-inlet cyclone at four different flowrates, i.e., 1.0, 1.5, 2.0 and 4.0 liter/min. The cutoff particle sizes for the quadru-inlet cyclone are 430, 299, 200 and 53.3 nm at 1.0, 1.5, 2.0 and 4.0 liter/min flow rates, respectively. As the operational flowrate increased, the cutoff particle sizes of the cyclone decreased. This is because that in high operation flowrate, the smaller cutoff particle size is resulted from the stronger centrifugal force.

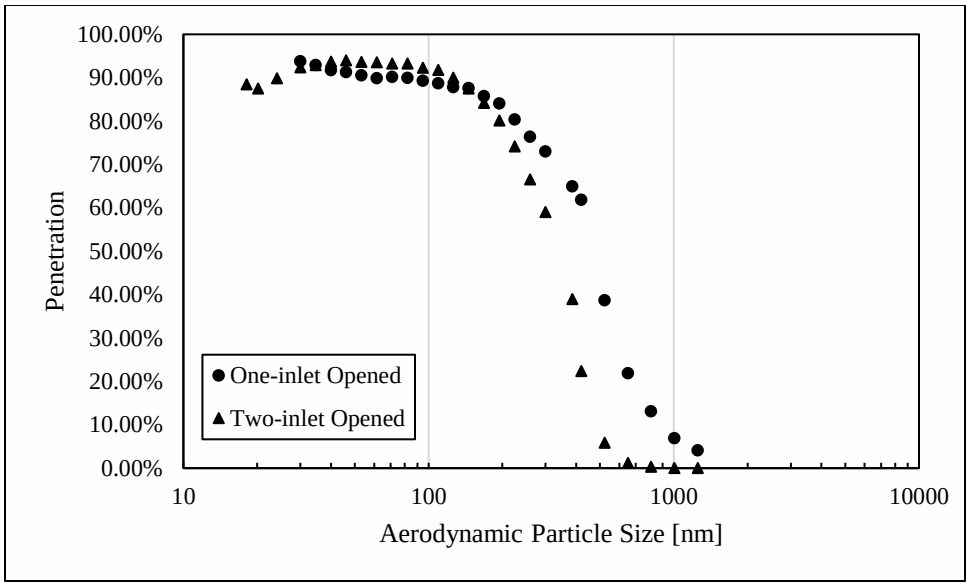
100.00%
90.00%
80.00%
70.00%
60.00%
50.00%
40.00%
30.00%
20.00%
10.00%
0.00%
Penetration
One-inlet Opened
Two-inlet Opened
10
100
1000
10000
Aerodynamic Particle Size [nm]

(a)

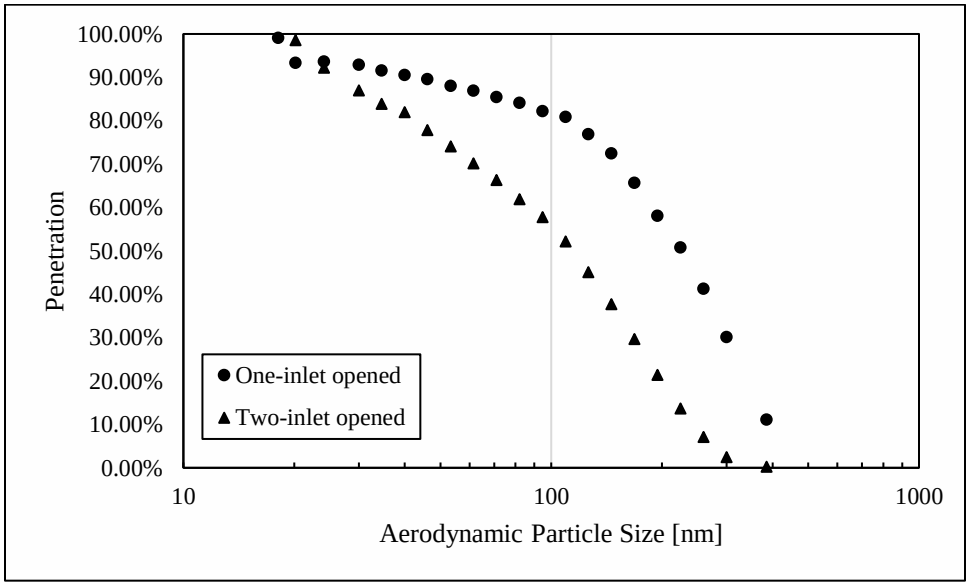
100.00%
90.00%
80.00%
70.00%
60.00%
50.00%
40.00%
30.00%
20.00%
10.00%
0.00%
Penetration
One-inlet opened
Two-inlet opened
10
100
1000
Aerodynamic Particle Size [nm]

(b)

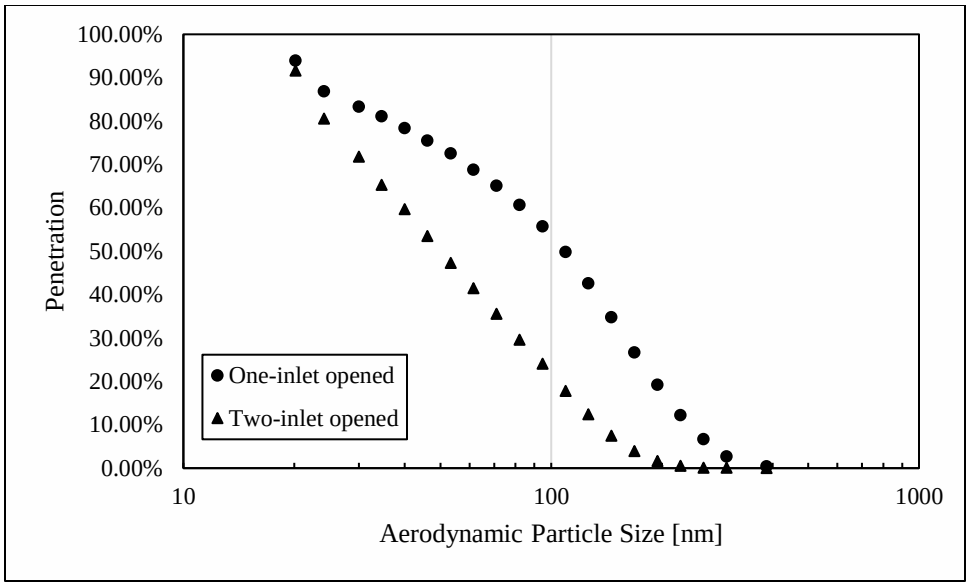

(c)

Figure 5 - 11 Particle penetration as a function of aerodynamic particle size for the quadru-inlet cyclone under one- or two-inlet opened condition. (a) Vin=28.6m/s; (b) Vin=57.1m/s;(c) Vin=85.7m/s

Figure 5-11 shows the particle penetration curves as a function of particle size for the studied quadru-inlet cyclone under two different conditions: one- or two- inlet opened. The inlet velocity in each plot are the same for both two conditions. It shows that smaller particle cutoff size can be obtained at two-inlet opened condition when the cyclone was operated under the same inlet velocity.

5.4.4 Particle penetration curve of the tapered body cyclones

(1) Body angle effect

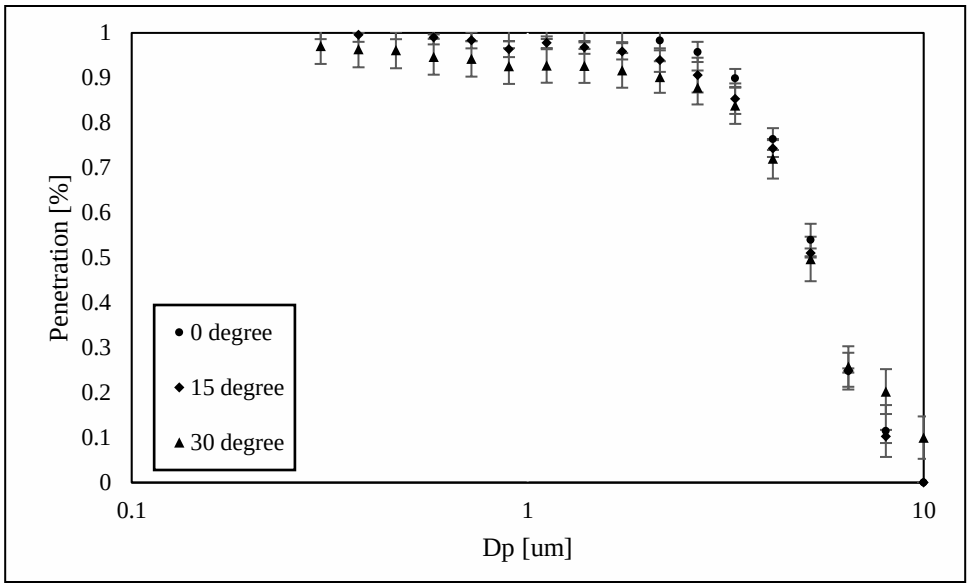
Penetration [%]
1
0.9
0.8
0.7
0.6
0.5
0.4
0.3
0.2
0.1
0
0.1
1
10
Dp [um]
0 degree
15 degree
30 degree

(a)

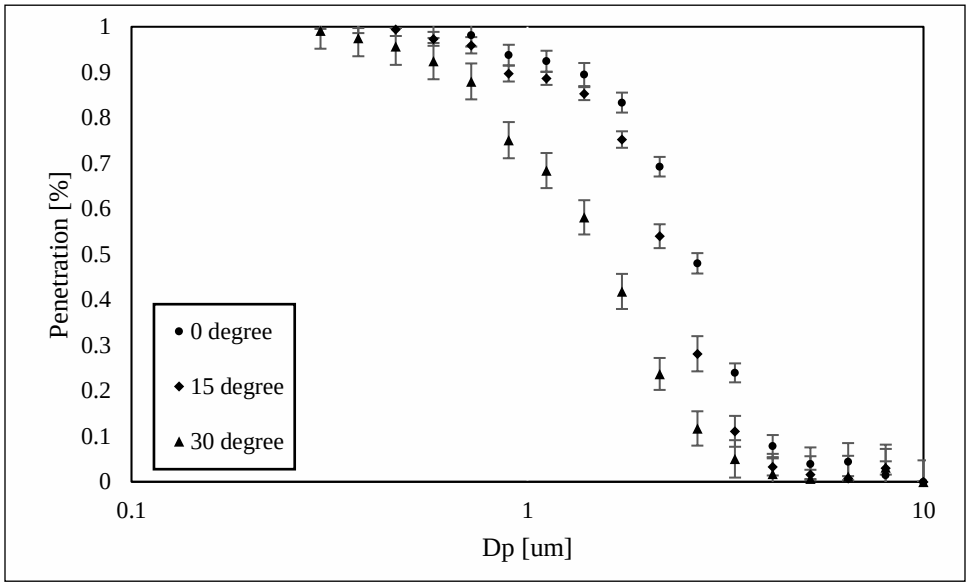
Penetration [%]
1
0.9
0.8
0.7
0.6
0.5
0.4
0.3
0.2
0.1
0
0.1
1
10
Dp [um]
0 degree
15 degree
30 degree

(b)

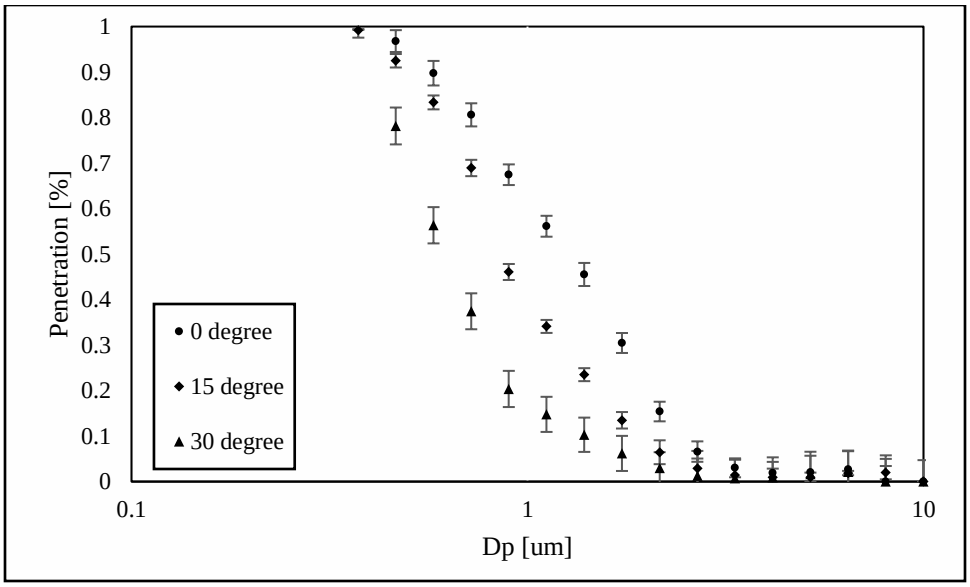

(c)

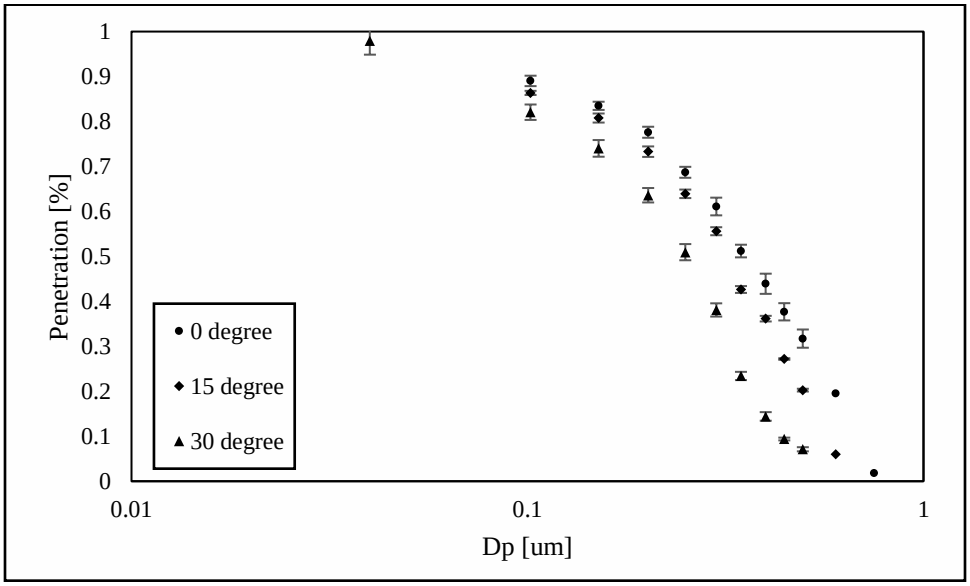

(d)

Figure 5 - 12 Particle penetration as a function of aerodynamic particle size for the prototype cyclones with different body contract angles. (a) 1.0 lpm sampling flowrate; (b) 2.0 lpm sampling flowrate; (c) 3.0 lpm sampling flowrate; (d) 5.0 lpm sampling flowrate.

Figure 5-12 shows the particle penetration curves as a function of aerodynamic particle size for the studied cyclones at four different sampling flowrates (i.e.,1.0, 2.0, 3.0 and 5.0 lpm). In each figure, it includes penetration curves from the tested cyclone with different

body contract angle (i.e., 0°, 15° and 30°). Under the same sampling flowrate, the particle cut-off size of the three prototype cyclones decrease with the increase of contract angles. This represents that the cyclone with larger body contract angle can remove more large particles than that of the cyclone with smaller body contract angle. This is because the cyclone with larger body contract angle has smaller cross section area compare to the that of the cyclone with smaller contract angle at the same height, which results in higher tangential velocity. The higher tangential velocity represents stronger centrifugal force, and leads to smaller particle cut-off size.

In additon, when the sampling flow rate was low (i.e., less than 1.0 lpm), the differences seem to be unobservable among the three cyclones with different body contract angle. This is in accordance with what had been found in the pressure drop performance: at low sampling flowrate, the pressure drop difference among the three cyclones are quite small (Figure 5-8), which results in negligible difference in particle cut-off size. Besides, as the flowrate increased, the differences on particle cut-off size among the three cyclones also increased. The maximum differences on particle cut-off size can be achieved around 2.0 lpm to 3.0 lpm. After that, as the flow rate increased, the differences started to decrease. This indicated that there is a range for sampling flow rate, where the "input-to-output ratio" can be maximized. This will be discussed in the detail in the pressure drop and cut-off size relationship paragraph.

(2) Flowrate effect

The prototype cyclones were also tested under different sampling flowrate. Figure 5-13 shows the particle penetration curves as a function of aerodynamic particle size for the

studied cyclones with different body contract angle under different sampling flowrates (i.e., 1.0, 2.0, 3.0, 5.0 and 7.0 liter/min). As expected, the particle cut-off size decreased as increasing sampling flowrate, due to increment of centrifugal force. The particle cut-off size for the three tapered body cyclones at different sampling flowrates are listed in Table 3. Monodisperse polystyrene latex (PSL) particles of 2.6um, 2.0um and 1.6um, were also used to verify the results from the polydisperse KCl particles testing at 2.0 lpm sampling flowrate for each cyclone. The results were consistent with the polydisperse particle data.

Table 5 - 3 Cutoff sizes for prototype tapered body cyclones under different flowrates.

Q [lpm]		1	1.5	2	3	5	7
D_{50} [um]	Θ=0°	5.486	3.427	2.602	1.437	0.355	0.231
	Θ=15°	5.470	3.555	2.263	0.944	0.320	0.204
	Θ=30°	5.203	2.842	1.740	0.653	0.254	0.174

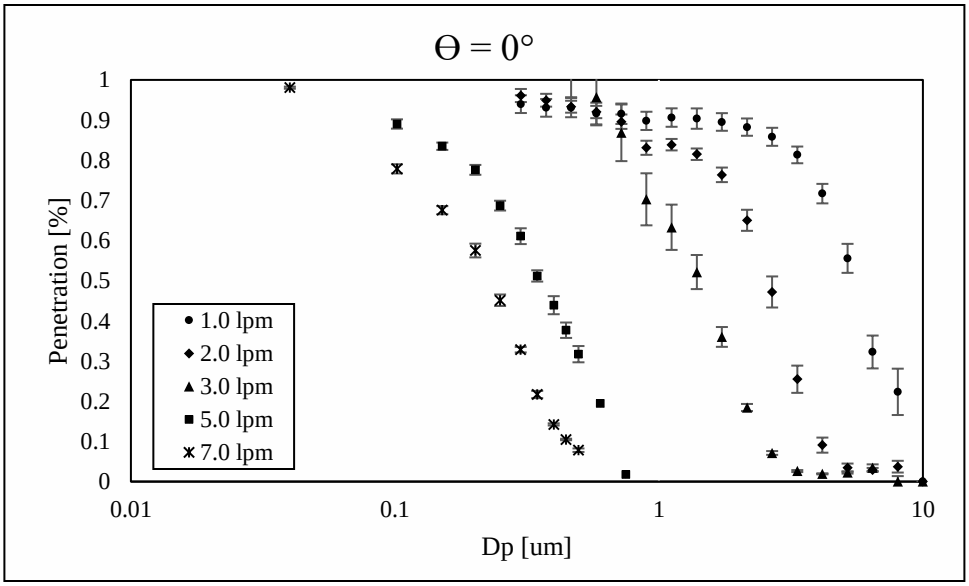
Θ = 0°
Penetration [%]
1
0.9
0.8
0.7
0.6
0.5
0.4
0.3
0.2
0.1
0
1.0 lpm
2.0 lpm
3.0 lpm
5.0 lpm
7.0 lpm
0.01
0.1
1
10
Dp [um]

(a)

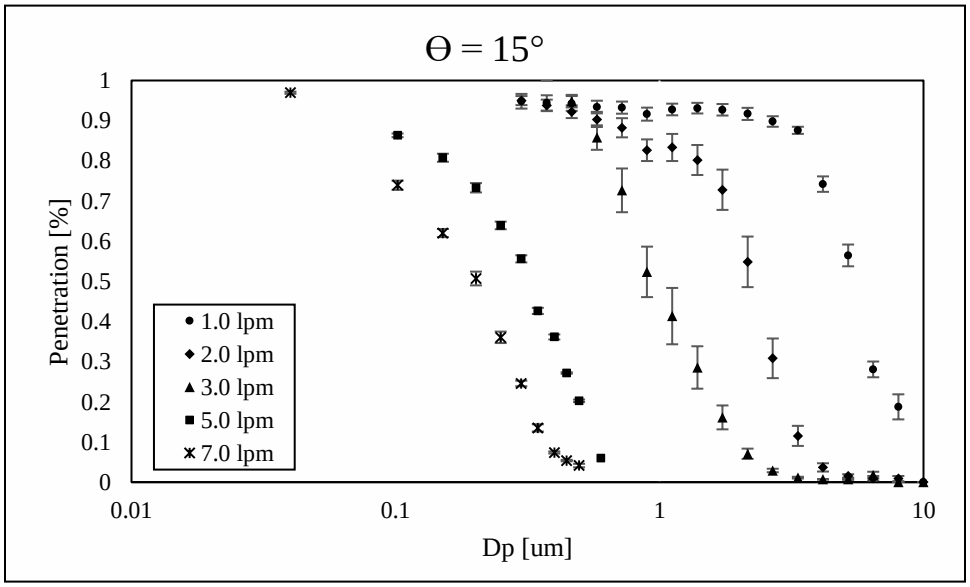
Θ = 15°
Penetration [%]
1
0.9
0.8
0.7
0.6
0.5
0.4
0.3
0.2
0.1
0
1.0 lpm
2.0 lpm
3.0 lpm
5.0 lpm
7.0 lpm
0.01
0.1
1
10
Dp [um]

(b)

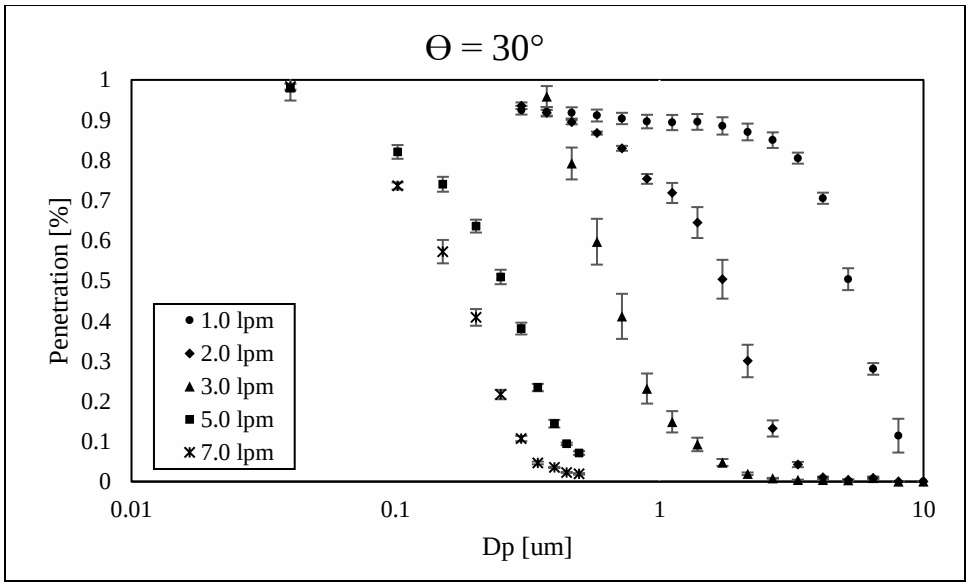

(c)

Figure 5 - 13 Particle penetration as a function of aerodynamic particle size for the prototype cyclones with different contract angle (i.e., 0°, 15° and 30°) under different sampling flowrates.

The steepness of measured particle penetration curves for all these three cyclones under various annual Reynolds number Re_{ann} were shown in Figure 5-14. Because of the conical contraction body of studied cyclones, we defined the annular flow Reynolds number of a cyclone as $Re_{ann} = \frac{\rho * V * (D_c - D_e)}{\mu}$, where ρ and μ are the density and viscosity of carrier gas, respectively. The characteristic velocity, V, is selected as the tangential velocity at the half height of studied cyclone body, which was estimated by assuming the conservation of angular momentum (i.e., $V = \frac{V_{in} * R_c}{R_{0.5h}}$, where R_c is the cyclone body radius, V_{in} is the inlet velocity and $R_{0.5h}$ is the radius at half height of a cyclone). The steepness of the penetration curves was defined as the square root of the ratio of particle size at the 70% penetration efficiency to that at the 30% efficiency. The data of curve steepness for mini- cyclone (Hsiao et al, 2009) and quadru-inlet cyclone (Liu et al, 2015) were also included in fig. 5-14. It was found that the steepness of particle penetration curves for three studied cyclones

was first increased as the cyclone Reynolds number increased, decreased as the number exceeding 2,000, and then reached constant as the number greater than 4,000. The above observation is possible because the effect of eddy motion in turbulent flow (in high Reynolds number regime) of a cyclone partially reduced the particle collection by the flow swirling. In general, the cyclones with the 15° and 30° body contraction angles offer slightly steeper cut-off curves as compared the cyclones with a cylindrical body.

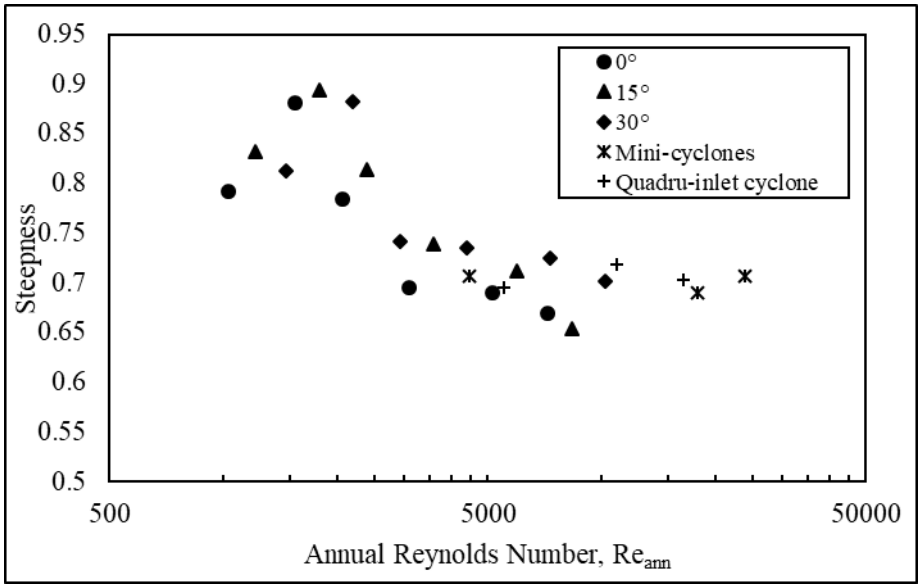

Figure 5 - 14 The steepness of cyclone penetration curves as a function of cyclone flowrate for studied cyclones, mini-cyclones and quadru-inlet cyclone.

(3) Vortex Finder Insertion length effect

Besides the body angle and sampling flowrate effect, the performances of the studied cyclones were also evaluated under different vortex finder insertion length (S). Figure 5-15 shows the particle penetration curves as a function of aerodynamic particle size for the three tapered body cyclones with different vortex finder insertion length (i.e., 0.2, 0.35 and 0.5 inches) at 2.0 lpm. There was no obvious change on the particle cut-off size for each cyclone under different insertion length. The particle penetration curves were merged with

each other for each case. Similar trend also found in the other two cyclones (i.e., 0° and 15°) under different sampling flowrates. These represented that changing vortex finder insertion length didn't affect the performance of the studied cyclones. This result was also consistent with the pressure drop data showing in figure 5-8.

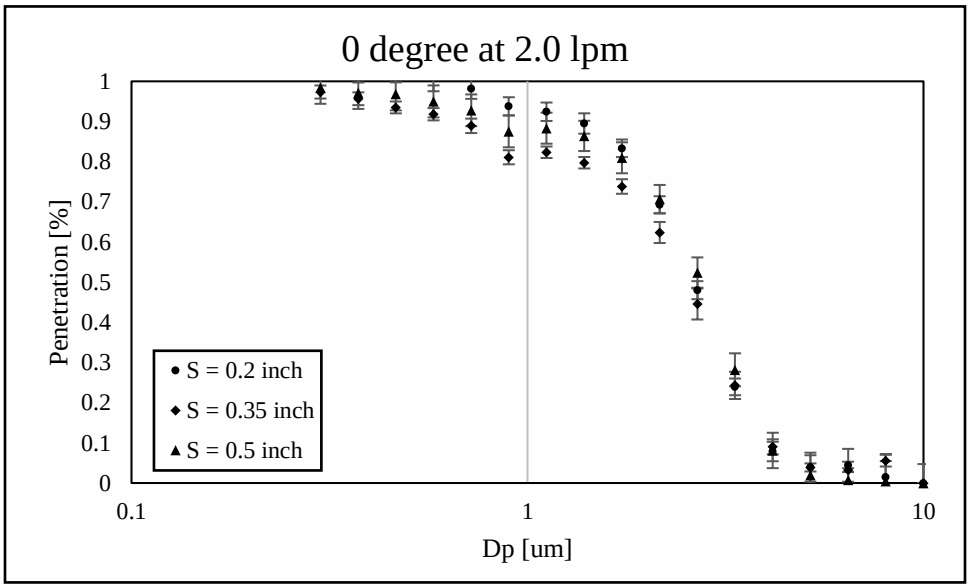

(a)

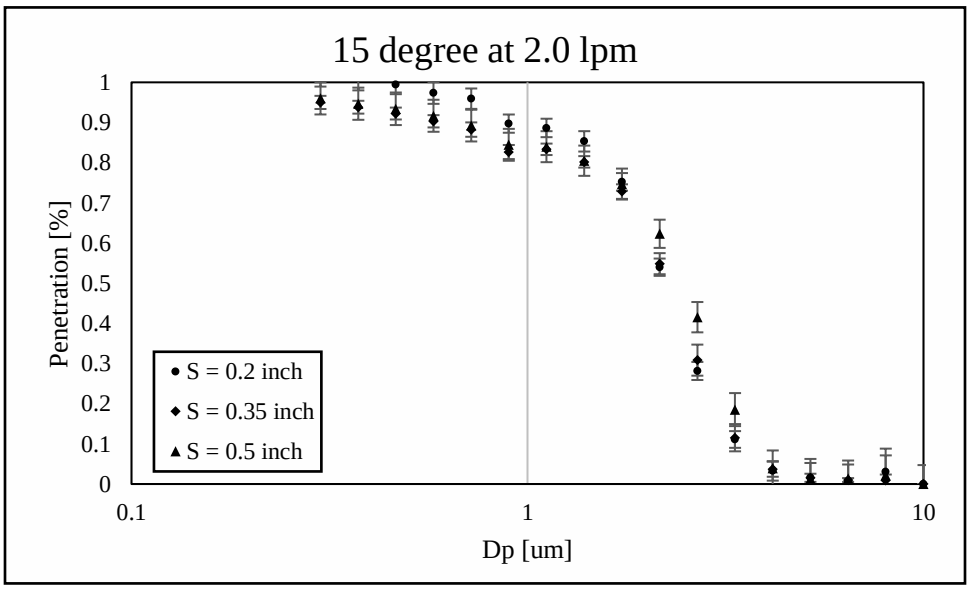

(b)

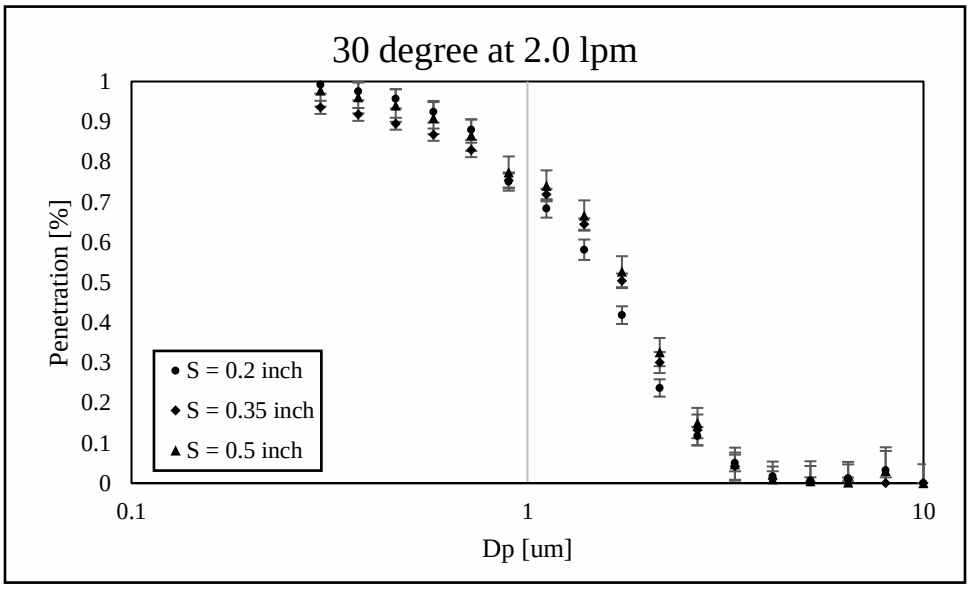

(c)

Figure 5 - 15 Particle penetration as a function of aerodynamic particle size for the prototype cyclones with different vortex finder insertion lengths. (a)cyclone with 0° body contract angle; (b) cyclone with 15° body contract angle; (c) cyclone with 30° body contract angle.

5.4.5 Relationship between the dimensionless particle cut-off size and the annular flow Reynolds number

Moore and McFarland (1990) had reported the linear relationship between the dimensionless particle cut-off size (i.e.,$\frac{C^{0.5}d_{50}}{D_c}$) and the annular flow Reynolds number (i.e., Re_{ann}):

$$\ln\left(\frac{C^{0.5}d_{50}}{D_c}\right) = a + b * \ln Re_{ann} \tag{5-5}$$

Where C is the Cunningham correction factor (dimensionless); d_{50} is the particle cutoff size. The annular flow Reynolds number is defined as

$$Re_{ann} = \frac{\rho * V * (D_c - D_e)}{\mu} \quad (5\text{-}6)$$

where ρ and μ are the density and viscosity of aerosol carry gas, respectively. For the quadru-inlet cyclone, the V is referred to the inlet velocity. For the tapered body cyclone, V is the average tangential velocity at the cyclone half height calculated from inlet velocity:

$$V = \frac{V_{in} * R_c}{R_{0.5h}} \quad (5\text{-}7)$$

where R_c is cyclone body radius, V_{in} is the inlet velocity and $R_{0.5h}$ is the cross-section radius at half height. Equation (5-6) is established under the conservation of angular momentum assumption.

The relationship of equation (5-5) was found for the performance of both the quadru-inlet cyclone and the tapered body cyclones.

(1) The quadru-inlet cyclone

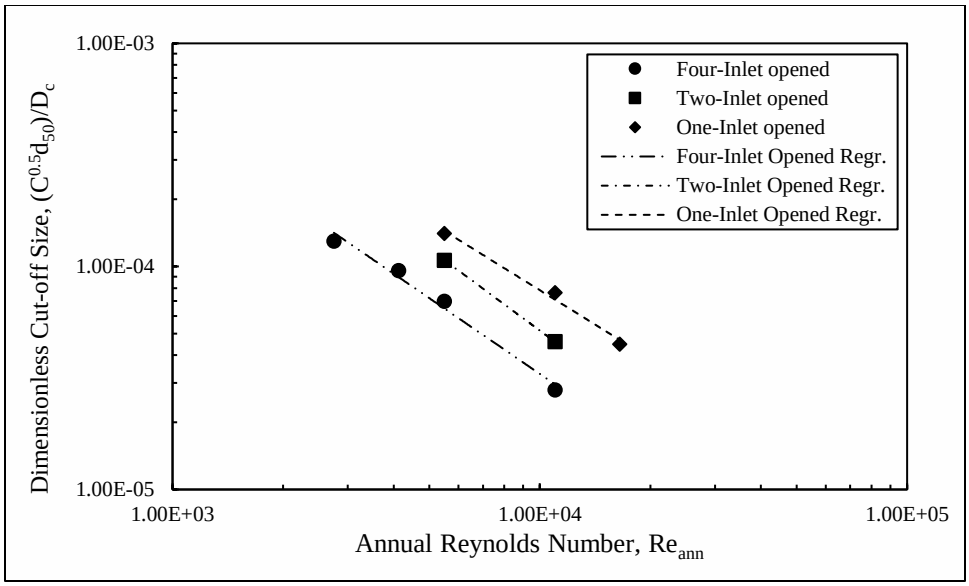

*Figure 5 - 16 Dimensionless cutoff size ($C^{0.5}$*$D_{p,50}/D_c$) vs. annular flow Reynolds number for the quadru-inlet cyclone with different opened inlet number.*

In figure 5-16, the relationship between the dimensionless cutoff particle size and the annular flow Reynolds number was observed in different testing cases of the quadru-inlet cyclone, which were under four inlets, two opposite inlets and a single inlet opened conditions. The slopes of the fitted lines were close to each other. The line interception with the y axis was increased as the number of the open inlets was reduced. The above observation shows that at the same annular flow Reynolds number the particle cutoff particle size of the cyclone can be reduced by having more inlets. By fitting the shown data sets using the equation with the format the same as Eq. (5-5), the following equation is obtained:

$$\ln\left(\frac{C^{0.5}d_{50}}{D_c}\right) = (0.7047 - 0.6122 * \ln n) - 1.1022 * \ln Re_{ann} \tag{5-8}$$

where n is the number of cyclone inlets. The above equation can be applied to the calculation of cutoff particle sizes of multi-inlet mini-cyclones during the design phase.

(2) The tapered body cyclone

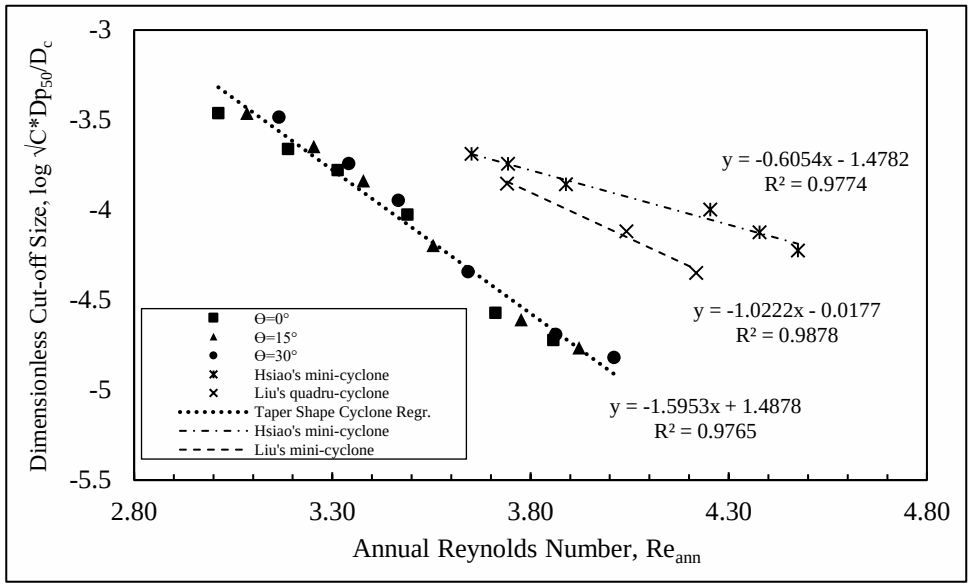

Figure 5 - 17 Dimensionless cutoff size vs. annular flow Reynolds number for the tapered body cyclones

Figure 5-17 shows the dimensionless particle cut-off size ($C^{0.5}d_{50}/D_c$) as a function of the annular flow Reynolds number (Re_{ann}) for the tapered body cyclones. As the annular flow Reynolds number increased, the dimensionless particle cut-off size decreased. This means that larger flow field can result in stronger collection efficiency. A linear regression equation was also obtained for the tapered body cyclones. The slope and the interception constant of the linear equation are −1.5953 and 1.4878, with $r^2 = 0.9765$. The regression model obtained here can be used to predict the operational flowrate for the studied cyclones for a desire particle cut-off size. The data of Hsiao's mini-cyclones and Liu's quadru-inlet cyclone were also included in figure 5-17. In comparison, the highest slope of linear regression was observed in the cases of cyclones with conical contraction body and the lowest slope of linear regression was occurred in the cases of mini- cyclones.

The above observation indicates that, at the same Re_{ann}, studied cyclones would have the smallest dimensionless cut-off sizes among all compared cyclones. Further analysis shows that the ratio of cyclone body height (H) to cyclone flow inlet diameter (i.e., D_{in}) has significant correlation with the slope of linear regression (i.e., the lower the ratio, the steeper the slope). The low D_{in}/H ratio implies low number of flow swirling turns in a cyclone, resulted in less frictional loss on the angular momentum of swirling flow. The other possible reason for the above observation might be due to the fact that it is easier to achieve the flow injection perfectly tangential to the cyclone body wall in studied cyclones than that in the other cyclones. It is because of much smaller flow opening designed in the mini- and quadru-inlet cyclones (when compared with that of studied cyclones).

5.4.6 Relationship between cyclone cutoff particle size ($D_{p,50}$) and pressure drop (ΔP)

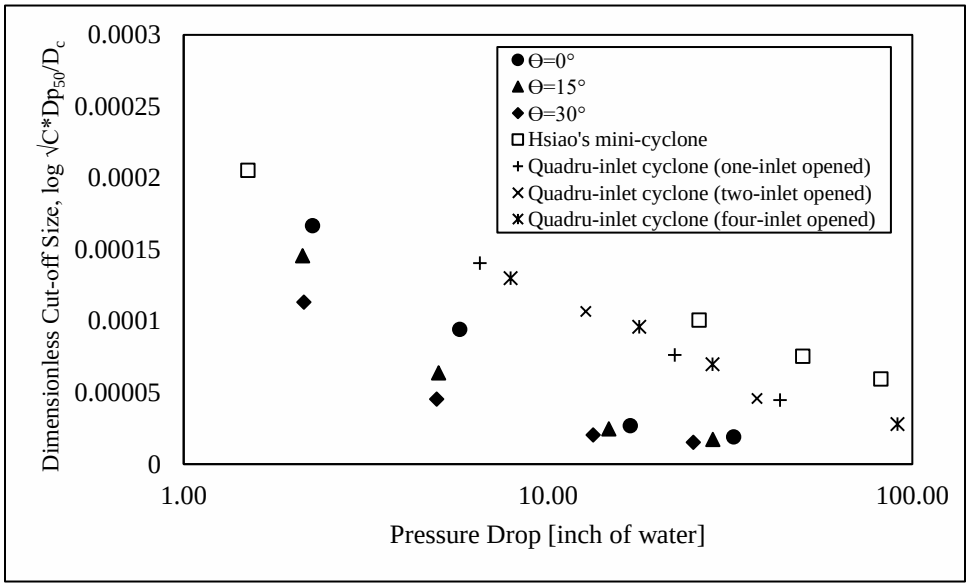

Figure 5 - 18 Dimensionless cutoff size vs. pressure drop for the prototype cyclones, Hsiao'mini-cyclone and Liu's quadru-inlet cyclone.

Figure 5-18 plots the relationship between the dimensionless particle cut-off sizes and the pressure drop of the studied cyclones with different body contract angle (i.e., 0°, 15°

and 30°), Hsiao's mini-cyclone and Liu's quadru-inlet cyclone. For all these cyclones, there shows a "one-to-one" relationship between the dimensionless particle cut-off sizes and the pressure drop. And, the dimensionless particle cut-off sizes were decreased as the pressure drop increased.

For the quadru-inlet cyclone, it is interesting to find out that all the three data sets (i.e., one-, two- and four-inlets open) are merged as one. This indicates that the particle cutoff size and pressure drop of the quadru-inlet cyclone were primarily attributed to the swirling flow in the cyclone body.

For the three tapered body cyclones, a rapid decrease in the particle cut-off size was observed as the cyclone pressure drop increased and less than 10 inH_2O (at which the operational flowrate was less than 3.0 lpm). The decrease in the cut-off size became gradual as the cyclone pressure drop further increased. To gain the maximal reward in the cut-off size reduction per unit pressure-drop increase, studied cyclones should be operated at the flow rate less than 3.0 lpm. It is because the power consumption required for cyclone operation is directly proportional to the cyclone pressure drop. More, at the same cyclone pressure drop, studied cyclones are capable of removing smaller particles than quadru-inlet cyclones and mini-cyclones.

As compared the data among the tapered body cyclones, it was found the cyclone with largest body contract angle (i.e., 30°) had the smallest particle cut-off size than the other cyclone (i.e., 0° and 15°) under the same pressure drop. This again shows the advantage for the conical body design.

5.5 Summary

A quadru-inlet mini-cyclone and a group of tapered body cyclones with different body contract angle (i.e., 0°, 15° and 30°) were designed and constructed. The body diameters of these cyclones are comparable to an US quarter coin. The pressure drop and particle penetration curve are two important characteristics for evaluating cyclones. Experiment were carried out to evaluate these two parameters for both the quadru-inlet cyclone and the tapered body cyclones.

According to the experimental data, the pressure drop values of both the quadru-inlet cyclone and the tapered body cyclones increased quadratically as the inlet velocity increased, which can be characterized by using the inlet dynamic pressure drop ($\rho_g V_i^2/2$) multiplied by a dimensionless loss coefficient, K_L. For the quadru-inlet cyclone, further experiments were performed to find out the loss coefficient (i.e., K_L) for the cyclone with only one- and two- inlets open. An empirical equation was also proposed to relate the loss coefficients to the number of open inlets. As for the tapered body cyclones, obvious difference can be found among the cyclones with different body contract angle: under the same sampling flowrate, the cyclone with larger body contract angle had larger pressure drop; the cyclone with smaller body contract angle had smaller pressure drop. However, changing the vortex finder insertion length showed negligible effects on pressure drop. A semi-empirical model modified from Dirgo's model was also developed for the tapered body cyclones.

The penetration curves of the quadru-inlet cyclone were studied under different sampling flowrate, which showed that the cutoff particle size decreased as the sampling flowrate increased. It is because of the increase of centrifugal force produced by the

cyclone vortex. In addition to test the penetration curve performance under different sampling flowrate, the tapered body cyclones were also tested under different body contract angle and vortex finder insertion length. Similar to what had found in the quadru-inlet cyclone experiment, increasing sampling flowrate resulted in decreasing the particle cut-off size for all the tapered body cyclones. Besides, at a fixed sampling flowrate, the tapered body cyclones with larger contract angle had the smaller particle cut-off size, while the cyclone with smaller angle had the larger particle cut-off size. However, the particle cut-off sizes of the tapered body cyclones were not affected by changing the vortex finder insertion length.

The linear relationship between the dimensionless particle cut-off size and the annular flow Reynolds number also was observed for the quadru-inlet cyclone and the tapered body cyclones. The slope value of the tapered body cyclones was larger than the quadru-inlet cyclone. The one-to-one relationship between the dimensionless particle cut-off sizes and the pressure drop of the quadru-inlet cyclone and the tapered body cyclones was also plotted. It was also found the cyclone with large body contraction angle removes smaller particles as compared to cyclones with low body contraction under the same cyclone pressure drop.

5.6 Reference

Avci, A. and I. Karagoz (2003). "Effects of flow and geometrical parameters on the collection efficiency in cyclone separators." Journal of Aerosol Science 34(7): 937-955.

Bräuner, Elvira Vaclavik, Lykke Forchhammer, Peter Møller, Jacob Simonsen, Marianne Glasius, Peter Wåhlin, Ole Raaschou-Nielsen and Steffen Loft. "Exposure to Ultrafine Particles from Ambient Air and Oxidative Stress-Induced DNA Damage." Environmental health perspectives, (2007): 1177-1182.

Chalupa, D. C., P. E. Morrow, G. Oberdorster, M. J. Utell and M. W. Frampton. "Ultrafine Particle Deposition in Subjects with Asthma." Environ Health Perspect 112, no. 8 (2004): 879-82.

Edwards, Rufus, Michael Johnson, Kevin H Dunn and Luke P Naeher. "Application of Real-Time Particle Sensors to Help Mitigate Exposures of Wildland Firefighters." Archives of environmental & occupational health 60, no. 1 (2005): 40-43.

Evans, J., et al. (2013). "Estimates of global mortality attributable to particulate air pollution using satellite imagery." Environmental Research **120**: 33-42.

Fan, J., et al. (2015). "The impact of PM2.5 on asthma emergency department visits: a systematic review and meta-analysis." Environmental Science and Pollution Research **23**(1): 843-850.

Geiser, Marianne, Barbara Rothen-Rutishauser, Nadine Kapp, Samuel Schürch, Wolfgang Kreyling, Holger Schulz, Manuela Semmler, Vinzenz Im Hof, Joachim Heyder and Peter Gehr. "Ultrafine Particles Cross Cellular Membranes by Nonphagocytic Mechanisms in Lungs and in Cultured Cells." Environmental Health Perspectives, (2005): 1555-1560.

Görner, P., et al. (2001). "Study of fifteen respirable aerosol samplers used in occupational hygiene." Annals of Occupational Hygiene **45**(1): 43-54.

Hsiao, Ta-Chih, Da-Ren Chen and Sang Young Son. "Development of Mini-Cyclones as the Size-Selective Inlet of Miniature Particle Detectors." Journal of Aerosol Science 40, no. 6 (2009): 481-491.

Kenny, L. C. and R. A. Gussman (2000). "A DIRECT APPROACH TO THE DESIGN OF CYCLONES FOR AEROSOL-MONITORING APPLICATIONS." Journal of Aerosol Science **31**(12): 1407-1420.

Kenny, LC, R Gussman and M Meyer. "Development of a Sharp-Cut Cyclone for Ambient Aerosol Monitoring Applications." Aerosol Science & Technology 32, no. 4 (2000): 338-358.

Lidén, Göran and Anders Gudmundsson. "Semi-Empirical Modelling to Generalise the Dependence of Cyclone Collection Efficiency on Operating Conditions and Cyclone Design." Journal of Aerosol Science 28, no. 5 (1997): 853-874.

Liu, D., et al. (2015). "Performance study of a miniature quadru-inlet cyclone." Journal of Aerosol Science **90**: 161-168.

Lim, K. S., S. B. Kwon and K. W. Lee. "Characteristics of the Collection Efficiency for a Double Inlet Cyclone with Clean Air." Journal of Aerosol Science 34, no. 8 (2003): 1085-1095.

Ma, Y., et al. (2011). "Fine particulate air pollution and daily mortality in Shenyang, China." Science of the Total Environment 409(13): 2473-2477.

Marra, Johan, Matthias Voetz and Heinz-Jürgen Kiesling. "Monitor for Detecting and Assessing Exposure to Airborne Nanoparticles." Journal of Nanoparticle Research 12, no. 1 (2010): 21-37.

Moore, M. E. and A. R. McFarland. "Design of Stairmand-Type Sampling Cyclones." Am Ind Hyg Assoc J 51, no. 3 (1990): 151-9.

Moore, M. E. and A. R. McFarland. "Design Methodology for Multiple Inlet Cyclones." Environmental Science & Technology 30, no. 1 (1996): 271-276.

Park, C.-W., et al. (2015). "Development of a single cyclone separator with three stages for size-selective sampling of particles." Journal of Aerosol Science 89(Supplement C): 18-25.

Potera, C. (2014). "Toxicity beyond the Lung: Connecting PM(2.5), Inflammation, and Diabetes." Environmental Health Perspectives **122**(1): A29-A29.

Pui, D. Y. H., et al. (2014). "PM2.5 in China: Measurements, sources, visibility and health effects, and mitigation." Particuology **13**: 1-26.

Samoli, E., et al. (2013). "Associations between fine and coarse particles and mortality in Mediterranean cities: results from the MED-PARTICLES project." Environmental Health Perspectives (Online) **121**(8): 932.

Shah, Alpa P, Anthony P Pietropaoli, Lauren M Frasier, Donna M Speers, David C Chalupa, Joseph M Delehanty, L Huang, Mark J Utell and Mark W Frampton. "Effect of Inhaled Carbon Ultrafine Particles on Reactive Hyperemia in Healthy Human Subjects." Environmental health perspectives 116, no. 3 (2008): 375.

Utell, Mark J and Mark W Frampton. "Acute Health Effects of Ambient Air Pollution: The Ultrafine Particle Hypothesis." Journal of aerosol medicine 13, no. 4 (2000): 355-359.

Weichenthal, S., M. Hatzopoulou and M. S. Goldberg. "Exposure to Traffic-Related Air Pollution During Physical Activity and Acute Changes in Blood Pressure, Autonomic and Micro-Vascular Function in Women: A Cross-over Study." Particle and Fibre Toxicology 11, (2014).

Xiang, R., et al. (2001). "Effects of cone dimension on cyclone performance." Journal of Aerosol Science **32**(4): 549-561.

CHAPTER 6 Dissertation Accomplishments and Recommendations for Future Work

6.1 Summary of accomplishments

In this dissertation, the performance of six commercial PM mass sensors was studied and a new electrical PM sensor for the geometrical surface area measurement has been successfully developed. In the first part of the dissertation, the selected PM sensors were challenged by particles with different physical properties and chemical compositions. The performance of the existing sensors was influenced by the test particles, which led to the second part of this dissertation — development of a new PM sensor. In the second part, an electrical PM sensor, consisting of a "core engine" and a size-selective inlet, was designed and studied. The performance of each component was carefully evaluated. The detailed accomplishments of each part are summarized as follows:

6.1.1 Evaluation of the existed PM mass sensor

Six PM sensors for mass concentration measurement, including five optical and one mechanical PM sensors, i.e., Sharp, Shinyei, Samyoung, Oneair, TSI DustTrak and Personal Dust Monitor (PDM) were selected in this study. The performance of these sensors was calibrated under the steady particle mass concentration condition and using lab-generated particles of various physical and chemical properties, i.e., total mass concentration, peak size, geometrical standard deviation of particle size distribution, and particle composition. The scientific TEOM (Model 1405) was selected as the reference in this calibration.

The linear relationship between the readouts of all test PM sensors and the particle mass concentration, obtained from the TEOM, was found for test particles under the fixed

size distribution and composition. However, the readouts of all tested optical PM sensors are sensitive to the physical and chemical properties of test particles. In addition, performance differences were observed for the low-cost optical PM sensors under the steady particle concentration condition and transient particle mass concentration condition (i.e., under calm air condition), which might be because of the presence of dead space in the particle passages of low-cost optical PM sensors.

In sum, proper calibration of the low-cost optical PM sensors using local particles is required to monitor the PM pollution. Besides, when measuring the large particles in the ambient, potential sampling issues should be considered for the usage of low-cost PM sensors.

6.1.2 Development of a new electrical PM monitor for integral parameter measurement

A new electrical PM sensor, consisting of a corona-based aerosol charger, a precipitator and high sensitive current meters, had been developed for integral parameter measurement (i.e., total surface area concentration and mass concentration). Different from the previous electrical aerosol detector, a new measurement strategy was proposed: instead of measuring the current from the "escaping" charged particles, the signal of the new PM sensor was collected from the current induced by the precipitated charged particles.

The performance of the core components (i.e., the charger and precipitator) were evaluated separately, and optimal operation parameters were thus defined. By assembling the components together, the new PM sensor performance was challenged by particles with different physical properties and chemical compositions. As a result, the new PM sensor was capable of measuring the particle total surface area concentration. However, variation

on the calibration curves of different test particles was observed when applying the new electrical PM sensor for mass concentration measurement.

6.1.3 Development of small cyclones as size-selective inlet

Two types of small cyclones (i.e. quadru-inlet cyclone and tapered body cyclones) were developed as size-selective inlets for the new PM monitor, of which body diameter are smaller than a US quarter. The pressure drop and particle penetration curve performance were evaluated for all prototype cyclones. In addition, a mathematic model was successfully developed for predicting the cyclone pressure drop. A linear relationship between the dimensionless particle cut-off size and the annular flow Reynolds number was observed in the log-log plot for all studied cyclones. The semi-empirical model can be applied as guidance in future cyclone design.

In the comparison among all the prototype cyclones, it was found that under the same pressure drop, the tapered cyclone with the largest body contract angle was capable for removing more particles and achieving the smallest particle cut-off size. This is favorable when applying the cyclone as the size-selective inlet for the PM monitor.

6.2 Recommendations for future research

In the new electrical PM sensor development, the calibration curves were influenced by particles with different physical properties and chemical composition when measuring the particle mass concentration. The reason for this was that the measured signal didn’t achieve the third power of particle size. More efforts are required for achieving the task:

(1) Improving charger performance via better charger design. The exponent on the power function of the mean charge per particle to the particle size was about 1.6 for the current charger. Since the value can be 2 according to the charge limit theory, there is still hope for improving the exponent. A charger with better design, which enables more ions to be attached on particles, can fulfill the above requirement.

(2) Adding additional precipitation stage. Increasing the number of ions on particles could result in low charging efficiency, because particles with more ions are more likely to be precipitated in the electrical field. By adding the 3rd stage precipitator, the exponent in the measured signal equation could be increased, while the charger can keep operating at a relatively low current.

In addition to the performance improvement, the new PM sensor shall be integrated in a compact size. The software development and performance calibration should be carried out for the integrated PM sensor. Except for the lab calibration, the performance of the electrical PM monitor shall be validated by field study for ambient aerosol measurement.

Up to now, the electrical PM sensor has been studied for particle integral parameters measurement (i.e., surface area and mass concentration). It can also be applied as a particle sizer for size distribution measurement. To achieve this additional feature, a data-reduction scheme should be developed to retrieve the size distribution of the particle from the PM sensor readout at different precipitator voltages.

VITA

Di Liu

EDUCATION

Ph.D. in Mechanical Engineering 01/2013 – 08/2018
Virginia Commonwealth University, Richmond, VA, USA

Master program in Energy, Environmental & Chemical Engineering 08/2012 – 12/2012
Washington University in St. Louis, MO, USA

B.S. in Environmental Science 09/2008 – 06/2012
Sut Yat-sen University, Guangzhou, Guangdong, China

PUBLICATION

Liu, D., et al. (2015). "Performance study of a miniature quadru-inlet cyclone." Journal of Aerosol Science 90(Supplement C): 161-168.

Liu, D., et al. (2017). "Performance calibration of low-cost and portable particular matter (PM) sensors." Journal of Aerosol Science112: 1-10.

Liu, D., et al. "Study of Small Cyclones with Conical Contraction Bodies." Accept by Aerosol and Air Quality Research.

Liu, D., Liu, Q. and Chen D.R. A New Miniature Electrical Ultrafine Particle Sizers. to be submitted Environmental Science and Technology.

Liu, D. and Chen. D.R. An electrical PM sensor for the aerosol integral parameter measurement. In preparation.

CONFERENCE PRESENTATIONS

Liu, D. and Chen, D.R. Performance Evaluation of Miniature Cyclones with Multiple Inlets. American Association for Aerosol Research 32st Annual Conference, Sept.30-Oct.12, 2013, Portland, OR, USA.

Liu et al. Performance Study of Miniature Cyclones with Multiple Inlets. American Association for Aerosol Research 33st Annual Conference, Oct.20-Oct.24, 2014, Orlando, FL, USA.

Liu D., Liu Q., and Chen, D.R. Performance Comparison of Aerosol Corona-based Mini-chargers for Miniature Ultrafine Particle Sizers. American Association for Aerosol Research 34st Annual Conference, Oct.12-16, 2015, Minneapolis, MN, USA.

Liu, D. and Chen, D.R. Performance Evaluation of portable sensors and existed personal monitors. American Association for Aerosol Research 35st Annual Conference, Oct.17-Oct.21, 2016, Portland, OR, USA.

Liu, D. and Chen, D.R. A New Electrical Particulate Matter Sensor (eM sensor). American Association for Aerosol Research 36st Annual Conference, Oct.16- Oct.20, 2017, Raleigh, NC, USA.